Free surface flows: Coalescence, Spreading and Dewetting

José Federico Hernández Sánchez

Free Surface Flows: Coalescence, Spreading and Dewetting

José Federico Hernández Sánchez

Graduation committee members:

Chair:	Prof. dr. ir. J.W.M. Hilgenkamp	Universiteit Twente
Promotor:	Prof. dr. J.H. Snoeijer	Universiteit Twente & Technische Universiteit Eindhoven
Members:	Dr. H. Okorn-Schmidt	Lam Research, Austria
	Prof. dr. D. Lohse	Universiteit Twente
	Prof. dr. ir. C.H. Venner	Universiteit Twente
	Prof. dr. A. Darhuber	Technische Universiteit Eindhoven
	Prof. dr. H. Riegler	Max Plank Institute of Colloids and Interfaces, Germany

The work in this thesis was carried out at the Physics of Fluids group of the Faculty of Science and Technology of the University of Twente. It was funded by Lam Research Corporation.

Title:
Free Surface Flows: Coalescence, Spreading and Dewetting

Publisher:
José Federico Hernández Sánchez, Physics of Fluids, University of Twente,
P.O. Box 217, 7500 AE Enschede, The Netherlands
pof.tnw.utwente.nl

ISBN: 978-90-365-3823-7

FREE SURFACE FLOWS: COALESCENCE, SPREADING AND DEWETTING

DISSERTATION

to obtain the degree
of doctor at the University of Twente,
on the authority of the rector magnificus,
Prof. dr. H. Brinksma,
on account of the decision of the graduation committee
to be publicly defended
on Friday the 20th of February of 2015 at 14:45 hours

by

José Federico Hernández Sánchez
Born on the 27th of April 1982
in Mexico City

This dissertation has been approved by the promotor:

Prof. dr. ir. Jacco Snoeijer

dedicated to all pioneers

Contents

1 Introduction

1.1 Motivation

1.1.1 Capillary phenomena

Capillary and wetting phenomena are an essential part of nature. Its presence is noticed in many circumstances where solid and liquid surfaces come into contact. We notice it when we cycle in the rain and our skin gets wet, a direct consequence of the chemical interaction between the surfaces of our skin and water. It also shows up in the kitchen, when the water jet that appears when we open the faucet naturally breaks into a train of drops due to the surface tension [1]. The influence of capillary forces becomes more evident when looking at the small scales in which some organisms live. For example small insects evolved to cope with the strong influence of capillarity and even use it on its advantage [2]. It can be seen that the ant and the spider in Fig. 1.1 interact with water very differently than humans.

When the ant in Fig. 1.1a) is in contact with water, the water surface becomes strongly deformed, indicating the strong effect of surface tension at this scale. For the ant, water represents at the same time a challenge and a huge threat. On one hand the ant requires a strategy to surpass the surface tension barrier and drink. On the other hand, if the barrier is deeply penetrated, recoiling will be not possible and the ant will drown. Other animals like the diving bell spider (*Argyroneta aquatica*) use

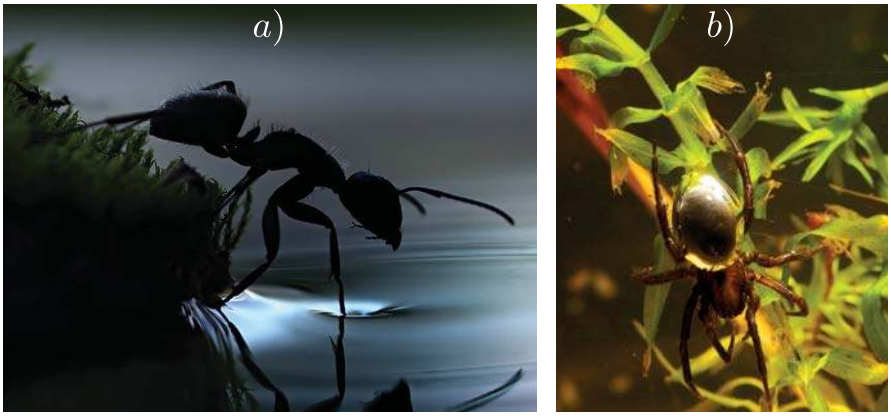

Figure 1.1: Examples of capillary forces at length scales. *a*) Ant using its leg to strongly deform the water surface. Photograph taken from Vadim Trunov website (`https://500px.com/vadimtrunov`). *b*) Diving bell spider showing an air entrapment around its abdomen when is submerged in water. Photograph taken from `http://www.newswise.com/`.

the surface tension to its advantage. As shown in Fig. 1.1*b*), when the spider dives underwater, its abdomen gets enclosed by an air film. This entrapment occurs due to hydrophobicity of the surface of its abdomen, a property that repels water. This is used by the spider to construct a nest within a bubble, allowing it to breath underwater. The diving bell spider spends most of its life inside this bubble, only leaving occasionally to renew the air.

However, since the influence of capillary forces occurs on a range of action of rather small lengths, it remained out of human sight for a long time. Leonardo da Vinci (1452-1519) introduced capillary phenomena for the first time in his notes, describing the menisci of liquid on a capillary tube [1]. Since then, the field of interfacial phenomena has gained a major relevance as a branch of physics, being essential in some problems of fluid mechanics. For example, capillary forces dictate the boundary condition at the free surface in the classical problem of Rayleigh-Plateau instability. A cylindrical filament of liquid with finite surface tension will break into drops under the influence of a perturbation. This instability is sometimes observed on spiderwebs early in the morning, as shown in Fig. 1.2*a*). Another example was presented by Podgorski *et al.* [3], where the contact line dynamics determines the shape of drops sliding on the glass window during rain. In Fig. 1.2*b*), we see drops sliding down an inclined plain. On the left side the inclination angle is small, show-

ing a moderately elongated drop, while on the other side, due a high inclination, the opposite is seen [4].

The research on capillary phenomena has extended beyond the scope of the fluid mechanics, supporting advances in other fields, such as micro-biology, where it was found that on non-wetting surfaces, the growth of bacteria is decreased. This knowledge is very relevant in the design of medical tools and equipment [5]. Similarly, capillarity and wetting are very important for many industrial applications. An example using the Rayleigh-Plateau instability is found in the technology of inject printing, where many droplets are controllably produced at very high frequency. Also, during a rain storm, a liquid-film forms on the wings of aircrafts. At high altitudes, this liquid film freezes, increasing the weight and the risk of accident of the aircraft. Giving hydrophobic properties to the wings surface, avoids the formation of the liquid film [6]. One last example of capillary effects applicability is the enhanced protection to corrosion given by the hydrophobic surfaces [7]. This is of great importance in the industry of maritime ships, in which surfaces are always exposed to seawater. It has also been claimed that hydrophobicity reduces the drag of these ships [8, 9].

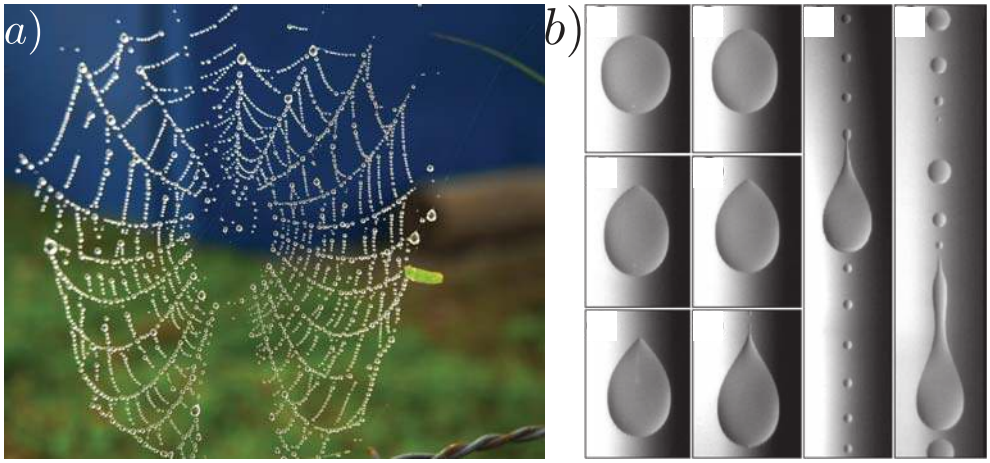

Figure 1.2: *a*) Rayleigh-Plateau instability on a spider web. Taken from `http://upload.wikimedia.org/wikipedia/commons/`. *b*) Water drops sliding on a partially wetting substrate on an inclined plane. Figure taken from Podgorski *et al.* [3].

1.1.2 Dewetting and drying: A technological instrument raising fundamental questions

One of the industries that crucially relies on controlling the dynamics of wetting, is the semiconductor technology. Here different methods are used to modify the wetting properties and clean the silicon wafers used for manufacturing chips. Tools are designed to perform the cleaning methods in mass production, which requires perfect control of most aspects of the processes. The above takes place within a clean environment, protecting the wafers from contamination. Fig. 1.3*a*) shows one of the tools used for this purpose by the Lam Research Corporation, who funded this thesis work. These machines are designed to process the wafers as fast as possible under highly controlled conditions. It can be observed that boxes of silicon wafers are inserted in one side of the tool.

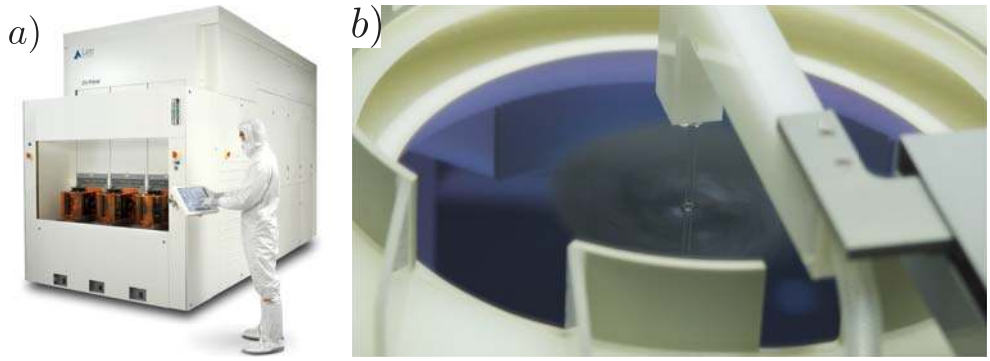

Figure 1.3: *a*) Wet-processing system from the Lam Research Corporation. This is one of the tools used to clean and dry silicon wafers used in the semiconductor industry. *b*) The process chamber used to clean and dry silicon wafers. A mechanical arm rinses the silicon wafer while spinning. The tubes supply different liquids, such as, ultra-pure water, organic solvents and cleaning solutions. This process is followed by spin drying; as the wafer rotates, a flux of gas presses the liquid film, increasing evaporation and forcing the drying. Images courtesy of Lam Research Corporation.

Fig. 1.3*b*) shows a snapshot of a cleaning process occurring inside the tool in Fig. 1.3*a*). The image shows a silicon wafer while a mechanical arm is rinsing a continuous jet of liquid on the surface. The arm carries a nozzle that can rinse the wafer with different liquids or blow gas to dry it. Several liquids can be used during the rinsing, such as ultra pure water, organic solvents and cleaning solutions. A description of the cleaning solutions and their use can be found on Kern [10] and more extensively in Reinhardt & Kern *et al.* [11]. During this process the wafer is rotating

at high spinning rates, maintaining the thickness of the liquid film rather small. The above introduces strong influence of capillary forces when the surfaces are rinsed and dried. Moreover the dynamics of the contact line motion is modified by the evaporation of liquids like water or isopropanol.

The process of drying is also influenced by other factors. If residual chemical compounds remain on the surface of the wafer, defects will appear. To avoid this, in one of the last steps of cleaning the chemical compounds are rinsed away from the wafer with ultra pure water. However, water evaporates rather slowly when compared with organic solvents. To increase the drying speed, ultra pure water is rinsed with isopropanol, which evaporates faster. By mixing these liquids, gradients of surface tension appear on the film since the surface tension of water is higher than the alcohol's. Thomson [12] already reported an intricate motion of the surface when mixing liquids such as alcoholic spirits and water. In fact, mixing liquids with different surface tensions, leads to surface tension gradients that are responsible for this behavior. This gradient of surface tension is typically referred as Marangoni forces and can lead to highly complex flow behaviors.

In fact, surface tension gradients are introduced in the process with a technique called Marangoni drying [13]. This technique is used widely to improve the drying velocity by adding vapor of a lower surface tension substance to the gas jet. When controlled, these interactions increase the velocity of dewetting, and also improve the degree of cleanliness of the surface [13]. However soluto-Marangoni forces, *i.e.* capillary forces due to gradients in chemical composition, are an usual source of instabilities, *e.g.* tears [14], that might be undesirable in processes in which homogeneous properties are aimed. It is known that during this part of the process defects appear on the substrate [15], reducing the amount of functional chips and the quality of manufacture.

Several questions arise when looking in detail to these various cleaning and drying processes. What happens when the liquid film is replaced by another liquid of lower surface tension? Or even more generally, what occurs when two liquids with different surface tensions are brought into contact? What is the influence of Marangoni stresses? Is the dynamics of drying affected by an external forcing, such as the spinning rates or the gas flux? Are the Marangoni forces responsible for instabilities causing defects on the surface? As such, this application poses interesting questions both from the fundamental and the technological point of view. In this thesis, we will address these questions by studying at simpler experimental realizations

that involve the same physical mechanisms.

1.2 Main topics

In the following part we will describe the specific background related to each of the specific topics we engage: Coalescence, Marangoni spreading and dewetting.

1.2.1 Coalescence of drops

One recent example of a conceptually simple experiment involving surface soluto-Marangoni forces is given by Karpitschka & Riegler [16]. In their experiments, two miscible sessile drops of different compositions are placed next to each other as shown in the side view sketch in Fig. 1.4*a*). In this figure we denote the surface tension of the two liquids by γ_1 and γ_2.

When drops of identical composition are put into contact, $\gamma_1 = \gamma_2$, the drops coa-

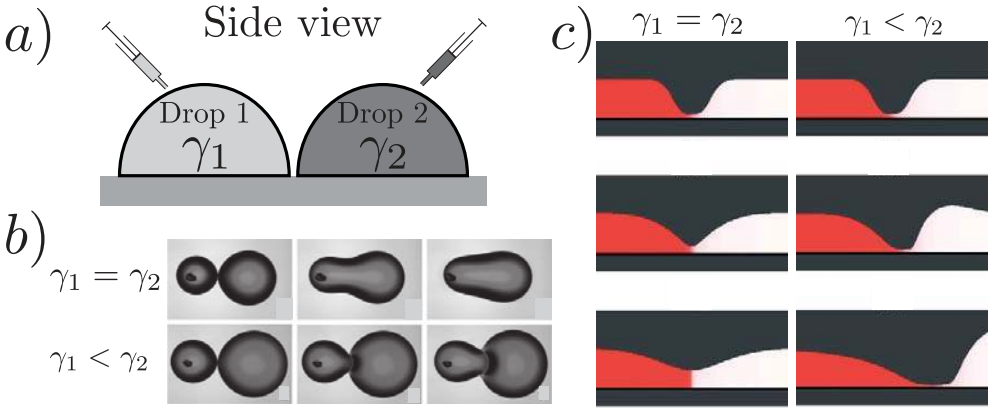

Figure 1.4: *a*) Sketch of drops on a substrate prior to coalescence. The drops are composed of different liquids with different surface tensions. *b*) Coalescence of sessile drops visualized from the top. Liquids from the same materials coalesce into one drop via a liquid bridge, as observed in the top panel. Instead, drops with different surface tensions form a bridge that displaces horizontally, as seen in the lowest part of the panel. Taken from Karpitschka & Riegler [16]. *c*) Comparison between numerical simulations of coalescence (left) and delayed coalescence (right) using the 1D lubrication approximation. Taken from Borcia *et al.* [17].

lesce through a bridge that continuously grows, ultimately forming a single drop as

shown in the upper photos of Fig. 1.4*b*). If the drops are of different compositions, a gradient of surface tension appears at contact, leading to the observation in the lower panel of Fig. 1.4*b*). Here, the bridge between the two drops does not grow, but instead moves at a constant velocity in the direction of the drop with larger surface tension. A numerical model of this phenomena, using the one-dimensional lubrication approximation coupled with Marangoni forces is presented in Borcia *et al.* [17]. The different interactions of the drops are replicated in the numeric simulations resulting in the height profiles presented in Fig. 1.4*c*). On the left side of the image, we observe the time evolution of the profiles in the absence of surface tension gradients. On the right side, the red color represents a liquid with lower surface tension than the white one. Once more, under the action of Marangoni forces we observe that the bridge does not grow, but in contrast it moves horizontally towards the drop of the higher surface tension [16, 18, 19].

Interestingly, even in the absence of Marangoni stresses, the problem of coalescence is challenging and still debated [20–22]. In Fig. 1.5 we present two different geometries of coalescence: freely suspended (top) and sessile drops (below). Fig. 1.5*a*) shows a sketch of the the experimental setup of the freely suspended drops. Fig. 1.5*b*) presents two snapshots of this experiments, the first one (on the left) is just before the coalescence starts and the second one (on the right) shows the bridge between the drops after 1μs. The coalescence of water drops is dominated by inertial forces and occurs very fast, taking only a few micro-seconds. The key question is to understand the rapid dynamics after the drops are put into contact. In this case the radius of the neck scales as $r \sim t^{1/2}$ as predicted by Duchemin *et al.* [23] and experimentally confirmed by Aarts *et al.* [24]. Here, the scaling law emerges from a balance between capillary forces and the inertia of the liquid. However the coalescence is strongly delayed for liquids whose viscosity is much higher than the one of water (high viscosity) [24], showing much larger time scales and leading to a radius of the neck scaling as $r \sim t \log t$, as predicted by Hopper [25] and Eggers *et al.* [26]. In more recent work, Paulsen *et al.* [27] advocates the existence of an inertio-viscous regime.

The coalescence of drops on a substrate, however, exhibits a much more complicated geometry. The top view is different from the side view, due the presence of the wall, where a contact angle appears as shown in the sketch in Fig. 1.5*c*). For highly viscous drops in Fig. 1.5*d*), the radius of the neck was experimentally found to scale as $r \sim t^{1/2}$ as presented by Ristenpart *et al.* [20]. Interestingly, the $1/2$ exponent for the freely suspended drops was achieved for inertial coalescence (low viscosity),

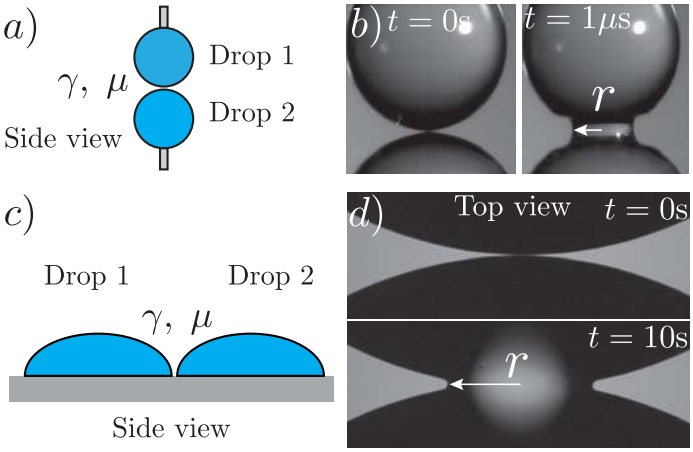

Figure 1.5: Two geometries for drop coalescence. *a*) Sketch of coalescence experiments of freely suspended drops. *b*) Snapshots of experiments of coalescence of two freely suspended drops of water. On the left, a snapshot before coalescence starts. On the right, a snapshot $\sim 1\mu$s after the coalescence starts. Taken from Aarts *et al.* [24]. *c*) Sketch of the side view of the coalescence of sessile drops. *d*) Snapshots of experiments of coalescence of sessile drops visualized from the top. Taken from Ristenpart *et al.* [20].

while for the sessile drops appears in the viscous limit. At present, there is limited experimental evidence for the bridge dynamics from the side, and scaling arguments different from [20] have been proposed [21, 22].

1.2.2 Marangoni spreading

During spin drying, a technique that uses centrifugal forces to remove water from the surface of silicon wafers, several phenomena take place. As was mentioned before, in the last step of cleaning, water is used to remove chemicals from the wafers, that remain at the surface. Later, a jet of isopropanol is discharged at the center of the wafer. Isopropanol is miscible with water and evaporates much faster, so the liquids are effectively exchanged. During this exchange of liquid, Marangoni forces appear due the difference in surface tension. Such forces are often associated to instabilities that could lead to defects on the surface of the wafer. Its dynamics presents also an interesting fundamental problem in the same spirit of the delayed coalescence [16], but now appearing in a different geometry of a thin liquid film.

The first study of interaction of liquids with different surface tensions was presented already by Thomson in 1855 [12]. He performed experiments pouring liquor on a glass of water and observed the effect of the interaction of the two different liquids. Below he describes the experimental technique as follows:

> *One part of these phænomena is, that if, in the middle of the surface of a glass of water, a small quantity of alcohol or strong spirituous liquor be gently introduced, a rapid rushing of the surface is found to occur outwards from the place where the spirit is introduced.*

Indirectly, he describes the direction of the Marangoni stress by stating that the high-surface-tension water pulls the liquid outwards. Thomson also specifies that Marangoni stresses occur in both thick and thin films. Even more, he describes the effect occurring when liquor is poured on a thin film of water:

> *If water be poured to the depth of about a tenth of an inch or less on a flat silver tray or marble slab, previously cleaned from any film which could hinder the water from thoroughly wetting its surface; and if then a little alcohol or wine be laid on the middle of that water, immediately the water will rush away from the middle, leaving a deep hollow there, and indeed leaving the tray bare of all liquid except an exceedingly thin film of the spirit, which continues always thinnest close to the margin of the water, because the water draws out to itself every portion of the spirit which approaches close to its margin.*

In the text, Thomson describes that after pouring the alcohol on the thin water film, the interaction of both liquids creates a stable patch of an even thinner region. To our knowledge, there is no extensive, systematic study on the thinning of the film after the exchange of liquids. By contrast a similar type of Marangoni spreading has been studied extensively using surfactants. Experimentally, surfactants are deposited on top of a thin film, changing locally the surface tension [28–38], similar to the effect of adding alcohol. However, a variety of results have been reported in several studies of surfactant spreading, depending on wether surfactants are soluble or not, or on the thickness of the layer. Jensen & Grotberg [30] and Jensen [31] predicted that the radius of spreading would scale as $r \sim t^{1/4}$ for thin films. This was corroborated experimentally by Gaver & Grotberg [29] and more recently by Fallest *et al.* [36]. Additionally, predictions for the radius of spreading of surfactants have been leading to different scaling laws [36].

Returning to the interaction of liquids with different surface tensions, Fournier & Cazabat [14] gave a quantitative description of the “tears of wine” effect. This

is a typical example of a Marangoni instability driven by evaporation at the contact line. The phenomena can be observed some time after a glass of any strong spirit is poured in a cup, *e.g.* a glass of wine, drops start climbing the inner part of the container. Colloquially, it is believed that the amount of drops ascending, also called tears, is related to the quality of the liquor. However, it was demonstrated that the effect is only related to the alcohol content of the mixture [14]. The alcohol contained in the spirit evaporates faster than the water, which is more noticeable at the contact line. Here water concentrates resulting in a local high surface tension at the border between the liquid and the container. This local surface tension gradient pulls up the liquid along the wall. Finally, a minimization of free surface takes place, by concentrating the film into a series of tears.

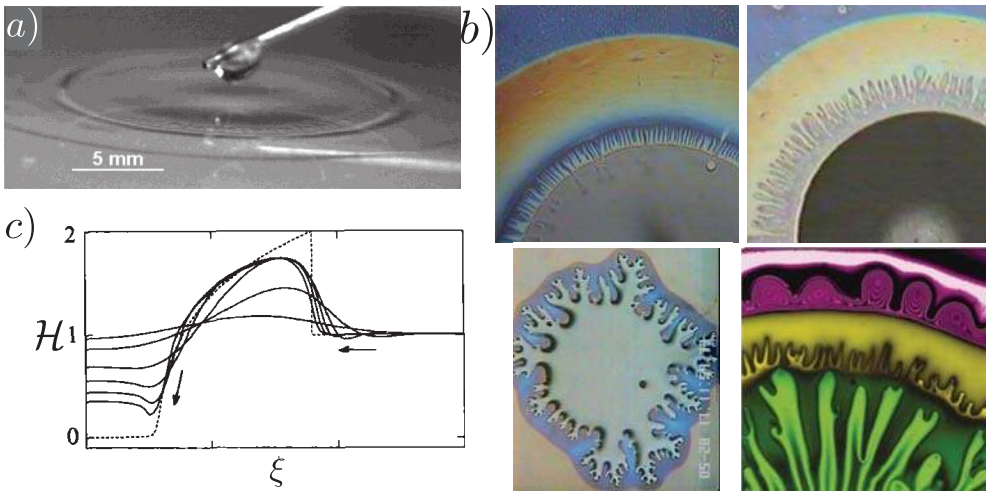

Figure 1.6: *a*) Snapshot from an experiment of surfactant spreading on a layer of liquid, via a drop deposition. Taken from Afsar-Siddiqui *et al.* [39]. *b*) Experimental visualization of surfactant spreading observed from the bottom view. Marangoni forces are responsible for the different fingering patterns observed. The upper images as well as the left-lower are taken from Hamraoui *et al.* [34]. The right-lower image was taken from Darhuber & Troian [40]. *c*) Numerical simulations of the evolution of the height profile of a non-soluble surfactant in an axisymmetric geometry, taken from Jensen & Grotberg [30].

Due its simplicity, a drop of surfactant spreading on a thin film has also been used as a setup to study Marangoni instabilities. Fig. 1.6*a*) presents a snapshot of an experiment performed by Afsar-Siddiqui *et al.* [39]. The pending drop contains

a surfactant that locally reduces the surface tension. After the deposition, a front develops a self similar height profile following the description of Jensen & Grotberg [30] with a characteristic cross section in Fig. 1.6*c*). Different studies have focused on the formation of fingering, leading to the beautiful patterns exemplified here. The three images of Fig. 1.6*b*) are examples of the wide variety of fingering morphologies presented by Hamraoui *et al.* [34]. In the bottom right image of Fig. 1.6*b*) it is presented a beautiful example of a fingering instability due a surfactant on glycerol [40], exhibiting a similar morphology to the tears of wine effect. For detailed reviews we refer to Matar & Craster [41] and Craster & Matar [42].

1.2.3 Dewetting under external forcing

An even more basic process is the dewetting of a liquid film, leaving behind a completely dry substrate (apart from the possibility of a nanoscopic precursor film [1, 43]). During the process of drying of silicon wafers, the interaction with the contact line is combined with other external forces. In particular, during spin drying a flux of gas normal to the substrate and located at the center of the wafer is used to remove the liquid from the surface. On partially wetting surfaces, the flux of gas induces a dry patch, delimited by a contact line. The liquid from the dry region forms a rim with the collected water that leaves behind a dry surface. The velocity of dewetting is enhanced by the external forcing from the gas flux, the spinning and by the Marangoni forces due differences in the chemical compositions. The detailed mechanisms of this enhancement have not been quantified. In particular, one would like to know the separate roles by the forcing due to the gas flux, the spinning and the Marangoni drying.

Even without external forces, important issues on the dewetting of a film remain a challenge. A first question is how the dewetting is initiated by the nucleation of a hole. This is for example addressed by Berendsen *et al.* [43], using the experiments shown in Fig. 1.7*a*). Once nucleated, the hole will grow at a constant velocity, leading to an spontaneous dewetting of a partially wetting substrate [1]. The liquid from the dry region is collected on a rim (ridge on Fig. 1.7*c*)) that has a dynamic contact angle θ_D. Experiments on "dewetting holes" are presented in Fig. 1.7*b*) by Redon *et al.* [44] and are described extensively in de Gennes *et al.* [1].

A second unresolved question is on the dynamic contact angle, for which two different predictions have been given. De Gennes *et al.* [1] proposed that the ratio between the dynamic contact angle and the equilibrium contact angle (θ_E) has a constant value $\theta_D/\theta_E \approx 0.25$. This is to be contrasted with the work by Snoeijer &

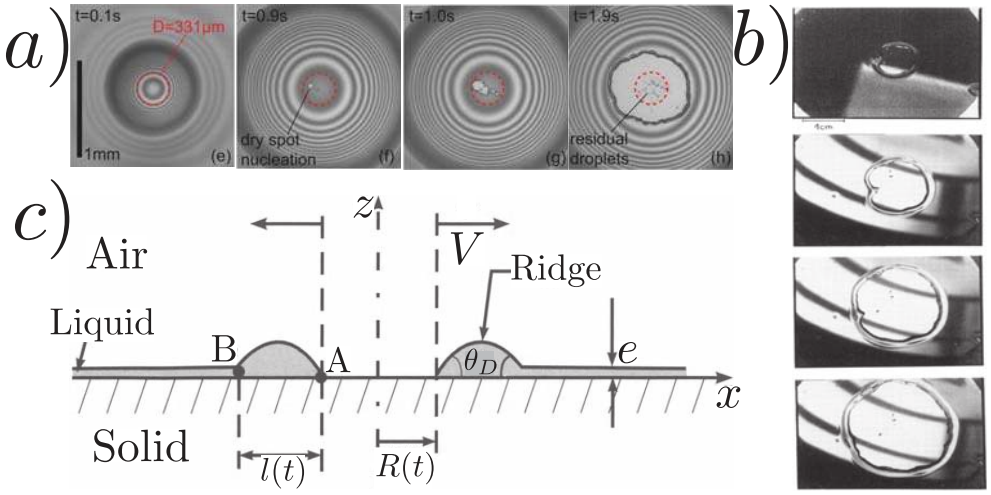

Figure 1.7: *a*) From left to right, time evolution of a continuously thinning film on a partially wetting surface. The thinning is induced by a strongly impinging air jet. The film breaks, nucleating a dry spot. The thickness of the film is measured using the interferometric fringes. Taken from Berendsen *et al.* [43]. *b*) Experiments of the dewetting hole by Redon *et al.* [44]. *c*) Sketch of the dewetting hole in an axisymmetric geometry. Taken from de Gennes *et al.* [1].

Eggers [45] who proposed a theory based on lubrication. This predicts a dynamic contact angle as a function of the capillary number, and with dynamic contact angles substantially larger than $0.25\theta_E$. However, a satisfactory experimental measurement of the dynamic angle of the dewetting rim is still lacking.

1.3 Guide through the thesis

In this thesis we investigate various problems that were described above. Chapter 2 presents experiments on the coalescence of viscous drops on a substrate. Observing the coalescence process from the side, we measure the size of the bridge connecting the drops as a function of time as well as the temporal evolution of the profiles. These measurements are performed for drops with different contact angles, so that the coalescence of symmetric and asymmetric drops is investigated. Using asymptotics of the lubrication approximation, a theory with no fitting parameters is developed and compared to the experiments.

In Chapter 3 a different experimental setup is used to investigate the effect of Marangoni forces of a thin film. A continuous train of drops of a liquid with a smaller surface tension is discharged on the water film, similar in spirit to the experiments performed by Thomson [12]. On the film a front is observed, moving the liquid previously deposited away from the jet. We vary the liquid's surface tension by changing the concentration of isopropanol to an aqueous mixture. Using a micro drop we also vary the flux on the liquid film. The thickness of the film is also controlled using spin coating at different spinning rates and rotation times. Based on these results, we propose scaling arguments to describe our experimental observations.

In Chapter 4 we focus on the dynamics of the dewetting rim. We use silicon wafer substrates, varying the hydrophobicity by vapor deposition of silanes. For each pair of liquid and substrate we determined the dewetting velocity. To resolve the issue of the dynamic contact angle of the dewetting rim, we develop an interferometry technique that allows measuring the liquid profile. In this Chapter we also investigate the influence that centrifugal forces have on the dewetting velocity, quantifying the increase of drying speed with the spinning rate. We also address the influence of different external forcing and report various instabilities.

References

[1] P.G. de Gennes, F. Brochard-Wyart & D. Quéré. Capillarity and wetting phenomena: drops, bubbles, pearls, waves. *Springer*, 2004.

[2] J.W. Bush & D.L. Hu. Walking on water: biolocomotion at the interface. *Annu. Rev. Fluid Mech.*, **38**, 339-369, 2006.

[3] T. Podgorski, J.M. Flesselles & L. Limat. Corners, cusps, and pearls in running drops. *Phys. Rev. Lett.*, **87**(3), 036102, 2001.

[4] N. Le Grand, A. Daerr, & L. Limat. Shape and motion of drops sliding down an inclined plane. *J. Fluid Mech.*, **541**, 293:315, 2005.

[5] R.M. Donlan. Biofilms: microbial life on surfaces. *Emerg. Infect. Dis.*, **8** (9), 881:90, 2002.

[6] L. Mishchenko, B. Hatton, V. Bahadur, J.A. Taylor, T. Krupenkin, & J. Aizenberg. Design of ice-free nanostructured surfaces based on repulsion of impacting water droplets. *ACS nano*, **4** (12), 7699:7707, 2010.

[7] T. Liu, Y. Yin, S. Chen, X. Chang & S. Cheng. Super-hydrophobic surfaces improve corrosion resistance of copper in seawater. *Electrochim. Acta*, **52** (11), 3709:3713, 2007.

[8] R.J. Daniello, N.E. Waterhouse, & J.P. Rothstein. Drag reduction in turbulent flows over superhydrophobic surfaces. *Phys. Fluids*, **21** (8), 085103, 2009.

[9] J.P. Rothstein. Slip on superhydrophobic surfaces. *Annu. Rev. Fluid Mech.*, **42**, 89:109, 2010.

[10] W. Kern. The evolution of silicon wafer cleaning technology. *J. Electrochem. Soc.*, **137**(6),1887-1892, 1990.

[11] K. Reinhardt & W. Kern. Handbook of silicon wafer cleaning technology. *William Andrew*, 2008.

[12] J. Thomson. XLII. On certain curious motions observable at the surfaces of wine and other alcoholic liquors. *The London, Edinburgh, and Dublin Philosophical Magazine and Journal of Science*, **10** (67), 330:333, 1855.

[13] A.F.M. Leenaars, J.A.M. Huethorst, & J.J. van Oekel. Marangoni drying: A new extremely clean drying process. *Langmuir*, **6**, 1701:1703, 1990.

[14] J.B. Fournier & A.M. Cazabat. Tears of Wine. *Europhys. Lett.*, **20** (6), 517:522, 1992.

[15] T. Hattori. Ultrapure Water-Related Problems and Waterless Cleaning Challenges. *E.C.S. Trans.*, **34** (1), 371:376, 2011.

[16] S. Karpitschka & H. Riegler. Quantitative experimental study on the transition between fast and delayed coalescence of sessile droplets with different but completely miscible liquids. *Langmuir*, **26** (14), 11823:11829, 2010.

[17] R. Borcia, S. Menzel, M. Bestehorn, S. Karpitschka & H. Riegler. Delayed coalescence of droplets with miscible liquids: Lubrication and phase field theories. *Eur. Phys. J. E.*, **34** (3), 1:9, 2011.

[18] S. Karpitschka & H. Riegler. Noncoalescence of Sessile Drops from Different but Miscible Liquids: Hydrodynamic Analysis of the Twin Drop Contour as a Self-Stabilizing Traveling Wave. *Phys. Rev. Lett.*, **109** (6), 066103, 2012.

[19] S. Karpitschka & H. Riegler. Sharp transition between coalescence and noncoalescence of sessile drops. *J. Fluid Mech.*, **743**, 2014.

[20] W.D. Ristenpart, P.M. McCalla, R.V. Roy, & H.A. Stone. Coalescence of Spreading Droplets on a Wettable Substrate. *Phys. Rev. Lett.*, **97**, 064501:, 2006.

[21] R.D. Narhe, D.A. Beysens & Y. Pomeau. *Europhys. Lett.* **81**, 46002 (2008).

[22] M.W. Lee, D.K. Kang, S.S. Yoon & A.L.Yarin, Coalescence of two drops on partially wettable substrates. *Langmuir* **28**, 3791 (2012).

[23] L. Duchemin, J. Eggers, & C. Josserand. Inviscid coalescence of drops. *J. Fluid Mech.* **487**, 167:178 (2003).

[24] D.G. Aarts, H.N. Lekkerkerker, H. Guo, G.H. Wegdam, & D. Bonn. Hydrodynamics of droplet coalescence. *Phys. Rev. Lett.* **95**(16), 164503 (2005).

[25] R.W. Hopper. Plane Stokes flow driven by capillarity on a free surface. *J. Fluid Mech.* **213**, 349:375 (1990).

[26] J. Eggers, J.R. Lister, & H.A. Stone. Coalescence of liquid drops. *J. Fluid Mech.* **401**, 293:310 (1999).

[27] J.D. Paulsen, J.C. Burton, S.R. Nagel, S. Appathurai, M.T. Harris, & O.A. Basaran. The inexorable resistance of inertia determines the initial regime of drop coalescence. *P. Natl. Acad. Sci. USA* **109**(18), 6857:6861 (2012).

[28] J. Ahmad & R.S. Hansen. A simple quantitative treatment of the spreading of monolayers on thin liquid films. *J. Colloid Iinterf. Sci.*, **38**,(3) 601:604, 1972.

[29] D.P. Gaver & J.B. Grotberg. Droplet spreading on a thin viscous film. *J. Fluid Mech.*, **235**, 399:414, 1992.

[30] O.E. Jensen & J.B. Grotberg. Insoluble surfactant spreading on a thin viscous film: shock evolution and film rupture. *J. Fluid Mech.*, **240**, 25988, 1992.

[31] O.E. Jensen. Self-similar, surfactant-driven flows. *Phys. Fluids*, **6**, 108494, 1994.

[32] J.B. Grotberg & D.P. Gaver III. A Synopsis of Surfactant Spreading Research. *J. Colloid Iinterf. Sci.*, **178** (1), 377:378, 1996.

[33] O.K. Matar & S.M. Troian. Spreading of a surfactant monolayer on a thin liquid film: Onset and evolution of digitated structures. *Chaos*, **9** (1), 141:153, 1999.

[34] A. Hamraoui, M. Cachile, C. Poulard & A. M. Cazabat. Fingering phenomena during spreading of surfactant solutions. *Colloid. Surface. A*, **250** (13), 215: 221, 2004.

[35] Warner, M. R. E. and Craster, R. V. and Matar, O. K. Fingering phenomena created by a soluble surfactant deposition on a thin liquid film. *Physics of Fluids*, **16**(13), 2933:2951, 2004.

[36] D.W. Fallest, A.M. Lichtenberger, C.J. Fox & K.E. Daniels Fluorescent visualization of a spreading surfactant. *New J. Phys.*, **12**(7), 073029, 2010.

[37] E.R. Peterson & M. Shearer. Radial Spreading of a Surfactant on a Thin Liquid Film. *Applied Mathematics Research eXpress*, **2011**(1), 1:22, 2011.

[38] M Roché, Z. Li, I.M. Griffiths and S. Le Roux, I. Cantat and A. Saint-Jalmes & H.A. Stone. Marangoni Flow of Soluble Amphiphiles. *Phys. Rev. Lett.*, **112** (20), 208302, 2014.

[39] A.B. Afsar-Siddiqui, P. F. Luckham & O. K. Matar. Unstable Spreading of Aqueous Anionic Surfactant Solutions on Liquid Films. 2. Highly Soluble Surfactant. *Langmuir*, **19** (3), 703:708, 2003.

[40] A.A. Darhuber, & S.M. Troian. Marangoni driven structures in thin film flows. *Phys. Fluids*, **15** (9), S9:, 2003.

[41] O.K. Matar & R.V. Craster. Dynamics of surfactant-assisted spreading. *Soft Matter*, **5** (20), 3801:3809, 2009.

[42] R.V. Craster & O.K. Matar. Dynamics and stability of thin liquid films. *Rev. Mod. Phys.*, **81** (3), 1131:, 2009.

[43] C.W. Berendsen, J.C. Zeegers, G.C. Kruis, M. Riepen & A.A. Darhuber. Rupture of thin liquid films induced by impinging air-jets. *Langmuir*, **28** (26), 9977: 9985, 2012.

[44] C. Redon, F. Brochard-Wyart & F. Rondelez. Dynamics of dewetting. *Phys. Rev. Lett.*, **66** (6), 715, 1991.

[45] J.H. Snoeijer & J. Eggers. Asymptotic analysis of the dewetting rim. *Phys. Rev. E*, **82** (5), 11823:056314, 2010.

2

Coalescence of Viscous Sessile Drops

* *The coalescence of viscous drops on a substrate is studied experimentally and theoretically. We consider cases where the drops can have different contact angles, leading to a very asymmetric coalescence process. Side view experiments reveal that the "bridge" connecting the drops evolves with self-similar dynamics, providing a new perspective on the coalescence of sessile drops. We show that the universal shape of the bridge is accurately described by similarity solutions of the one-dimensional lubrication equation. Our theory predicts a bridge that grows linearly in time and stresses the strong dependence on the contact angles. Without any adjustable parameters, we find quantitative agreement with all experimental observations.*

2.1 Introduction

The coalescence or breakup of liquid drops is a fundamental process relevant for the formation of raindrops or sprays, inkjet printing, or stability of foams and emulsions [1–4]. The initial stages of coalescence of two spherical drops has been characterized in great detail [5–10]. After contact, a small liquid bridge connects the two drops and the bridge grows rapidly with time. Depending on the viscosity of the liquid, the radius of the bridge grows as $r \sim t$ (high viscosity) [5–8], or $r \sim t^{1/2}$ (low viscosity,

*Published as: J. F. Hernández-Sánchez, L. A. Lubbers, A. Eddi, and J. H. Snoeijer, "Symmetric and Asymmetric Coalescence of Drops on a Substrate", Phys. Rev. Lett. **109** (18), 184502, 2012.

inertia dominated) [7–9], with a crossover depending on fluid properties and drop size [10].

In many cases, however, the coalescing drops are not freely suspended but are in contact with a substrate. Much less is known about the coalescence of such sessile drops. When looking from a top view (perpendicular to the substrate), the coalescence of drops on a substrate looks very similar to the case for spherical drops [3]; yet the bridge dynamics is fundamentally different. Measurements of the top view radius of the bridge r for very viscous drops give a growth $r \sim t^{1/2}$ [11, 12], and even smaller exponents have been suggested [13]. The challenge lies in the complications introduced by the presence of the substrate. First, the geometry of the drop is no longer a sphere with an axisymmetric bridge, but a spherical cap with a contact angle θ. As a consequence, a top view of the coalescence process is very different from a side view. Second, the wall slows down the liquid transport towards the bridge [11] and gives rise to the motion of a contact line [14]. At present, it is not clear whether or not this contact line motion affects the initial stages of coalescence, and different predictions for the θ dependence have been reported [11–13]. Based on numerical simulations it was argued that the main direction of the flow is towards the neck, and that the flow perpendicular to the view shown in Fig. 2.1 can be neglected [11]. While this simplifies the description of the coalescence, this hypothesis remains to be validated experimentally.

In this Chapter we resolve the coalescence of viscous drops on a substrate by performing side view experiments, imaging parallel to the substrate (Fig. 2.1). Our central finding is that the initial stages evolve by a self-similar shape of the bridge, with a linear growth of the bridge height $h_0 \sim t$. The influence of the contact angle is studied in detail by considering drops with identical or different contact angles, resulting into symmetric or asymmetric coalescence [Fig. 2.1(b, c)]. Theoretically, we show that all experiments are described quantitatively by the one-dimensional lubrication, assuming that the bridge height (side view) evolves independently from its width (top view). We identify similarity solutions that quantitatively predict the shape and evolution of the bridge without adjustable parameters. This confirms the hypothesis by Ristenpart *et al.* [11] that the coalescence is governed by liquid flux from the drop into the neck. Our results reveal that the rate of vertical growth scales with the contact angle as $\sim \theta^4$, the horizontal speed $\sim \theta^3$, and provide a new perspective on previous top view measurements.

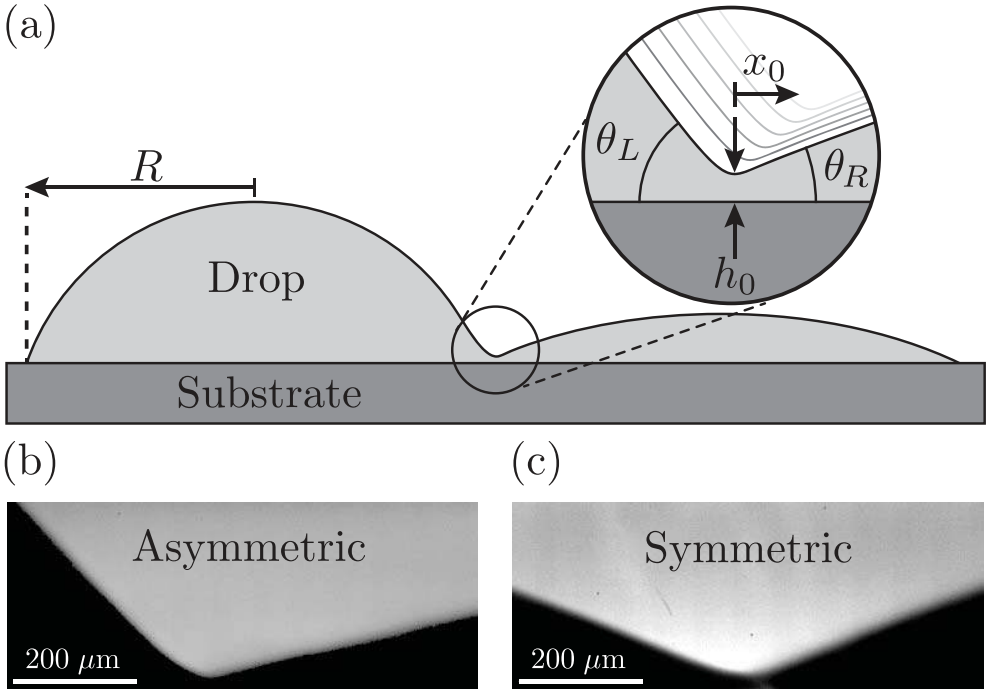

Figure 2.1: (a) Schematic of two coalescing viscous drops on a substrate, viewed from the side. The minimum height $h_0(t)$ characterizes the bridge size. The left-right contact angles θ_L and θ_R can be different at the moment of contact. The horizontal displacement x_0 results from the asymmetry in the contact angles. (b, c) Typical frames of the experiments are shown for asymmetric contact angles (b) and symmetric contact angles (c).

2.2 Experimental setup

The side view images of coalescing drops in Fig. 2.1(b, c) are obtained by a digital video camera (Photron APX-RS) equipped with a microscopic lens (Navitar 12x zoom lens), resulting in a resolution of 2 μm/pixel. The camera recorded 12.5 frames per second. The substrate consists of a horizontal microscope glass slide (Menzel pre cleaned microscope slide, average roughness ≈ 10 nm). The glass slide was further cleaned using ethanol and acetone, then submerged in an ultrasonic bath and dried with filtered nitrogen gas. The coalescing drops were made from silicon oils (Basildon Chemical Company Limited), with viscosity $\eta = 0.974$ Pa$\cdot$s or 12.2 Pa$\cdot$s, which both have a surface tension $\gamma = 21 \cdot 10^{-3}$ N$\cdot$m^{-1} and density $\rho = 975$ kg$\cdot$m^{-3}.

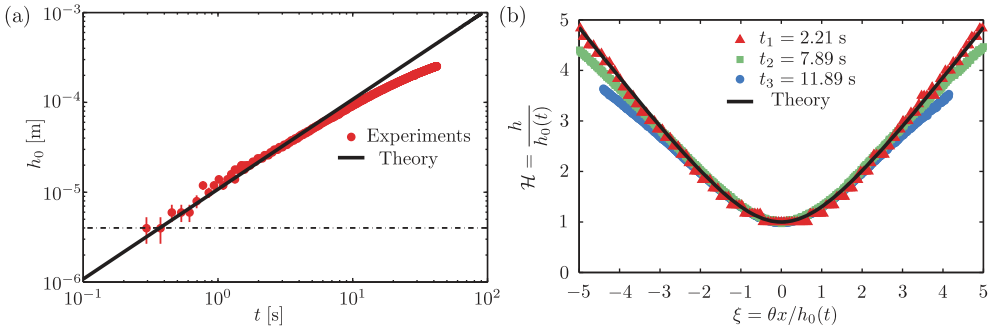

Figure 2.2: Symmetric coalescence. (a) Height of the bridge h_0 as a function of time after contact t, for drops with $\theta_L = \theta_R = 22^\circ$ ($\eta = 12.2$ Pa$\cdot$s). Experiments are shown in red (●), the solid line is the prediction by Eqs. (2.2,2.3). The dashed line represents the lower limit for spatial resolution. (b) Rescaled experimental profiles at different times, $\mathscr{H} = h(x,t)/h_0(t)$ versus $\xi = x\theta/h_0(t)$. The collapse reveals self-similar dynamics at the early stage of coalescence, in agreement with the similarity solution (solid line).

The silicon oils perfectly wet the cleaned glass slide ($\theta_{eq} \approx 0$).

The coalescence of two drops is controlled as follows. A first drop is deposited from the syringe on the substrate. Although the silicon oil perfectly wets the glass, the spreading of these high viscosity drops is very slow, with the liquid contact angle decreasing slowly in time. Subsequently, the glass plate is displaced by a manual translation stage and a second drop is placed next to the first one. By controlling the volume of silicon oil and the time between the deposition of drops we achieve a range of contact angles θ_L and θ_R between 10° to 67° at the time of coalescence. We consider both symmetric coalescence [$\theta_L = \theta_R$, Fig. 2.1(c)] and asymmetric coalescence [$\theta_L \neq \theta_R$, Fig. 2.1(b)]. The spreading determines the initial conditions, but in all cases the spreading speed is much smaller than the growth of the bridge. We verified that the weak spreading does not influence our results by performing some experiments under partially wetting conditions, for which the coalescence was started from equilibrium.

Contact time is determined when there is a visual change, which happens before the bridge is thick enough to provide a reliable measurement. The dashed line in Fig. 2.2(a) shows this spatial resolution limit.

2.3 Self-similar dynamics

The dynamics of coalescence is characterized by the growth of the bridge connecting the two drops. Figure 2.2(a) presents the height of the bridge h_0 defined in Fig. 2.1, as a function of time for a symmetric coalescence experiment ($\theta_L = \theta_R = 22^\circ$). At early times, we observe a linear increase of the bridge height, *i.e.* $h_0 \sim t$, while at later times the coalescence slows down. In these final stages the height of the bridge becomes comparable to the total drop size, which is typically ~ 1 *m*m for all experiments. The very early stage, however, exhibits self-similar dynamics that is governed by a single length scale. This is revealed in Fig. 2.2(b) where the meniscus profiles, $h(x,t)$, and the horizontal coordinate, x, are rescaled by $h_0(t)$. The scaled profiles at different times collapse onto a universal curve: the early stages of coalescence are characterized by a self-similar meniscus profile. The size of the bridge is simply h_0, both in horizontal and vertical direction. The solid line is the theoretical similarity profile that will be derived below.

Our experiments suggest that coalescence of drops on a substrate is governed by a similarity solution of the flow. To simplify the three-dimensional geometry of the coalescence, we assume that the flow is predominantly oriented from the centers of the drops towards the coalescing bridge, as suggested by Ristenpart *et al.* [11]. We therefore attempt a similarity solution based on the one-dimensional lubrication theory for viscous flows [15] (see also Appendix A),

$$\frac{\partial h}{\partial t} + \frac{\gamma}{3\eta}\frac{\partial}{\partial x}\left(h^3\frac{\partial^3 h}{\partial x^3}\right) = 0. \tag{2.1}$$

Here, $h(x,t)$ is the meniscus profile viewed from the side, η is the liquid viscosity and γ denotes the surface tension. This lubrication equation is valid for small contact angles and represents mass conservation: the second term is the surface tension-driven flux of liquid towards the bridge, causing a growth of the bridge ($\partial h/\partial t > 0$). A direct comparison with side view experiments will test the validity of the one-dimensional assumption.

Consistent with our experiments, Eq. (2.1) has a similarity solution that imposes a linear time-dependence,

$$h(x,t) = vt\,\mathscr{H}(\xi), \quad \text{with} \quad \xi = \frac{\theta x}{vt}, \tag{2.2}$$

where $\mathscr{H}(\xi)$ is the similarity profile of the meniscus bridge. Here we incorporated

the contact angle θ in the scaling of x, such that the condition $\partial h/\partial x = \theta$ translates to $\mathscr{H}' = 1$. The correct scaling of the coalescence velocity with θ then turns out to be

$$v = V\frac{\gamma\theta^4}{3\eta}, \tag{2.3}$$

where V is a numerical constant that still needs to be determined. In combination with (2.1) and (2.2), this provides an ordinary differential equation (ODE) for the similarity profile $\mathscr{H}(\xi)$:

$$\mathscr{H} - \xi\mathscr{H}' + \frac{1}{V}\left(\mathscr{H}^3\mathscr{H}'''\right)' = 0. \tag{2.4}$$

In order to solve Eq. (2.4), which is a fourth order ODE with one unknown parameter V, five boundary conditions are required. At the center of the symmetric bridge

$$\mathscr{H}(0) = 1, \quad \mathscr{H}'(0) = \mathscr{H}'''(0) = 0, \tag{2.5}$$

while far away the profile has to match a linear slope of contact angle θ. For the similarity variables this becomes

$$\mathscr{H}''(\infty) = 0, \quad \mathscr{H}'(\infty) = 1. \tag{2.6}$$

The boundary value problem (2.4-2.6) uniquely determines the similarity solution for symmetric drop coalescence. It was solved numerically using a shooting algorithm, from which we obtained both the dimensionless velocity, $V = 0.818809$, and the similarity profile $\mathscr{H}(\xi)$ – See also Appendix B. As the influence of the contact angle was scaled out, the solution describes the coalescence for all contact angles, within the lubrication assumption of small θ.

The similarity solution indeed provides an accurate description of the coalescence experiments. The solid line in Fig. 2.2(a) is the prediction (2.3) without adjustable parameters. The solid line in Fig. 2.2(b) is the similarity profile $\mathscr{H}(\xi)$ obtained from our analysis. The agreement between experiment and theory shows that the initial stages of coalescence are accurately described by a one-dimensional lubrication model. As expected, the similarity solution breaks down at later times when the size of the meniscus bridge becomes comparable to the size of the drops – See also Appendix A.

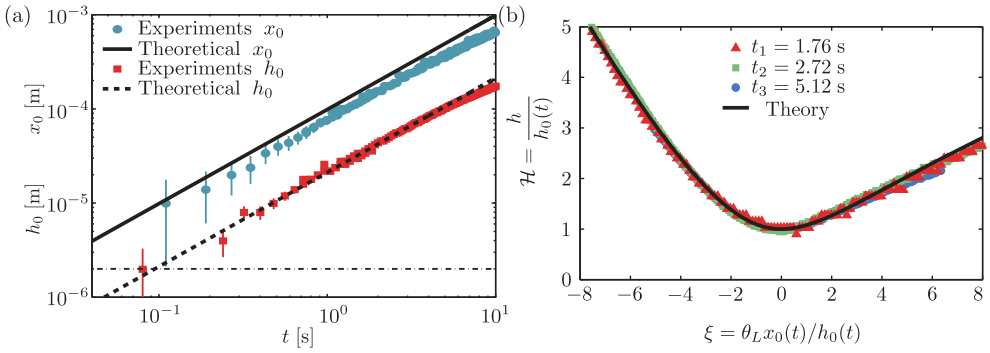

Figure 2.3: Asymmetric coalescence. (a) Horizontal and vertical position of the meniscus bridge, $x_0(t)$ and $h_0(t)$, for asymmetric drops ($\theta_L = 46°$, $\theta_R = 13°$, viscosity $\eta = 12.2\,\mathrm{Pa}\cdot\mathrm{s}$). Blue (●) and red (■) markers are experimental data for x_0 and h_0 respectively. Solid and dashed lines are the predictions from the similarity solutions. (b) Rescaled experimental profiles at different times, $\mathscr{H} = h(x,t)/h_0(t)$ versus $\xi = x_0\theta_L/h_0(t)$. The collapse reveals self-similar dynamics at the early stage of coalescence. The solid line is the similarity solution predicted by our analysis.

2.4 Asymmetric coalescence

We further extend the theory to asymmetric coalescence, for which the contact angles $\theta_L \neq \theta_R$ (Fig 2.1). Without loss of generality, we assume that $\theta_L > \theta_R$, and scale the coordinates using θ_L. Interestingly, the lack of symmetry induces a *horizontal* displacement of the meniscus bridge during the coalescence process: the minimum of the bridge, x_0, is pulled towards the lower contact angle (θ_R). This effect can be captured using a similarity variable that is co-moving with the bridge, of the form

$$\xi = \frac{\theta_L(x-ut)}{vt}, \quad \text{with} \quad u = U\frac{\gamma\theta_L^3}{3\eta}. \tag{2.7}$$

The horizontal velocity of coalescence u scales with θ_L^3, where U is a numerical constant. The vertical velocity still follows (2.3) with $\theta = \theta_L$. Inserting (2.7) in (2.1) yields

$$\mathscr{H} - \left(\xi + \frac{U}{V}\right)\mathscr{H}' + \frac{1}{V}\left(\mathscr{H}^3\mathscr{H}'''\right)' = 0. \tag{2.8}$$

This fourth order ODE for $\mathscr{H}(\xi)$ now contains two unknown parameters, U and V,

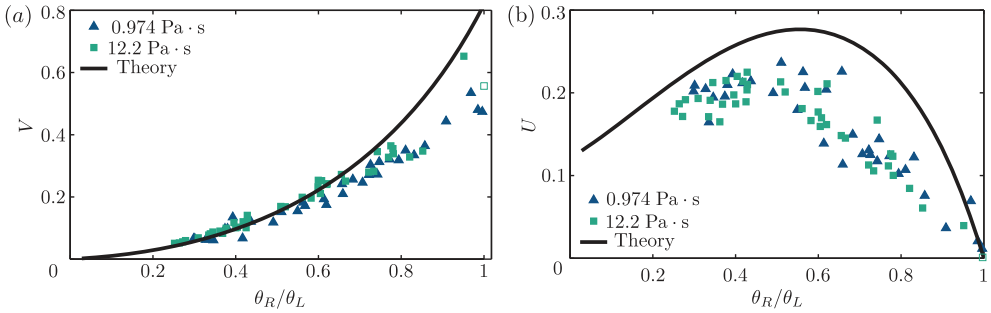

Figure 2.4: Contact angle dependence of coalescence velocity. (a) Dimensionless vertical speed, $V = 3v\eta/(\gamma\theta_L^4)$, as a function of θ_R/θ_L. (b) Dimensionless horizontal speed, $U = 3u\eta/(\gamma\theta_L^3)$, as a function of θ_R/θ_L. The horizontal speed vanishes for the symmetric case $\theta_R/\theta_L = 1$, and displays a maximum around $\theta_L/\theta_R \sim 0.5$. Closed symbols: 75 experiments on completely wetting substrate. Open symbols: drops on partially wetting substrate $\theta_{eq} = 55°$. Solid lines: similarity solutions.

hence the solution requires six boundary conditions. The minimum of the bridge is still defined by $\mathscr{H}(0) = 1$, $\mathscr{H}'(0) = 0$, but the symmetry condition on $\mathscr{H}'''$ no longer applies. Instead, one has to impose $\mathscr{H}''(-\infty) = \mathscr{H}''(\infty) = 0$, with contact angles

$$\mathscr{H}'(-\infty) = -1, \quad \mathscr{H}'(\infty) = \theta_R/\theta_L. \tag{2.9}$$

The resulting boundary value problem has a unique solution for each ratio θ_R/θ_L, selecting both U and V.

Figure 2.3 compares theory and experiment for an asymmetric coalescence ($\theta_R/\theta_L = 0.25$). The horizontal position of the bridge x_0 (blue circles) and the vertical position of the bridge h_0 (red squares) are shown in Fig. 2.3(a). These again evolve linearly in time with a well-defined velocity. The solid and dashed lines are the predictions (2.3,2.7), with prefactors U and V determined from the similarity solution. Figure 2.3(b) confirms that the asymmetric experimental profiles indeed display self-similarity (symbols), in excellent agreement with theory (solid line).

We finally consider the influence of the contact angle on the coalescence speed. Our theory suggests a universal behavior when making the horizontal and vertical velocities dimensionless, according to $U = 3u\eta/(\gamma\theta_L^3)$ and $V = 3v\eta/(\gamma\theta_L^4)$. The results of 75 experiments are summarized in Fig. 2.4 and compared to the theoretical predic-

tion. Indeed, we observe a good collapse of the data. The open symbol corresponds to a case where the substrate is partially wetting. The agreement with the (slowly) spreading drops shows that the initial coalescence is governed by the neck geometry, not by the substrate wettability. An interesting feature is that the theory predicts an optimal horizontal speed around $\theta_R/\theta_L \approx 0.5$, which is verified experimentally.

This maximum horizontal velocity can be explained as follows. The asymmetry induces a bias in the pulling force of surface tension, which is more efficient for the smaller contact angle θ_R. However, the "lubrication effect" inhibits liquid transport when $\theta_R \to 0$, as the viscous friction in the liquid increases for smaller angles. The combination of these two effects gives rise to an optimum ratio θ_R/θ_L.

2.5 Discussion

Our results imply that the initial coalescence of drops on a substrate, which is manifests three-dimensionally, is described quantitatively by a one-dimensional model. This can be explained from the cross-section of the bridge perpendicular to our viewpoint, r, which is much larger than h_0. Elementary geometry suggests $r \sim (Rh_0/\theta)^{1/2}$ [12], R being the footprint radius of the drop on the substrate. At early times we therefore have $r \gg h_0$, such that local gradients will be oriented in the x direction. This is consistent with numerical characterization of the flow field [11].

It would be interesting to see whether the one-dimensional approach also applies for coalescence of low-viscosity drops, which are dominated by inertia rather than viscosity [2, 16].

Appendix A: Numerical solutions

In this Appendix we briefly derive the lubrication equation and perform a numerical solution of the time evolution of the bridge growth. This provides a further motivation for the emergence of similarity solutions as discussed in the main text, and their breakdown at later times when the bridge height becomes comparable to the drop height.

For the derivation we start from the two-dimensional conservation of volume equation

$$\frac{\partial h}{\partial t}+\frac{\partial Q}{\partial x}=0, \tag{2.10}$$

where t is the time, x is the horizontal position, h is the height of the film and Q is the volumetric flow rate. The flow rate Q is calculated from a laminar viscous flow in 2D and for a no-shear free surface (*i.e.* no Marangoni forces) is expressed as

$$Q=-\frac{h^3}{3\eta}\frac{\partial P}{\partial x}, \tag{2.11}$$

where η is the viscosity and $\partial P/\partial x$ is the pressure gradient. The pressure has two components, one from the linearized Young-Laplace equation $P_L=-\gamma\,\partial^2 h/\partial x^2$ and the hydrostatic pressure $P_h=\rho g h$. We ignore the influence of the disjoining pressure. The pressure gradient then becomes

$$\frac{\partial P}{\partial x}=-\gamma\frac{\partial^3 h}{\partial x^3}+\rho g\frac{\partial h}{\partial x}, \tag{2.12}$$

And the general lubrication approximation equation becomes

$$\frac{\partial h}{\partial t}-\frac{\partial}{\partial x}\left[\frac{h^3}{3\eta}\left(\gamma\frac{\partial^3 h}{\partial x^3}-\rho g\frac{\partial h}{\partial x}\right)\right]=0. \tag{2.13}$$

By neglecting the effect of gravity in Eq. 2.13 we recover Eq. 2.1. If these equations are solved for steady state ($\partial h/\partial t=0$), a natural difference arises between Eq. 2.13 we recover Eq. 2.1. On the one hand, the solution of Eq. 2.1 leads to a inverted parabola, which is in contact with the substrate at two points, *i.e.* it has two contact lines. On the other hand, the solution of Eq. 2.13 yields to an exponential behavior that far away from the origin naturally converges to a constant thickness due to the influence of gravity. The thickness is of the order of the capillary length $l_c=(\gamma/\rho g)^{1/2}$. Unlike in Eq. 2.1, the solution for Eq. 2.13 that matches to the finite thickness has only a single with the contact line at the origin. By using this steady state solution as an initial condition for the coalescence of two sessile layers of liquid, brought into contact where the two layers meet, a model for the contact line in the edges is no needed and simplifies the numerical simulations. The characteristic length and time of this problem are the capillary length and the characteristic time $t_c=3\eta l_c/\theta^3\gamma$. These are used to nondimensionalize Eq. 2.13. The horizontal and vertical components are scaled with the capillary length l_c and the contact angle θ, leading to the dimensionless position $X=x/l_c$, height $H=h/\theta l_c$ and time $T=t/t_c$. This scaling transforms Eq. 2.13 to

$$\frac{\partial H}{\partial T} = \frac{\partial}{\partial X}\left[H^3\left(\frac{\partial^3 H}{\partial X^3} - \frac{\partial H}{\partial X}\right)\right], \tag{2.14}$$

which was solved using an implicit numerical method on a linear grid. The result of computing the height of the bridge $H(0)$ is presented in Fig. 2.5(a) as a blue curve. The linear prediction from the similarity theory is shown as a solid black line. There is a perfect match, up to the point where the height of the bridge becomes of the same order of magnitude as the film height, *i.e.* when $H(0) \sim 0.1$. The same "slowing down" is observed for the experimental results, when the bridge height reaches the size of the drop. Fig. 2.5(b) presents a comparison between the height profiles from the numerical simulations, compared with the self-similarity profile as a black solid line. Here it can be observed that the numerical profiles collapse to the self-similar for the very early times.

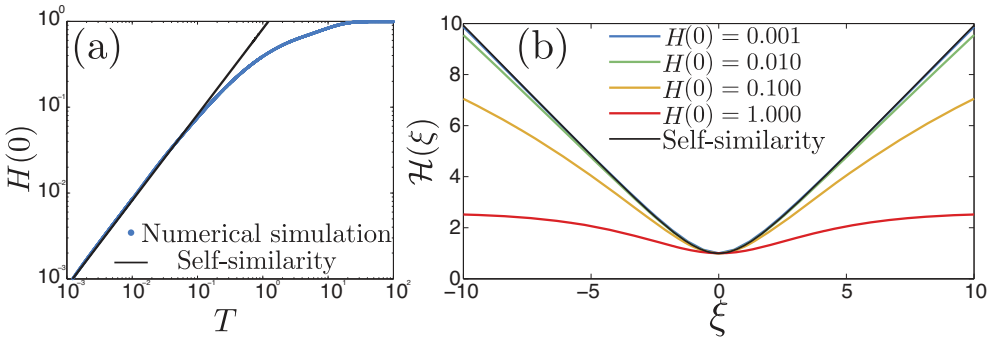

Figure 2.5: Results of the numerical simulations compared with the self-similarity solution. (a) The dimensionless height of the bridge $H(0)$ as a function of the dimensionless time T is plotted in blue, while the solid black line is the similarity solution. (b) Numerically simulated height profiles at different times compared with the self-similarity solution in black solid line. The dimensionless times are $H(0) = 0.001$, $H(0) = 0.01$, $H(0) = 0.1$ and $H(0) = 1$.

Appendix B: Shooting method for the similarity solution

In this Appendix we describe the shooting algorithm used to compute the similarity profiles and the values of the dimensionless velocities U and V.

Symmetric contact angles

The self-similar profile of the coalescence of viscous sessile drops is described by Eq. 2.4. The solution to this fourth order ODE with an unknown parameter, requires five boundary conditions. We calculate the value of these parameters using a shooting method. The reason is that in our boundary value problem only the three initial conditions of Eq. 2.5 are known, leaving the initial value of the second derivative $\mathscr{H}''(0)$ and the velocity V unknown (note that throughout this appendix we refer to the condition at $\xi = 0$ as the "initial" condition). These have to be determined from imposing the additional boundary conditions of Eq. 2.6, using a shooting procedure. Essentially, for any value of V that gives with $\mathscr{H}''(\infty) = 0$, the value of $\mathscr{H}'(\infty)$ dictates how $\mathscr{H}''(0)$ must be adapted. The value at $\xi \to \infty$ is taken at a sufficiently large value, such as $\xi = 100$. More specifically, for a starting value of V, we use an *ansatz* to select a lower and upper limits for $\mathscr{H}''(0)$ that contains solutions with the desired $\mathscr{H}''(\infty) = 0$. This range of values is narrowed iteratively by taking the midpoint, and comparing $\mathscr{H}''(\infty)$ to its desired value. This process is systematically repeated until the difference between the boundaries is smaller than a threshold value. Similarly, this systematic process is repeated narrowing the predefined range of values of V, as the value of $\mathscr{H}'(\infty)$ gets continuously closer to its desired value ($\mathscr{H}'(\infty) = 1$).

Asymmetric contact angles

The algorithm to calculate the initial conditions and the unknown values of the asymmetric coalescence is different. Here, the additional parameter U as well as the asymmetry change the boundary conditions. In this case, only two conditions at $\xi = 0$ are defined, and four boundary conditions at $\xi = \infty$ are necessary to select the values of U, V, $\mathscr{H}''(0)$ and $\mathscr{H}'''(0)$. In the current algorithm, the value U determines the asymmetry of the profile, selecting the ratio θ_R/θ_L. For the range of values predefined, the initial value of the third derivative $\mathscr{H}'''(0)$ is calculated. The result then is compared with the criteria

$$\int_{-\infty}^{\infty} \mathscr{H}'''(\xi) d\xi = \mathscr{H}''(-\infty) - \mathscr{H}''(\infty) = 0. \tag{2.15}$$

Since Eq. 2.15 is correct, we can argue that if $\mathscr{H}''(-\infty) - \mathscr{H}''(\infty) < 0$, the initial value of the third derivative $\mathscr{H}'''(0)$ should increase to satisfy Eq. 2.15. If $\mathscr{H}''(-\infty) - \mathscr{H}''(\infty) > 0$, the initial value of the third derivative $\mathscr{H}'''(0)$ should also decrease. These criteria is used to systematically narrow a range *a priori* defined for the initial values of the third derivative $\mathscr{H}'''(0)$. After calculating the new range

containing the values of $\mathscr{H}'''(0)$, we proceed to compute the initial value of the second derivative $\mathscr{H}''(0)$. Here, the value of $\mathscr{H}''(\infty)$ is selected by $\mathscr{H}''(0)$ and the criteria used is similar to the one presented on the algorithm used for the symmetric drops. With the selected values of the initial conditions of $\mathscr{H}'''(0)$ and $\mathscr{H}''(0)$, we proceed to find the value of V. The boundary value of the first derivative $\mathscr{H}'(\infty)$ must be equal to one, and this must be guarantied by the correct selection of the dimensionless velocity V. Moreover, for the case of the asymmetric coalescence, V is not single-valued as it can be calculated for both sides of the height profile in 2.6(a). If these values exist and are not the same, the value of the third derivative should be recomputed. This process is used to find values smaller than a certain threshold $U < U_{max}$, being $U_{max} = 0.2766$. In Fig. 2.6 we show different profiles of $\mathscr{H}(\xi)$ calculated for continuously increasing values of U at different ranges. The two plots in Fig. 2.6 present different ranges of the similarity variable with equal of contact angles ratios. Fig. 2.6(a) displays a large range of the similarity variable ξ and the bridge profile $\mathscr{H}(\xi)$. This image shows that far away from the origin the boundary conditions are preserved. Fig. 2.6(b) presents a close up to the curves in Fig. 2.6(a) and displays the smooth curvature of the profile that represents the bridge between the drops.

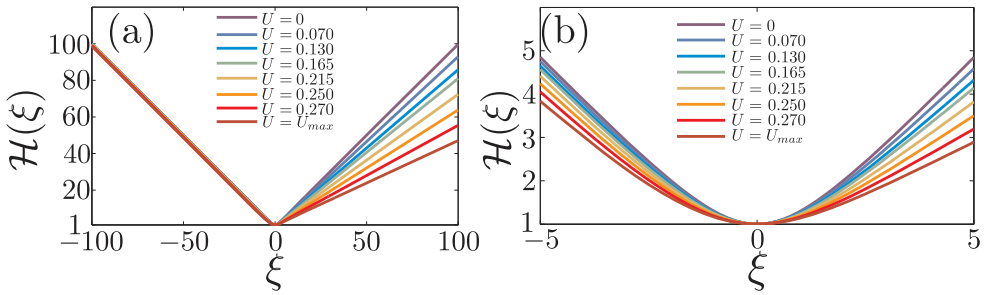

Figure 2.6: (a) The similarity profile $\mathscr{H}(\xi)$ for different asymmetries of the contact angle. It is observed that the value of U selects the contact angle asymmetry θ_R/θ_L. The range of the similarity variable ξ is comprehended between -100 and 100. (b) The similarity profile for different asymmetries observed from a closer view. The value of U_{min} resulted from the numerical method.

References

[1] J. Eggers, Rev. Mod. Phys. **69**, 865 (1997).

[2] N. Kapur and P. H. Gaskell, Phys. Rev. E **75**, 056315 (2007).

[3] C. Andrieu and D. Beysens and V. S. Nikolayev and Y. Pomeau, J. Fluid Mech. **453**, 427 (2002).

[4] M. P. Brenner and X. D. Shi and S. R. Nagel, Phys. Rev. Lett. **73**, 3391 (1994).

[5] J. Eggers and J. R. Lister and H. A. Stone, J. Fluid Mech. **401**, 293 (1999).

[6] R. W. Hopper, J. Fluid Mech. **213**, 349 (1990).

[7] S. T. Thoroddsen and K. Takehara and T. G. Etoh, J. Fluid Mech. **527**, 85 (2005).

[8] D. G. A. L. Aarts and H. N. W. Lekkerkerker and Hua Guo and G. H. Wegdam and D. Bonn, Phys. Rev. Lett. **95**, 164503 (2005).

[9] L. Duchemin and J. Eggers and C. Josserand, J. Fluid Mech. **487**, 167 (2003).

[10] J. D. Paulsen and J. C. Burton and S. R. Nagel, Phys. Rev. Lett. **106**, 114501 (2011).

[11] W. D. Ristenpart and P. M. McCalla and R. V. Roy and H. A. Stone, Phys. Rev. Lett. **97**, 064501 (2006).

[12] R. D. Narhe and D. A. Beysens and Y Pomeau, Europhys. Lett. **81**, 46002 (2008).

[13] M. W. Lee and D. K. Kang and S. S. Yoon and A. L. Yarin, Langmuir **28**, 3791 (2012).

[14] D. Bonn and J. Eggers and J. Indekeu and J. Meunier and E. Rolley, Rev. Mod. Phys. **81**, 739 (2009).

[15] A. Oron and S. H. Davis and S. G. Bankoff, Rev. Mod. Phys. **69**, 931 (1997).

[16] J. Billingham and A. C. King, J. Fluid Mech. **533**, 193 (2005).

[17] S. Karpitschka and H. Riegler, Langmuir **26**, 11823 (2010).

3

Marangoni spreading due to a localized alcohol supply on a thin water film

* *Bringing two miscible fluids into contact naturally generates strong gradients in surface tension. Here we investigate such a Marangoni-driven flow by continuously supplying isopropyl alcohol (IPA) on a film of water, using micron-sized droplets of IPA-water mixtures. These droplets create a localized depression in surface tension that leads to the opening of a circular, thin region in the water film. At the edge of the thin region there is a growing rim that collects the water of the film, reminiscent of Marangoni spreading due to locally deposited surfactants. In contrast to the surfactant case, the driving by IPA-water drops gives rise to a dynamics of the thin zone that is independent of the initial layer thickness. The radius grows as $r \sim t^{1/2}$, which can explained from a balance between Marangoni and viscous stresses. We derive a scaling law that accurately predicts the influence of the IPA flux as well as the thickness of the thin film at the interior of the spreading front.*

*Submitted to Phys. Fluids as J. F. Hernández-Sánchez, A. Eddi, and J. H. Snoeijer, Marangoni spreading due to a localized alcohol supply on a thin water film.

3.1 Introduction

Liquids of spatially inhomogeneous composition will exhibit surface tension gradients, which induces nontrivial flow. A famous example of such a Marangoni flow are the tears of wine [1], where selective evaporation of alcohol is at the origin of complicated droplet patterns. A similar effect is exploited in the industrial technique called Marangoni drying, where the Marangoni forces due to vapor adsorption induces local gradients in composition [2, 3]. This is an effective technique for achieving very clean surfaces, of particular importance in semiconductor industry. Though substantial theoretical understanding was achieved [4, 5], some unexpected coalescence phenomena were recently reported. When two miscible droplets of different chemical composition are brought into contact, the Marangoni forces can delay or prevent actual coalescence [6–10]. The coalescence is frustrated by the very localized gradient of surface tension in the "neck" region. In contrast to the growth of the neck as in normal coalescence [11–14], the drops exhibit a translational motion where the drop of larger surface tension pulls the other drop over the substrate [7, 9].

The purpose of the present work is to investigate the Marangoni flow by localized deposition of alcohol on a thin water film. These droplets create a localized depression in surface tension that leads to the opening of a circular, thin region in the water film. This is a geometry that has been extensively studied for surfactants, creating a similar surface tension gradient and radially outward flow [15–28]. This class of experiments is called "surfactant spreading", that typically exhibits power-law dynamics of the spreading radius versus time, i.e. $r \sim t^{\alpha}$. Many different cases have been identified, leading to a variety of exponents: Surfactants can be soluble or insoluble, can be supplied at different rates and in different geometries, while the supporting film can be deep or thin. Recently, the Marangoni flow of soluble surfactants on a deep pool was suggested as a tool to efficiently measure surfactant properties [23]. Most similar to our present study is the axisymmetric spreading on thin films, which for spreading of a fixed amount of surfactant and from a continuous source, respectively, leads to $r \sim t^{1/4}$ [16, 20, 22, 24, 25, 29–32] and $r \sim t^{1/2}$ [28]. In all cases, the spreading was observed to be faster on films of larger thickness [33–35].

In this Chapter, we experimentally determine the scaling law for the Marangoni spreading due to a continuous flux of miscible liquid (IPA-water mixture) on a water film. It is found that for all conditions $r \sim t^{1/2}$, while accurate control over the liquid composition and deposition allows us to quantify how the prefactor of this law depends on the experimental parameters. Interestingly, this gives a different picture than expected in comparison to the case of surfactant spreading. Based on our de-

tailed measurements we can derive a scaling theory that captures all observations. In section 2 we describe the experimental setup, the measurements and the calibrations required to achieve well controlled quantitative experiments. In section 3 we present measurements of the radius of the opening hole as a function of time for different conditions. Here we present the scaling arguments that describe the process as the dynamic balance between the Marangoni and viscous stresses. The Chapter ends with a Discussion in section 4.

3.2 Experimental setup

We start by describing the experimental setup, measurement procedure and necessary calibrations. Two steps were followed for each experiment. First, a water layer of uniform thickness is deposited on a hydrophilic substrate using a spin coater [Fig. 3.1(a)]. The thickness h_0 is varied from 8 to 70 microns, where h_0 is determined using a high-resolution spectrometer (Ocean optics HR4000). The substrate consists of a silica glass slide ($71 \times 71m$m), which is made hydrophilic using the cleaning procedure described in the Appendix. This cleaning step is critical to achieve reproducible results. Second, the substrate with the film is placed on the inverted microscope (Zeiss Axiovert 25), with a high speed color camera (Photron SA2) recording the bottom view [Fig. 3.1(b)]. A Marangoni flow is created by a continuous supply of micron-sized drops of an IPA-water mixture, deposited on top of the water film. The IPA-water mixture has a lower surface tension than water, giving rise to localized depression of surface tension and hence Marangoni forces. As seen in Fig. 3.1(c-f), these forces induce a radially outward flow in the form of a circular traveling front, leaving behind a liquid layer much thinner than the initial thickness. The small drops that are deposited at the center of the images have negligible inertia, ensuring that this radial spreading is solely driven by Marangoni forces. While the growth of the circular front is reminiscent of the classical "dewetting hole" (dry circular patches on partially wetting surfaces Brochard-Wyart and de Gennes [36]), a key difference is that here the substrate is perfectly wetting and a macroscopic liquid film remains in the interior.

The goal of the experiment is to reveal the dynamics of the spreading radius $r(t)$, as a function of the control parameters of the experiment. The spreading radius is defined as the backside of the rim, as shown in Fig. 3.1(b). Through image analysis, we measure the spreading radius in the recordings. The concentric rings in the inner region appear due the constructive light interference. Using the color interferometry technique reported by [37], the fringes provide a measurement of the film thickness in

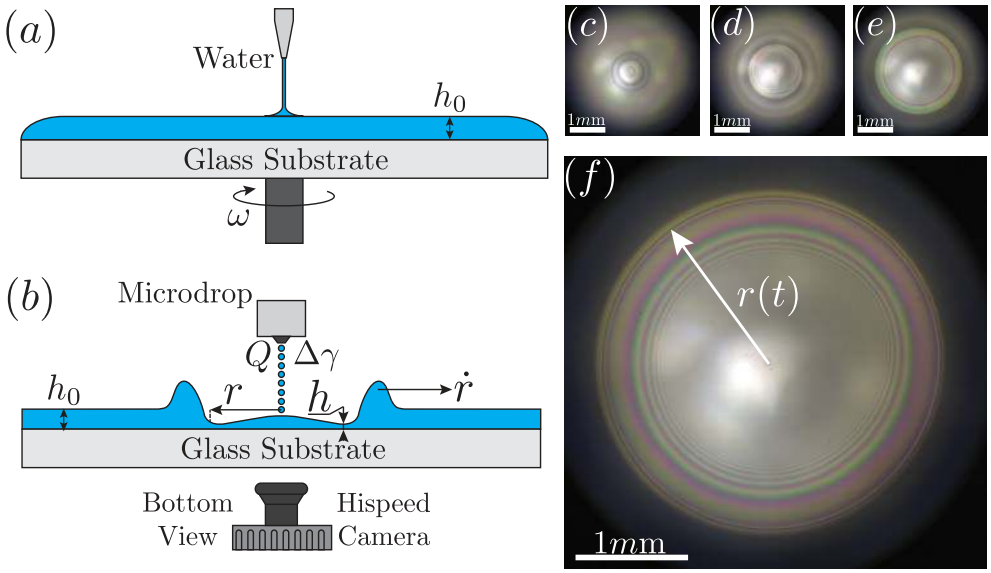

Figure 3.1: (a) Sketch of the spin coater setup, depositing a uniform film of water of thickness h_0. (b) Sketch of the radial spreading dynamics viewed as cross-section. After placing the substrate on the inverted microscope, a color high speed camera is used to record the process. A microdrop nozzle shoots droplets ($d \sim 50\mu$m) with controlled frequency of an IPA-water mixture on the water layer. The flux Q of IPA-water induces a surface tension difference $\Delta\gamma$. ($c-f$) Bottom view of the typical experiment image from the inverted microscope at times $t = 5ms$, $t = 37ms$, $t = 97ms$, $t = 157ms$. The experimental conditions are $h_0 = 14\mu$s, $Q = 157n$L/s, 1% IPA (Vol). The interferometry patterns are the result of a small thickness in the region behind the outward moving front.

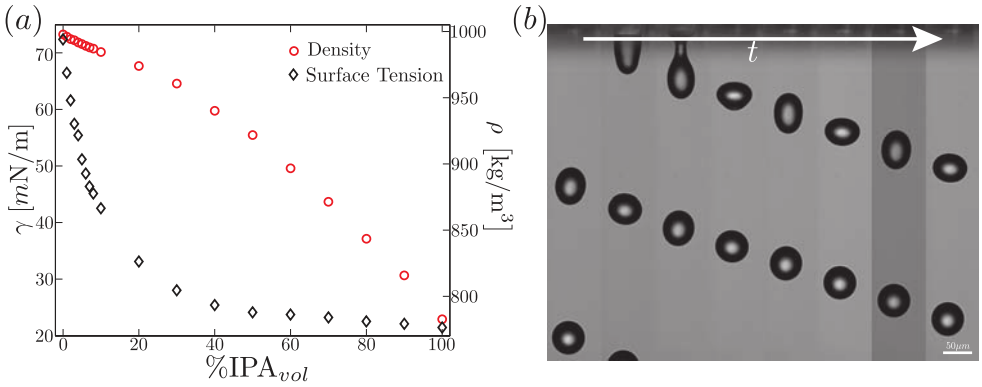

Figure 3.2: (*a*) Calibration of the density (◯, right vertical axis) and the surface tension(◇, left vertical axis) as a function of IPA concentration. (*b*) Visualization of the generation of microdrops, obtained using iLIF technique developed by [39]. From these type of images, we could determine the range over which the monodisperse train of droplets was generated, and determine the corresponding flow rates Q.

the thinnest region. We performed experiments by systematically varying the initial film thickness h_0, the flow rate of the IPA-water drops Q, as well as the composition of the IPA-water mixture. By changing the composition, we vary the surface tension and the density as has been calibrated in Fig. 3.2(*a*). The density and the surface tension were measured using a density-meter (DM A35 from Anton Paar) and the pendant drop method (tensiometer OCA15 Pro - Dataphysics). These calibrations show excellent agreement with [38], who previously measured surface tension and viscosity measurements of IPA-water mixtures. We vary the flow rate Q by the frequency at which the microdrops are deposited. The exact flow rate is calibrated by measuring the droplet size for each frequency, using the technique developed by [39], from typical images shown in Figure. 3.2(*b*).

3.3 Results and scaling laws

We start by considering a 1% (in volume) concentration IPA-water mixture that is deposited at a flow rate $Q = 150.7n$L/s, onto films of varying initial thickness h_0. The results are presented in Fig. 3.3(*a*), showing the spreading radius as a function of time on a log-log plot. We observe that the radius scales as $r \sim t^{1/2}$. Below we will show that this scaling law is very robust and observed for all experiments.

Quite unexpectedly, the data in Fig. 3.3(a) reveal that the radius $r(t)$ is completely independent of the initial thickness of the water layer. This is in marked contrast with the classical view on spreading due to localized deposition of surfactants [17, 33–35, 40], for which scaling laws are usually built upon the initial thickness h_0. However, we were able to observe an influence of h_0 on the dynamics *ahead* of the rim. Figure 3.4 shows two snapshots under identical conditions, both taken at $t = 15\,ms$, but with a different thickness. One very clearly observes the inside of the front (denoted as inner rim), which we have used before to measure $r(t)$. The horizontal yellow lines show that this inner rim has the same radius in both Fig. 3.4(a) and (b), confirming their dynamics to be independent of h_0. However, the width of the rim is clearly different in both cases: the outer rim has evolved over a larger distance on the image on the left (larger thickness) than on the right (smaller thickness). The position of the outer rim is much more difficult to resolve here, but for completeness we have reported the dynamics of the outer radius r_{out}(t) in Fig. 3.3(b). The front advances more rapidly on thicker water layer. Given the difficulty to accurately determine the outer front, we will from now on focus on the dynamics of the inner radius. The central goal is to find out what determines its dynamics, if we cannot use h_0 as a characteristic length scale.

Next we consider the influence of the flux Q on the inner rim dynamics, $r(t)$, while keeping the IPA concentration constant at 1%. The variation in the flux Q spans nearly three orders of magnitude from 1.5nL/s to 904.4nL/s. The initial thickness in these experiments is kept constant at $h_0 = 14\mu$m. In Fig. 3.5(a), we show the radius as a function of time for different Q. This result confirms that the spreading law $r \sim t^{1/2}$ is very robust, for all rates at which IPA is supplied. However, we do observe a clear influence of Q on the dynamics: increasing the flow rates leads to a faster Marangoni flow. To quantify this result, we fitted the curves in Fig. 3.5(a) by

$$r = A\, t^{1/2}, \tag{3.1}$$

and determined the prefactor A as a function of Q. As shown in Fig. 3.5(b), the data are consistent with a power-law, $A \sim Q^n$. Fitting the value of the exponent, we obtain $n = 0.23 \pm 0.02$. Below we argue that this corresponds to a scaling exponent $n = 1/4$, which is shown as the solid black line.

We now provide a scaling law to explain these observations. Contrarily to the situation encountered for surfactants [40], the scaling laws for the inside of the hole should not involve the thickness of the initial layer h_0. We start by considering the driving force generated by a Marangoni stress,

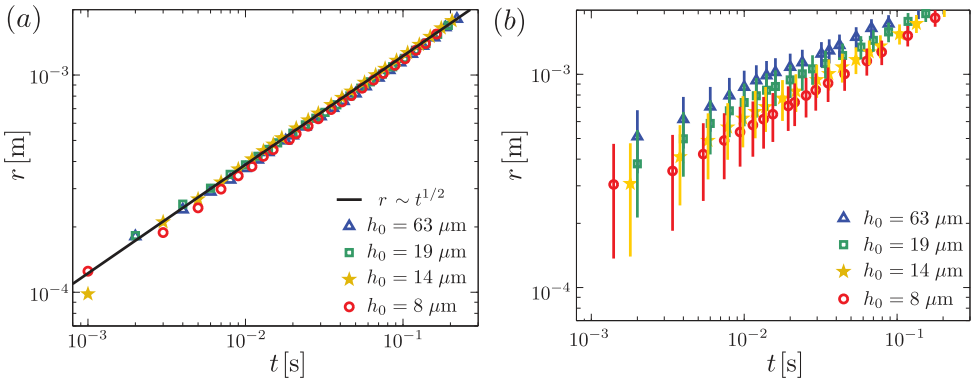

Figure 3.3: (*a*) Spreading radius $r(t)$ as a function of time for different thickesses of the water layer film h_0. The symbols ($\triangle$), ($\square$), ($\star$) and ($\bigcirc$) respectively correspond to initial water layer thickness $h_0 = 63\mu$m, $h_0 = 19\mu$m, $h_0 = 14\mu$m and $h_0 = 8\mu$m), respectively. The liquid flow to the surface is $Q = 150.7n$L/s and the isopropanol concentration is 1% which leads to a surface tension difference $\Delta\gamma = 5.56m$N/m. The initial time is taken at the instant of contact observed in the recordings. The dynamics of the spreading radius is found to be independent of the initial water layer thickness h_0. Each curve is the average of three experiments under the same conditions. (*b*) Radius of the "outer rim" $r_{\text{out}}(t)$, as defined in Fig. 3.4. Despite limited accuracy, one observes that the outer front develops more rapidly over water layers of larger thickness.

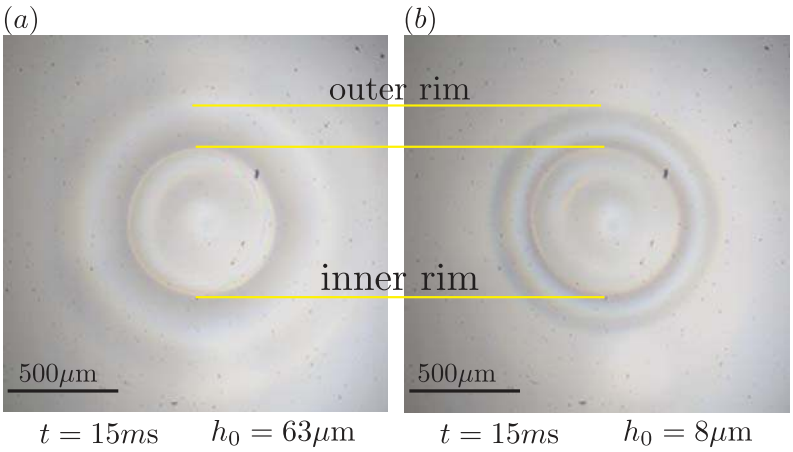

Figure 3.4: Comparing two experiments of different initial thickness: $h_0 = 63\mu$m (a) and $h_0 = 8\mu$m (b). The dynamics of the "inner rim" (lower yellow lines) is identical in both cases. By contrast, the "outer rim" (upper yellow line) advances more rapidly for larger h_0.

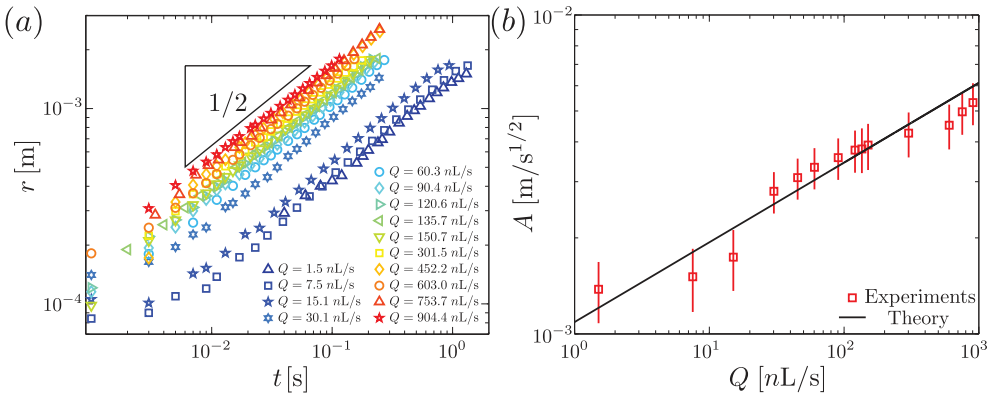

Figure 3.5: (a) Measurement of the spreading radius as a function of time for different rates of IPA-water supply ($Q = 1.5n$L/s to $904n$L/s). The spreading dynamics follows $r(t) = At^{1/2}$, where the prefactor A increases with Q. (b) The fitted values of A as a function of the flow rate Q. The solid line correponds to the predicted scaling law $A \sim Q^{1/4}$, with a prefactor 0.7 (best fit). The initial thickness in these experiments is $h_0 = 14\mu$m.

$$\tau_M = \frac{d\gamma}{dr} \sim \frac{\Delta\gamma}{r}, \tag{3.2}$$

where $\Delta\gamma$ is the surface tension difference between the two liquids. By scaling the r-derivative as $1/r$, we assume that the surface tension difference spreads out over the entire radius of the inner circle (see also [23]). Clearly, these type of arguments do not capture detailed spatial structure of the IPA-concentration profile, nor the dependence shown in Fig. 3.2(a) – yet they enable to capture the essential physics of the Marangoni-flow, as will become apparent below.

The Maragoni-stress τ_M is opposed by a viscous stress τ_η, which for thin film flows reads

$$\tau_\eta = \eta \frac{dv_r}{dz} \sim \eta \frac{\dot{r}}{h}. \tag{3.3}$$

where η is the viscosity, $\dot{r} = dr/dt$ is the velocity of the inside of the rim and, h is the characteristic thickness of the film. Balancing $\tau_M \sim \tau_\eta$ we find

$$\frac{\Delta\gamma}{r} \sim \eta \frac{\dot{r}}{h}. \tag{3.4}$$

Crucially, we have seen that the initial thickness of the film h_0 is irrelevant for the dynamics. Hence, we assume that the characteristic thickness h appearing in (3.4) corresponds to the thin film at the interior of the circle, the thickness of which is an unknown dynamical variable as well. Its value can be identified using mass conservation: we consider that the flux of incoming drops Q equals the flux displaced by the movement of the rim. The latter scales like the velocity $\dot{r}$ multiplied by the area associated to the perimeter times liquid thickness, $2\pi rh$, which in terms of scaling gives

$$Q \sim rh\dot{r}. \tag{3.5}$$

Combined with Eq. (3.4), we can eliminate h and obtain,

$$Q \sim \frac{\eta}{\Delta\gamma} r^2 \dot{r}^2, \tag{3.6}$$

or equivalently,

$$r \sim \left(\frac{Q\,\Delta\gamma}{\eta}\right)^{1/4} t^{1/2}, \quad \Longrightarrow \quad A = k\left(\frac{Q\,\Delta\gamma}{\eta}\right)^{1/4}. \tag{3.7}$$

Here we introduced k as a numerical prefactor that we expect to be of order unity.

These scaling arguments indeed explain the two key experimental observations: $r \sim t^{1/2}$ and $A \sim Q^{1/4}$. In addition, Eq. (3.7) gives a prediction for A in terms of the known parameters $\Delta\gamma = 5.56m\text{N/m}$, and $\eta = 0.95m\text{Pa}\cdot\text{s}$. We use the dataset in Fig. 3.3(b) to determine the numerical prefactor k. The black solid line (best fit) indeed corresponds to a value of order unity, namely $k = 0.7$.

To further test the validity of the scaling theory, we perform a set of experiments changing the isopropanol concentration in the IPA-water mixture from 0.05% to 23%. This changes both the surface tension and the viscosity of the IPA-water mixture, which in practice means that we have to recalibrate the settings of the microdrop for given frequency and isopropanol concentration. Therefore, by changing the IPA concentration, we vary Q, η and $\Delta\gamma$ at the same time. Yet, all values have been calibrated independently, allowing for a quantitative comparison to the theory. In Fig. 3.6(a) we present the results for the different IPA-water mixtures, corresponding to a large range of surface tension differences, from $\Delta\gamma = 0.3m\text{N/m}$ to $40m\text{N/m}$. Once more, we find $r \sim t^{1/2}$ and we can directly test the prediction for A. To this end, we try to collapse the data by plotting $(r/\tilde{A})^2$, where $\tilde{A} = (Q\,\Delta\gamma/\eta)^{1/4}$ should account for the parametric dependence. Indeed, the data nicely collapse as shown in Fig. 3.6(b), without adjustable parameter. The solid line corresponds to the theory with $k = 0.7$, as obtained from our previous fit. We conclude that the scaling theory very well describes our experimental observations.

Finally, one can solve the thickness of the thin film h, by combining Eq. (3.4) and (3.7). The various scaling laws are such that the thickness is independent of time,

$$h \sim \left(\frac{\eta\, Q}{\Delta\gamma}\right)^{1/2}, \tag{3.8}$$

and which is expressed in terms of known quantities. For the experiment in Fig 3.1($c-f$), these are $\Delta\gamma = 5.56\ m\text{N/m}$, $Q = 150.7n\text{L/s}$ and $\eta = 0.95m\text{Pa·s}$, such that $h \sim 5.1\mu\text{m}$. This estimate gives the characteristic thickness of the region at the interior of the circular region. Owing to the fringes observed just behind the moving front [see e.g. Fig. 3.1(f)], we can locally determine the film thickness using the interferometry technique developed by [37]. Indeed, we obtain a thickness that during the course of the experiment is approximately constant, within a range of $\pm 250n\text{m}$, and that is determined $h \sim 1.4\mu\text{m}$. It is a bit smaller than the prediction by the scaling law (3.8), though still of comparable magnitude. In addition, we note that the central region has

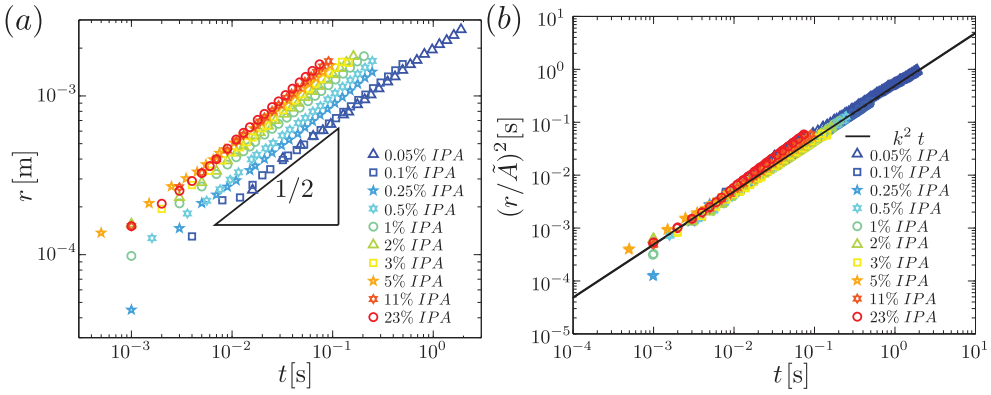

Figure 3.6: (*a*) Measurement of the spreading radius r as a function of time for different experiments using different isopropanol concentrations. The initial time is taken at the instant of contact observed in the recordings. The isopropanol concentrations were varied from 0.05% to 23% which lead to surface tension differences from $\Delta\gamma = 0.3m$N/m to $40.61m$N/m. (*b*) Collapsed curve for the various isopropanol concentrations. The curves were normalized using $A = (Q\Delta\gamma/\eta)^{1/4}$. The initial thickness in these experiments is $h_0 = 14\mu$m.

a larger thickness, as the fringes are no longer visible.

3.4 Discussion and conclusions

In this Chapter we analyzed Marangoni spreading due to the injection of an IPA-water mixture on a water film. Using a microdrop generator, we were able to supply the IPA in a very localized area and at controlled flow rates, allowing for a detailed quantitative study of the spreading. The experimentally observed dynamics was explained through a balance between Marangoni and viscous stresses, and we proposed scaling laws that were verified in detail by a data-collapse.

A key ingredient of the dynamics is that the surface tension gradient is spread out over the entire radius of the opening hole, *i.e.* $d\gamma/dr \sim \Delta\gamma/r$. This reduces the Marangoni driving force as the radius grows, which is why the spreading velocity decreases during the course of the experiment. This slowing down is markedly different from the "delayed coalescence", observed when two sessile drops of miscible liquids come into contact [6–10]. Rather than coalescing, the drop of the larger surface tension was found to pull the other drop at constant velocity over the substrate. Such a

constant velocity suggests that the surface tension gradient remains constant and localized where the two fluids meet, at least during the initial stages of the experiment [9].

The decrease in gradient observed in the present Chapter is much more reminiscent of the surfactant spreading [21, 22, 25], though some remarkable differences do appear. In particular, we have found that the initial thickness of the film does not affect the dynamics of the central zone. Most closely resembling the present work is the case where surfactants are continuously supplied in a way that their total mass increases linearly in time. However, it is usually assumed that the liquid volume is unchanged, *i.e.* the surfactant is supplied by a flow rate in units of area per time [40]. In our experiment the IPA is provided in a volumetric rate hence increasing the volume of liquid in the film – as expressed in Eq. (3.5). This subtle difference gives a different input in the scaling laws, and explains why for the present case the influence of the initial thickness drops out of the analysis. It emphasizes the key importance of the flow geometry on Marangoni flows. Finally, we remark that the dynamics ahead of the opening hole *is* affected by the initial film thickness. Such differences between upstream and downstream dynamics are generic for surfactant spreading, though intriguingly, the difference was not predicted for the case of continuous supply of surfactant (area per unit time) [40].

A priori it is not obvious to what extent the IPA-water drops can be considered as a surfactant. For this, one would need to know the detailed spatial distribution of the IPA concentration in water, both in the radial direction and across the depth of the liquid film. It is clear that the influence of diffusion needs to be considered for this. The duration of a typical experiment is about 0.1s and the diffusion constant for IPA in water is $D \sim 10^{-9}\mathrm{m}^2/\mathrm{s}$, which leads to a diffusion length of $L = 10\mu\mathrm{m}$. This length is indeed totally negligible with respect to the radial scale, but only a bit larger than the characteristic thickness of the film. Hence, a lubrication approach for which the IPA is assumed to average quickly over the depth is not perfectly justified, but also the IPA does not remain perfectly at the interface. Similar to recent work on surfactants [43], it would be interesting to further explore experimental possibilities to obtain more detailed information on the IPA distribution and the implications for the resulting Marangoni flow. We emphasize, however, that the results obtained here by experiment and scaling analysis capture the essential physical mechanisms.

Appendix: Calibrations

We use the following cleaning procedure to give hydrophilic properties to a silica glass slide ($71m\text{m}\times 71m\text{m}$). A precleaned glass slide is rinsed with pure water (resistivity $\mathscr{R} = 18.2M\Omega$), wiped with an aqueous solution of a soap (1%aq Hellmanex III), rinsed with pure water, then with isopropanol and dried with nitrogen. Afterwards, the substrate is placed inside a plasma cleaner (Harrick Plasma PDC-002) for 3 minutes at $1.8m$bar. The hydrophilicity of this process is tested measuring the contact angle of a sessile drop of water.

To create the uniform water layer on the film, we fix the substrate on a spin coater with a vacuum pump. This is shown in Fig. 3.1(a). Then, we continuously supply water to the substrate while spinning during 10s. Afterwards, the water supply stops and the rotation continue during 10s more. The resulting thickness is measured as a function of the spin rate (from 200rpm to 600rpm). The thickness is measured using a High-Resolution spectrometer (Ocean optics HR4000), similar to [44] and [45].

We use a microdrop dispenser system (Microdrop Technologies MD-E-3000) to deposit a continuous supply of an IPA-water mixture on top of the water layer. The microdrop dispenser produces a continuous train of drops at frequencies varying from 1Hz to 6000Hz. For each IPA-water mixture we calibrate the settings of the microdrop. This calibration consists of finding microdrop settings that produce a monodisperse train of drops and measure the typical drop diameter, using the technique presented by van der Bos *et al.* [39], see Fig. 3.2(b). This measurement is performed synchronizing a camera with the piezo pulse and a laser. The camera takes a picture at each cycle with a successive controlled delay. Different pictures at different moments of time allow to reconstruct the evolution of the stream of drops leaving the microdrop nozzle. The series of pictures are used to measure the drop diameter. The exact flow rate is calibrated by measuring the droplet size for each frequency. In order to achieve mono disperse size drops we do trial and error tests under different conditions.

References

[1] A.E. Hosoi and J.W.M. Bush. Evaporative instabilities in climbing films, *J. Fluid Mech.*, **442**, 217:239, 2001.

[2] A.F.M. Leenaars and J.A.M. Huethorst and J.J. Van Oekel. Marangoni drying: A new extremely clean drying process, *Langmuir*, **6** (11), 1701:1703, 1990.

[3] J. Marra and J.A.M. Huethorst. Physical principles of Marangoni drying, *Langmuir*, **7** (11), 2748:2755, 1991.

[4] O.K. Matar and R.V. Craster Models for Marangoni drying, *Phys. Fluids*, **13** (7), 1869:1883, 2001.

[5] S.B.G.M. O'Brien. On Marangoni drying: nonlinear kinematic waves in a thin film, *J. Fluid Mech.*, **254**, 649:670, 1993.

[6] H. Riegler and P. Lazar. Delayed Coalescence Behavior of Droplets with Completely Miscible Liquids, *Langmuir*, **24** (13), 6395:6398, 2008.

[7] S. Karpitschka and H. Riegler. Quantitative Experimental Study on the Transition between Fast and Delayed Coalescence of Sessile Droplets with Different but Completely Miscible Liquids, *Langmuir*, **26** (14), 11823:11829, 2010.

[8] R. Borcia and M. Bestehorn. Partial Coalescence of Sessile Drops with Different Miscible Liquids, *Langmuir*, **29** (14), 4426:4429, 2013.

[9] S. Karpitschka and H. Riegler. Noncoalescence of Sessile Drops from Different but Miscible Liquids: Hydrodynamic Analysis of the Twin Drop Contour as a Self-Stabilizing Traveling Wave, *Phys. Rev. Lett.*, **109** (6), 066103, 2012.

[10] S. Karpitschka and H. Riegler. Sharp transition between coalescence and noncoalescence of sessile drops, *J. Fluid Mech.*, **743**, 2014.

[11] W.D. Ristenpart and P.M. McCalla and R.V. Roy and H.A. Stone. Coalescence of Spreading Droplets on a Wettable Substrate, *Phys. Rev. Lett.*, **97** (6), 064501, 2006.

[12] R.D. Narhe, D.A. Beysens and Y. Pomeau. Dynamic drying in the early-stage coalescence of droplets sitting on a plate, *Euro. Phys. Lett.*, **81** (4), 46002, 2008.

[13] M.W. Lee, D.K. Kang, S.S. Yoon and A.L. Yarin. Coalescence of Two Drops on Partially Wettable Substrates *Langmuir*, **81** (8), 3791:3798, 2012.

[14] Hernández-Sánchez, J. F. and Lubbers, L. A. and Eddi, A. and Snoeijer, J. H. Symmetric and Asymmetric Coalescence of Drops on a Substrate *Phys. Rev. Lett.*, **109** (18), 184502, 2012.

[15] M.S. Borgas and J.B. Grotberg. Monolayer flow on a thin film *J. Fluid Mech.*, **193**, 151:170, 1988.

[16] D.P. Gaver and J.B. Grotberg. The dynamics of a localized surfactant on a thin film, *J. Fluid Mech.*, **213**, 127:148, 1990.

[17] O.E. Jensen. Self-similar, surfactant-driven flows, *Phys. Fluids*, **6**(3), 1084: 1094, 1994.

[18] O.K. Matar and S.M. Troian. Spreading of a surfactant monolayer on a thin liquid film: Onset and evolution of digitated structures, *Chaos*, **9** (1), 141:153, 1999.

[19] M.R.E. Warner, R.V. Craster and O.K. Matar. Fingering phenomena associated with insoluble surfactant spreading on thin liquid films, *J. Fluid Mech.*, **510**, 169:200, 2004.

[20] M.R.E. Warner and R.V. Craster and O.K. Matar. Fingering phenomena created by a soluble surfactant deposition on a thin liquid film, *Phys. Fluids*, **16**(13), 2933:2951, 2004.

[21] D.W. Fallest, A.M. Lichtenberger, C.J. Fox and K.E. Daniels. Fluorescent visualization of a spreading surfactant *New J. Phys.*, **12**(7), 073029, 2010.

[22] E.R. Peterson and M. Shearer. Radial Spreading of a Surfactant on a Thin Liquid Film, *AMRX*, **2011**(1), 1:22, 2011.

[23] M. Roché, Z. Li, I.M. Griffiths, S. Le Roux, I. Cantat, A. Saint-Jalmes and H.A. Stone. Marangoni Flow of Soluble Amphiphiles *Phys. Rev. Lett.*, **112** (20), 208302, 2014.

[24] J.B. Grotberg and D.P. Gaver III. A Synopsis of Surfactant Spreading Research *J. Colloid Interf. Sci.*, **178** (1), 377:378, 1996.

[25] A. Hamraoui, M. Cachile, C. Poulard and A.M. Cazabat,. Fingering phenomena during spreading of surfactant solutions, *Colloid. Surface. A*, **250**(1), 215:221, 2004.

[26] J. Ahmad and R.S. Hansen. A simple quantitative treatment of the spreading of monolayers on thin liquid films, *J. Colloid Interf. Sci.*, **38**,(3) 601:604, 1972.

[27] S.M. Troian, E. Herbolzheimer and S.A. Safran. Model for the fingering instability of spreading surfactant drops, *Phys. Rev. Lett.*, **65**,(3) 333, 1990.

[28] O.E. Jensen and J.B. Grotberg. The spreading of heat or soluble surfactant along a thin liquid film, *Phys. Fluids A-Fluid*, **5**,(1) 58:68, 1993.

[29] M.R.E. Warner and R.V. Craster and O.K. Matar. Linear stability analysis of an insoluble surfactant monolayer spreading on a thin liquid film, *Phys. Fluids*, **9**, 3645:3657, 1997.

[30] M. Cachile, A.M. Cazabat, S. Bardon, M.P. Valignat and F. Vandenbrouck. Spontaneous spreading of surfactant solutions on hydrophilic surfaces, *Colloid. Surface. A*, **159**(1), 47:56, 1999.

[31] A.D. Dussaud, O.K. Matar and S.M. Troian. Spreading characteristics of an insoluble surfactant film on a thin liquid layer: comparison between theory and experiment, *J. Fluid Mech.*, **544**, 23:51, 2005.

[32] O.K. Matar and R.V. Craster. Dynamics of surfactant-assisted spreading, *Soft Matter*, **5**(20), 3801:3809, 2009.

[33] D.K. Sinz, M. Hanyak and A.A. Darhuber. Immiscible surfactant droplets on thin liquid films: Spreading dynamics, subphase expulsion and oscillatory instabilities, *J. Colloid Interf. Sci.*, **364**,(2) 519:529, 2011.

[34] D,K. Sinz, M. Hanyak, J.C. Zeegers and A.A. Darhuber. Insoluble surfactant spreading along thin liquid films confined by chemical surface patterns, *Phys. Chem. Chem. Phys.*, **13**,(20) 9768:9777, 2011.

[35] M. Hanyak, D.K. Sinz and A.A. Darhuber. Soluble surfactant spreading on spatially confined thin liquid films, *Soft Matter*, **8**,(29) 7660:7671, 2012.

[36] F. Brochard-Wyart and P.G. de Gennes Dynamics of partial wetting *Adv. Colloid Interfac.*, **39**(0), 1:11, 1992.

[37] R.C.A. van der Veen, T. Tran, D. Lohse and C. Sun. Direct measurements of air layer profiles under impacting droplets using high-speed color interferometry, *Phys. Rev. E*, **85**(2), 026315, 2012.

[38] T.T. Ngo, T.L. Yu and H. Lin Influence of the composition of isopropyl alcohol/water mixture solvents in catalyst ink solutions on proton exchange membrane fuel cell performance, *Chaos*, **225** (0), 293:303, 2013.

[39] A. van der Bos, A. Zijlstra and E. Gelderblom and M. Versluis. iLIF: illumination by Laser-Induced Fluorescence for single flash imaging on a nanoseconds timescale *Exp. Fluids*, **51**(5), 1283:1289, 2011.

[40] O.E. Jensen and J.B. Grotberg. Insoluble surfactant spreading on a thin viscous film: shock evolution and film rupture *J. Fluid Mech.*, **240**, 259:289, 1992.

[41] R. Borcia, S. Menzel and M. Bestehorn and S. Karpitschka and H. Riegler. Delayed coalescence of droplets with miscible liquids: Lubrication and phase field theories *Eur. Phys. J. E.*, **34** (3), 1:9, 2011.

[42] O.E. Jensen. The spreading of insoluble surfactant at the free surface of a deep fluid layer, *J. Fluid Mech.*, **293**, 349:378, 1995.

[43] E.R. Swanson, S.L. Strickland, M. Shearer and K.E. Daniels. Surfactant Spreading on a Thin Liquid Film: Reconciling Models and Experiments, *arXiv preprint arXiv:1306.4881*, 2013.

[44] J.H. Snoeijer and J. Ziegler, B. Andreotti, M. Fermigier and J. Eggers. Thick Films of Viscous Fluid Coating a Plate Withdrawn from a Liquid Reservoir, *Phys. Rev. Lett.*, **100**(24), 244502, 2008.

[45] J. Seiwert and C. Clanet and D. Quéré. Coating of a textured solid, *J. Fluid Mech.*, **2011**(669), 55:63, 2011.

4

The dewetting rim: Dynamic contact angles and external forcing

* *A liquid layer on top of a hydrophobic surface gets unstable if at some point its thickness becomes smaller than a certain critical (microscopic) length: a dewetting hole will grow around that point, the liquid of the film being collected into a rim around the hole. The physics of the dewetting rim has been explained before: Two theories give dewetting velocities and dynamic contact angles as a function of layer thickness and static contact angles. On the one hand de Gennes et al. [1] proposed that the ratio of dynamic and static contact angles has a constant value of* $\theta_d/\theta_r \sim 0.25$*, independent of the capillary number. On the other hand Snoeijer & Eggers [16] proposed a relationship based on matched asymptotics of the lubrication equation, where* θ_d/θ_r *is significantly larger and a function of the capillary number. In this chapter we present measurements of the dynamic contact angles for various liquid/substrate combinations (*i.e. *different static angles, viscosities and surface tensions), and compare the results with these two models. Furthermore, we use different approaches to enhance the velocity of the dewetting rim. These are substrate spinning, a radial gas flux across the hole/film, and Marangoni forces.*

*To be submitted as: J.F. Hernández Sánchez, S. Karpitschka and J.H. Snoeijer, Dynamic contact angle measurement of the dewetting rim.

4.1 Introduction

Dewetting, as defined by de Gennes, is the spontaneous withdrawal of a liquid film from a hostile surface [1]. This phenomena is ubiquitous, *e.g.*, since our skin is hydrophobic, dewetting can be seen just after we close the shower faucet, or when cleaning a teflon pan with water. In both examples holes nucleate and grow as they try to remove water from the surface. Fundamental questions on the dynamics of wetting under partially wetting conditions have been studied in a broad variety of contexts, for reviews see [2, 3]. This is also of great importance in surface engineering, as it is in reducing the drag of maritime ships [4, 5], improving the resistance to corrosion [6], or for the use of hydrophobic materials for aircraft wings in order to avoid the formation of a water film from atmospheric moisture that freezes later on at high altitudes [7]. Another important example is found in the semiconductor industry, in the processing of silicon wafers. Different microfabrication processes give non-homogeneous wetting properties to the wafer surfaces. This is important during wet chemical processes, because partial drying leads to the formation of drying stains, which may cause faults in the microelectronic devices. In this context, the method of Marangoni-drying makes use of selective evaporation/condensation of liquids/vapors with different surface tensions during the dewetting/drying phase [22]. At the same time the wafer is spinning in order to induce an outward flow. It is a challenge to better understand the interplay between spontaneous dewetting, driven by the surface energies, and external forces from centrifugal acceleration, or Marangoni forces.

The dewetting of a liquid film of uniform thickness has been studied exensively in the past [1, 14–16, 19, 28]. Once a small dry patch is nucleated on a partially wetting substrate, the free energy of the system is reduced by increasing the surface area of the dry substrate. This provides a natural driving force for the receding contact line motion. As a result, a circular region of dry surface grows over time. A sketch of the two-dimensional cross section of the resulting liquid profile is given in Fig. 4.1. The radius of the dewetting hole $r(t)$ increases over time [1]. The volume of liquid that was originally on this dry patch is collected into the outward moving rim. The rim thus grows over time in both, height (denoted by h_r), and width ($2w$). The apparent or dynamic contact angle is given by θ_d. Many aspects of the dynamics have been investigated. For example, the role of intermolecular forces, manifested in the loss of stability of ultra thin films, was studied in [8–10]. The influence of slip [11] or non-Newtonian effects [12, 13] on the dewetting rim was also investigated.

Interestingly, even in the case of a macroscopic film of Newtonian liquid, there remain some important unresolved questions. It is well-established that the contact

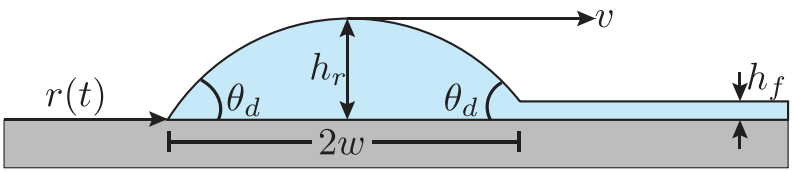

Figure 4.1: Cross-section of a circular dewetting front, connected to a liquid film of thickness h_f. The radius of the dewetting hole, $r(t)$, grows over time. The dewetted liquid volume is collected into a liquid rim (the dewetting rim) of height h_r and width $2w$. The underlying hydrodynamics results in the dynamic contact angles θ_d of the receding (left) and the advancing (right) fronts.

line velocity is dominated by the liquid viscosity η, surface tension γ, and the static (receding) contact angle θ_r, as [3, 14]

$$\mathrm{Ca} \sim \theta_r^3, \tag{4.1}$$

where the capillary number is defined as

$$\mathrm{Ca} = \frac{\eta V}{\gamma}. \tag{4.2}$$

However, different theoretical predictions exist for the proportionality factor in (4.1). Even more pronounced is the difference in the predictions for the dynamic contact angle θ_d as a function of the static receding contact angle θ_r: the estimation given by de Gennes *et al.* [1] is that $\theta_d/\theta_r \approx 0.25$, while a lubrication analysis suggests a substantially larger ratio that weakly depends on the experimental parameters [16].

In this Chapter we will first elaborate on the open question regarding the dynamic contact angle of unforced dewetting (Sec. 4.2), followed by a detailed description of the experimental methods (Sec. 4.3). Then we present experimental results for the dewetting speed and dynamic contact angles for a variety of liquids and substrates (Sec. 4.4). Finally, we study the impact of external forcings on the dewetting motion. In sec. 4.5 we demonstrate the effect of centrifugal forces due to spinning, and we report two instabilities that were observed. In Sec. 4.6, we also discuss the influence of an external air-flow over the dewetting hole/film, and Marangoni forces due to the vapor of a second liquid in the air flow.

4.2 Dynamic contact angle of the dewetting rim

Let us briefly recall the mechanism by which the velocity of the dewetting rim is selected, following the analysis of [1]. The idea is that liquid at the rim is essentially at equilibrium, *i.e.* constant pressure, such that the cross-sectional geometry of the rim can be approximated as a circle. The energy that is harvested by opening the dry hole is dissipated mainly at the receding and advancing fronts of the rim. This is captured by a dynamical contact angle θ_d, that from the circular geometry of the rim must be the same on both sides. To close the problem, a relation between the θ_d and the capillary number Ca is required. The receding contact line is directly in contact with the dry substrate, and the motion will thus be related to the difference with the static receding angle θ_r. The front of the rim is advancing over the liquid film, and can be seen as an advancing contact line over a completely wetting surface. Expressing this in terms of the model by de Gennes [17], we obtain the following relations:

$$\begin{aligned} \theta_d^3 &= 6\mathrm{Ca}L_a, \qquad \text{(advancing)} \\ \theta_d\left(\theta_r^2-\theta_d^2\right) &= 6\mathrm{Ca}L_r. \qquad \text{(receding)} \end{aligned} \tag{4.3}$$

The prefactors $L_{a,r}$ appearing in the advancing/receding cases are numerical constants that represent the viscous singularity of contact line motion. For the motion over the macroscopic film this was estimated $L_a \sim 1$, while the receding contact line one typically finds $L_r \sim 10$. Eliminating Ca from (4.3) readily gives the scaling law (4.1), while for the dynamic angle one obtains

$$\theta_d = \frac{\theta_r}{\left(1+\frac{L_r}{L_a}\right)^{1/2}} \sim \frac{\theta_r}{4}, \tag{4.4}$$

where the last estimation is taken from de Gennes *et al.* [1].

An alternative approach to this problem is to analyze the problem directly from the one-dimensional lubrication equation [16, 19]. The results from a matched asymptotic expansion can be summarized by a different relation for the dynamic contact angles [16]

$$\begin{aligned} \theta_d^3 &= 9\,\mathrm{Ca}\,\ln\frac{2a\mathrm{Ca}^{1/3}w}{e\,h_f}, \qquad \text{(advancing)} \\ \theta_d^3 &= \theta_r^3 - 9\,\mathrm{Ca}\,\ln\frac{2\theta_r w}{3\lambda}. \qquad \text{(receding)} \end{aligned} \tag{4.5}$$

This result is of the classical form by Tanner, Cox and Voinov [2], but here has explicit expressions in terms of the slip lenght λ, the film thickness h_f and the width of the rim w. The expression also involves Euler's number e and a numerical constant $a = 1.094\cdots$ originating from the matching to the film. Eliminating Ca gives

$$\mathrm{Ca} = \frac{\theta_r^3}{9}\left[\ln\left(\frac{4}{3e}\theta_r\mathrm{Ca}^{1/3}\frac{w^2}{\lambda h_f}\right)\right], \tag{4.6}$$

which is once more of the form (4.1). The dynamic contact angle becomes

$$\frac{\theta_d}{\theta_r} = \left(1 + \frac{\ln\dfrac{2\theta_r w}{3\lambda}}{\ln\dfrac{2ea\mathrm{Ca}^{1/3}w}{h_f}}\right)^{-1/3}, \tag{4.7}$$

exhibiting a different exponent than (4.4) for the denominator on the right.

Equations 4.4 and 4.7 give different predictions for the contact angle of the rim. To illustrate the mechanism of the contact angle selection, let us compare the dynamic contact angles given by (4.3) and (4.5), shown in Fig. 4.2*a*) and *b*) respectively. The plots show the predicted advancing contact angle (in blue) and the receding contact angle (in red) for both models. The crossing of the two lines selects the dynamic contact angle and the associated value of the capillary number. For the lubrication model, the ratio θ_d/θ_r is significantly larger than the prediction of 0.25. Note also that the angle selected in de Gennes' model is on the lower branch of the receding contact line, which is supposed to correspond to an unstable solution.

4.3 Experimental methods

We now provide details on the experimental methods. In the first part we discuss the surface modification procedure, which allows to control the wetting properties. The second part describes the illumination system used to visualize and measure the

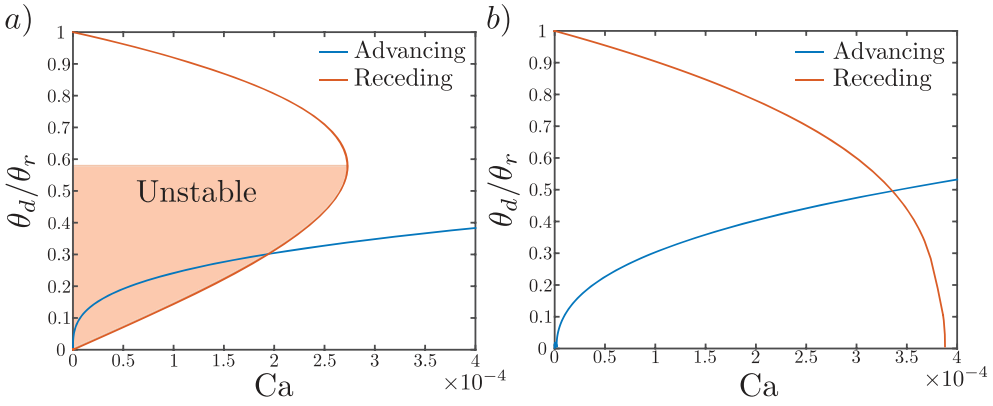

Figure 4.2: Selection of the velocity and dynamic contact angle of the dewetting rim. *a*) De Gennes theory for the dynamic contact angle (θ_d) for the receding (red) and advancing (blue) contact angles. *b*) Lubrication model for the receding (red) and the advancing (blue) contact angles, for $\theta_r = 20^o$, $w = 1m$m, $h_f = 10\mu$m and $\lambda = 10^{-9}$m.

radius of the dewetting hole as a function of time. The last part of the experimental section describes the interferometry setup used to visualize in detail the dynamic contact line, leading to measurements of the dynamic contact angle θ_d.

4.3.1 Surface modification and liquids used in the experiment

As substrates we use single-side polished silicon wafers (P type, Boron, (100) orientation, 5-10$\Omega \cdot c$m resistivity) of 100mm diameter. The polished surfaces were coated with different silanes in order to vary their wettability (static contact angle) for different liquids. The details and especially the cleanliness of this process are extremely important to achieve well defined substrates and reproducible results. Reproducible results were achieved by the following steps. First, organic contamination was removed from the silicon wafer surfaces by immersion in fresh piranha solution *i.e.*, sulfuric acid mixed with hydrogen peroxide at a ratio of 3:1 by volume, for approximately 30 minutes. Then the wafers were rinsed with ultrapure milliQ water at least five times. Then they were sonicated in fresh milliQ water in a low power ultrasonic bath for about 10 minutes at elevated temperature ($40 - 60^o$C) to remove traces of the acid. After that, the wafers were spin-dried in a clean room environment with additionally blowing dry nitrogen (purity 5.0) onto the center of the spinning wafer. Subsequently the silanes were vapor deposited onto the wafers in a contin-

uously evacuated dessiccator. During this, the wafers were placed above a drop of pure silane with the polished side facing down. The residual pressure in the dessicator was about 20$m$bar. After a few hours, the wafers removed from the vacuum and annealed in an oven at 100^{o}C for one hour. Afterwards, the excess of silane was removed by sonicating in acetone. As a last step in the surface preparation, we covered the central part of the wafer with a PDMS disk (diameter approximately 80mm), and plasma cleaned the edge of the wafer. With this last step we ensured that edges of the wafer were hydrophilic. This is critical, since otherwise any liquid film would spontaneously dewet from the wafer edges. Recovering the hydrophilicity around the periphery of the wafer, we assure that the dewetting hole can be nucleated in the center.

We used three different silanes: Vinyldimethylchlorosilane (VDMCS), n-Decyldimethylchlorosilane (DDMCS) and trichloro(1H,1H,2H,2H-perfluorooc ilane (pfDDMCS). The silanes were supplied by ABCR GmbH (purity $\geq 95\%$) and used as supplied. The resulting static contact angles with different liquids (see Table 4.1 for liquid properties) are described in Table 4.2. With the above preparation procedure, the hysteresis of the contact angle was small, typically $\pm 3^o$. However, since the results can be very sensitive to any contact angle variation, both static advancing (θ_a) and receding (θ_r) were measured by inflating and deflating drops with a needle attached to them.

Liquid	Surface tension [mN/m]	Viscosity [Pa·s]$\times 10^{-3}$
Water	72	1
Ethanol	22.1	1.2
Acetone	25.2	0.36
Isopropyl alcohol	21.7	1.96
1,2-Propanediol	45.6	40
Squalene	32	12

Table 4.1: Properties of the liquids used for the dewetting experiments.

4.3.2 Experimental procedure for dewetting experiments

The liquid films for the dewetting experiments were prepared by depositing an excess amount of the respective liquid onto the prepared wafer. Then, the film was thinned to the desired thickness by spinning the wafer for a certain time (5-30s) at a certain

Liquid	VDMCS $\theta_r[^o]$	DDMCS $\theta_r[^o]$	pfDDMCS $\theta_r[^o]$
Water	60	-	99
Ethanol	-	25	-
Acetone	-	-	55
Isopropyl alcohol	-	-	44
1,2-Propanediol	25	-	69
Squalene	-	19	61

Table 4.2: Static receding contact angle for different combinations of liquid and coating.

rotation rate (300-1500rpm).

During the spinning process we measured the evolution of the thickness with interferometry, see also Chapter 3. We use a High Resolution Spectrometer HR4000 (Ocean Optics), focused at a well-defined point ($\sim 5m\text{m}^2$). The achieved film thicknesses were well reproducible with respect to spinning rates and times. One example of these measurements (for isopropanol) is presented in Fig. 4.3. The plot shows the height of the film h_f as a function of time during spining at different rotation rates. In this particular example, we observe that due to evaporation, the evolution of the thickness of isopropanol ultimately leads to a completely dry surface. For the dewetting experiments, the spinning was stopped prior to complete drying. Dewetting Experiments were performed for a remaining liquid film thickness ranging from 5μm and 200μm.

After the preparation of the film on the substrate, the dewetting has to be nucleated. To achieve this, we use a short (0.05-0.2s) nitrogen pressure pulse, hitting the film surface in normal direction. The pulse was emitted from a flat-ended needle very close (approx. 0.5-1.5mm) to the film surface. The short duration of the pulse and the short distance to the surface guarantee a very local distortion of the liquid film. Therefore, at some distance to the center ($\lessapprox 1c$m), the film was undisturbed and we could observe the dewetting of a homogeneous flat film.

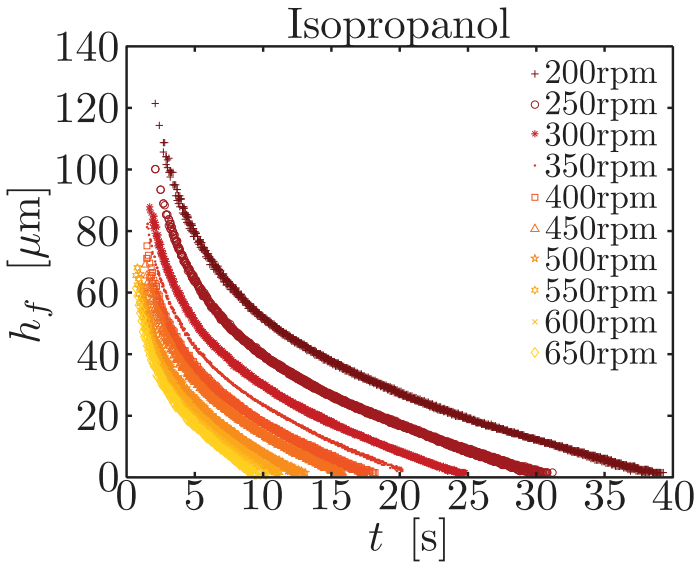

Figure 4.3: Using an interferometer, we measured the time evolution of the thickness of different liquids as a function of time during the spin coating process. In this example we show the thickness evolution of isopropanol.

4.3.3 Radius and velocity measurement of the dewetting rim

To visualize the dewetting dynamics we used the illumination as indicated in Fig. 4.4. The illumination consists of a fiber lamp whose light is limited by a diaphragm and collimated by a plano-convex lens onto a holographic diffuser (10^o diffusing angle). Then, a Fresnel lens ($30 \times 30c$m) is used to collimate the light from the diffuser with a well-defined divergence onto the reflecting wafer. By this, we enhance the contrast and clearly visualize the contact line as a transition from a bright dry wafer) to a dark region (inclined liquid surface). A beam splitter (50/50), tilted 45^o is used to visualize the top aspect of the wafer. A high-speed camera is used to record the experiments, as shown in Fig. 4.4. The elements of the illumination setup are used to make the illumination as uniform as possible. The use of a Fresnel lens is important, because the reflecting nature of the observed surfaces requires a converging beam across the rather large surface area ($10c$m diameter), *i.e.* the lense has to be bigger than the observed area. The diffusor (illuminated by the collimated fiber light source) acts as a homogeneous light source, close to but slightly behind the backfocal plane of the Fresnel lens. Typical images of these experiments are shown in Fig. 4.6, together with sketches of the side- and top aspects.

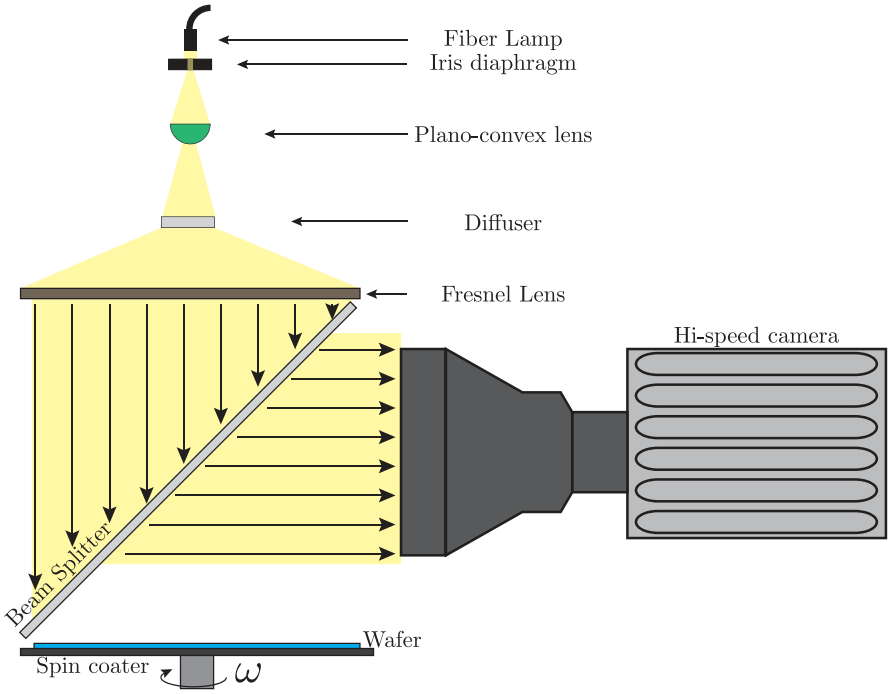

Figure 4.4: The optical setup provided a uniform, slightly convergent illumination of the wafer. It consists of a fiber lamp, a diaphragm, a plank-convex lens, a diffuser and a Fresnel lens. A beam splitter is used to record top aspects with illumination from above. The images were recorded using a hispeed camera (Photron SAX, SA1, or SA7) with a 50mm Macro lens (Carl Zeiss).

4.3.4 Interferometry technique for dynamic contact angle measurements

We finally describe the interferometry technique used to measure the dynamic contact angle in dewetting experiments. Fig. 4.5a) sketches the path of the light through the film. As light reaches the surface of a transparent film, part of it is transmitted. The transmitted light crosses through the film and is reflected at the substrate. Part of the reflected light passes through the top surface of the film and interferes with the part of the light that is directly reflected off the top surface. By using single wave length illumination, dark and bright bands appear as a result of constructive and destructive interference. The resulting intensity depends on the phase angle of the interfering beams which is determined by the physical properties of the film, like its refractive index and thickness. Also the incident angle of the light plays an important role.

Constructive interference on a flat film is given by the condition

$$2\, n_2 h_f \cos\phi = m\lambda, \tag{4.8}$$

where n_2 is the refraction index of the liquid film, h_f is the film thickness, and ϕ is the incident angle of the light. m is an integer number and λ is the wavelength of the light. We use this technique to measure the local thickness of the receding contact angle and thus reconstruct the height profile near to the contact line. It is important to mention that such a technique is limited to measure small contact angles. For contact angles larger than 30^o the fringes are indistinguishable from each other.

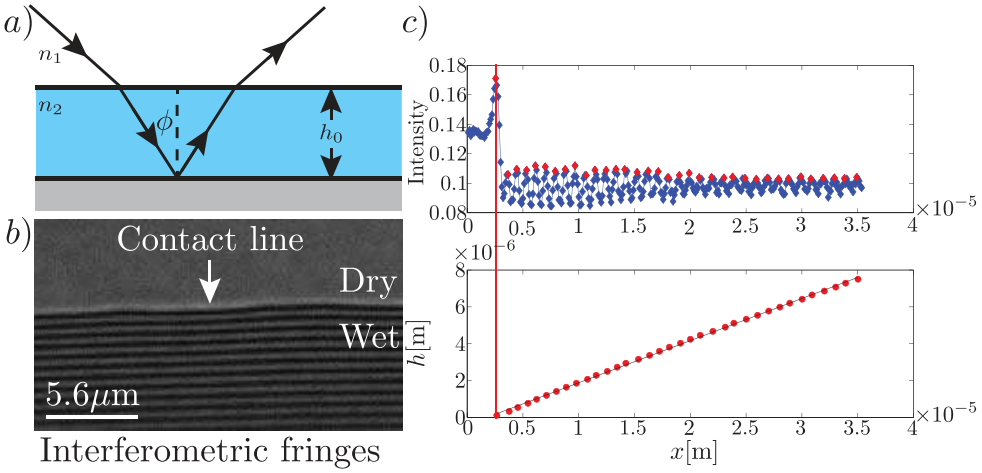

Figure 4.5: *a*) Sketch of the constructive/destructive interference pattern during the dewetting of the rim. *b*) Visualization of the interference pattern during the dewetting of squalene on top of a silicon wafer substrate coated with DDMCS. *c*) Intensity profile from the image (upper panel) and the reconstructed height profile from the bright fringes (lower panel). A parabolic fit is used to calculate the contact angle.

In order to measure the interferometry patterns close to the contact line, we used an Olympus microscope with a 100x infinity-corrected long working distance objective (Mitutoyo). The illumination of the system was provided by a red diode laser (650*n*m). The speckle of the laser was smoothened out using two holographic diffusers, one static and one rotating, which lead to images as shown in Fig. 4.5*b*). The dark and bright bands on the intensity profile are regions where there is destructive and constructive light interference on the liquid film, as can be seen in Fig. 4.5*c*). The distance between the local maxima is extracted, and, using Eq. (4.8), the height profile (shown in Fig. 4.5*c*) is reconstructed. A parabolic fit of the height profile is

used to measure the dynamic receding contact angle. The first datapoint is not included in the fit, in order to reduce the error due to the uncertainty in the threshold value between dry an the wet front. A weak curvature of the profile is observed, with a curvature that is of the order of the size of the large rim.

4.4 Dewetting velocity and dynamic contact angle

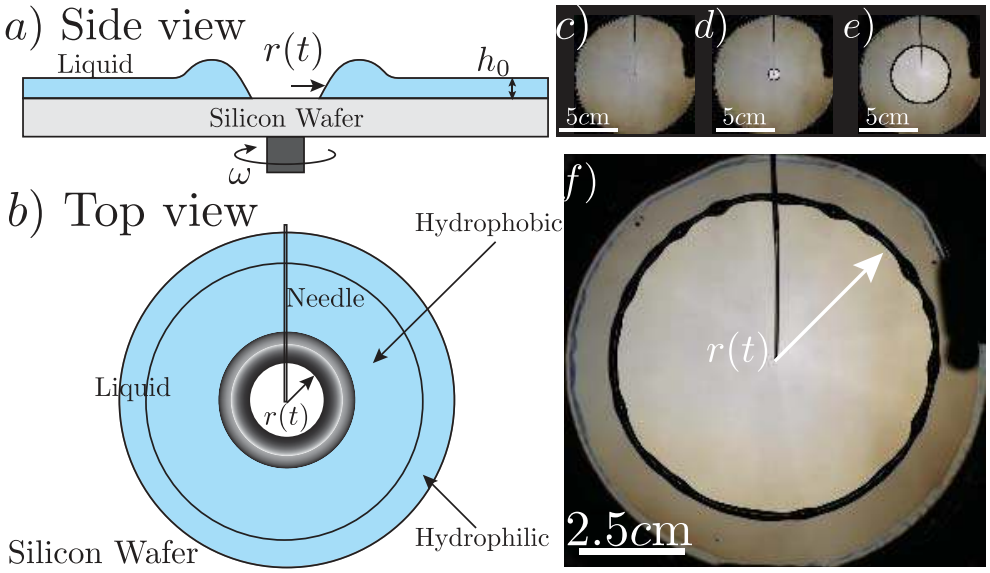

Figure 4.6: *a*) Sketch of the cross-section through the spin coater setup. A uniform film of liquid (thickness h_0) is dewetting. The dewetted liquid is collected into an axisymmtetric rim. *b*) Sketch of the top view. While the main part of the wafer surface is hydrophobic, the edges were hydrophilized to avoid dewetting from the edges. A high speed camera (here a color version) is used to record the process. A nozzle shoots a short pulse of clean nitrogen onto the film, in order to start the dewetting. *c*)$-$*f*) Top view of the typical experimental image at times $t = 0\,\mathrm{s}$, $t = 4\,\mathrm{s}$, $t = 30\,\mathrm{s}$, $t = 50\,\mathrm{s}$. The liquid in this example is 1,2-propanediol on top of a pfDDMCS coated substrate ($\theta_r = 69^o$).

Here we present the results of our dewetting experiments, in the absence of any external forces. We start by showing a typical experiment in Fig. 4.6. Panels *a*) and *b*) respectively provide a sketch of the cross-sectional and top aspect of the experiments. Panels *c*) to *f*) show experimental images. After spin coating a film of

thickness h_0, a dewetting hole is nucleated from short pulse of nitrogen flux, imposed at $t = 0$. The pulse is given from a capillary tube bended at 90^o, and the tube is visible as a line crossing the wafer. The rim is clearly visible in the experimental images of Fig. 4.6*c*)−*f*): the light is deflected due to the curved surfaces of the rim, making regions with strongly inclined liquid surfaces (close to the contact line) appear dark. The dewetting hole is almost perfectly circular, owing to the elaborate substrate preparation procedure.

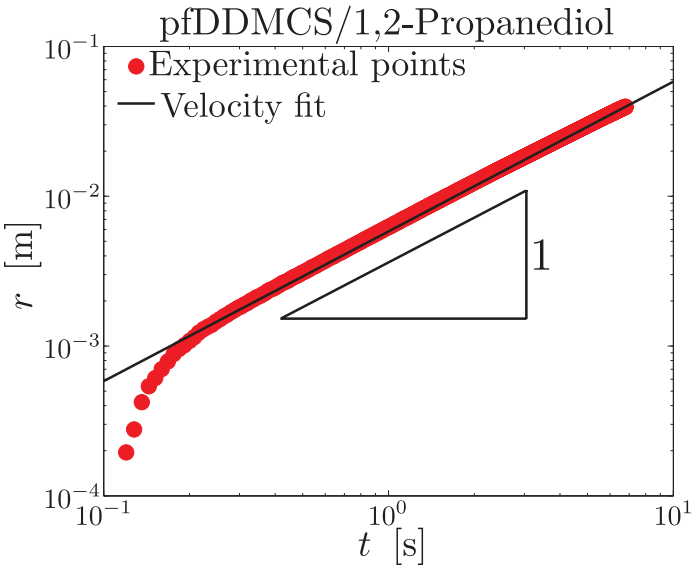

Figure 4.7: Typical measurement of the radius as a function of time $r(t)$ for a dewetting hole of 1,2-propanediol on a pfDDMCS coated substrate. The fit shows that the dewetting velocity is constant only after a short initial stage (the latter being dominated by the nucleation pulse).

For each experiment we measure the radius of the dewetting hole $r(t)$, as a function of time. Typical results are given in Fig. 4.7. In all cases, we observe that, after a small initial phase after applying the pulse, the contact line moves across the substrate at a well defined, constant velocity. In the remainder we will report the dewetting velocity as measured *after* the short transient initial stage.

The dewetting velocity is determined for a wide range of experimental parameters, *i.e.*, combinations of substrates and liquids, as is summarized in Fig. 4.8. We report the capillary number as a function of the static receding contact angle θ_r. Our results are indeed consistent with the scaling $\mathrm{Ca} \sim \theta_r^3$, and resemble those shown

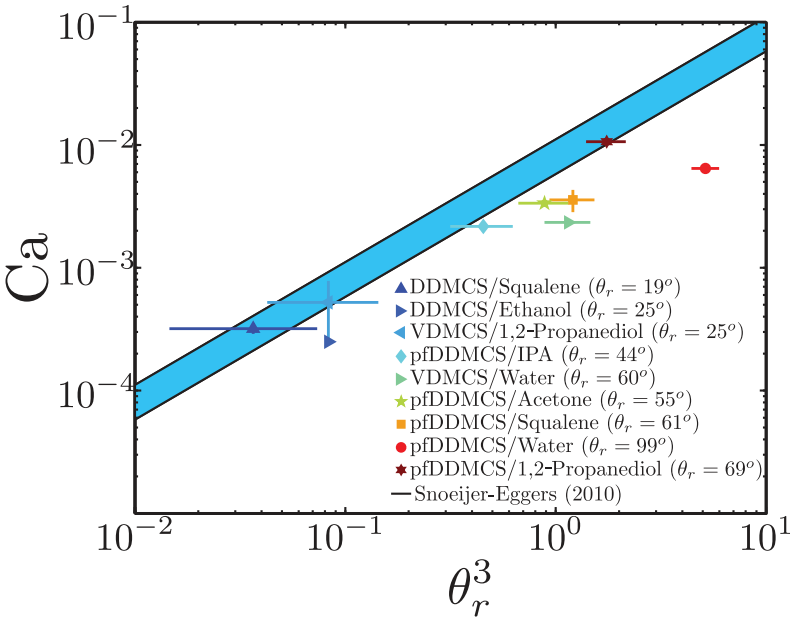

Figure 4.8: Experimental measurements of the capillary number Ca for the dewetting hole versus the receding contact angle θ_r^3, for different combinations of liquids and substrates. Contact angles vary from 19^o up to 99^o. The prediction by Snoeijer-Eggers (Eq. (4.6) [16]) is presented by the blue area, taking into account typical experimental parameters.

previously for different types of liquids and substrates [3, 14].

To quantitatively test the validity of the lubrication prediction, we considered (4.6) within the range of parameters from the experiment. The width of the rim w varies roughly from $1m$m to $1c$m, depending on initial film thickness and dewetted radius. The variation in the film height h_f ranges from 1μm to 300μm. The value of the slip length was estimated as $\lambda = 10^{-9}$m. This leads to a small variation of the numerical factors in (4.6), which is represented by the blue region in Fig. 4.8. We find a good agreement with experimental data, in particular for the small contact angles where the lubrication theory is expected to be valid.

We now turn to the measurement of the dynamic contact angle with interferometry. These measurements were performed for two different liquids, squalene and ethanol, on a substrate coated with DDMCS. We used these systems because their

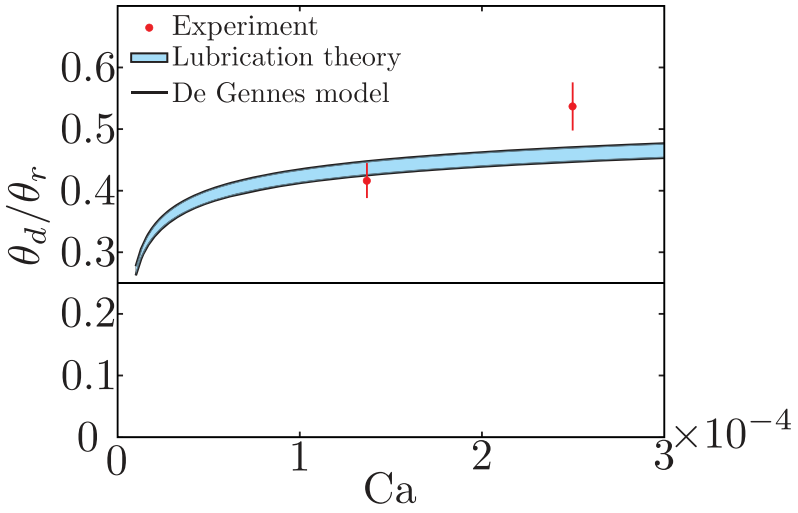

Figure 4.9: Dynamic contact angle, represented as θ_d/θ_r, for squalene and ethanol on a substrate coated with DDMCS (red dots). The blue zone represents the theory of Eq. 4.7 from Snoeijer & Eggers [16] (using the same range of parameters as in Fig. 4.8), compared to the value 0.25 predicted quoted in [1] (solid line).

static contact angles θ_r are sufficiently small to allow for an interferometric measurement. The results are presented in Fig. 4.9 (red disks). The blue region again visualizes the prediction from lubrication (Eq. 4.7), for the same range of parameters (film thickness h_f, slip length λ, and half width w) as for the capillary number. The experimental data are in good agreement with the lubrication-based theory, and clearly rule out the prediction $\theta_r/\theta_d = 0.25$ from [1].

4.5 Forces affecting the dewetting rim

Up to now we have been describing the dewetting rim in absence of external forces. Now we turn to the various types of external forcings that occur during wafer cleaning and drying in an industrial context. First we focus on the extent to which centrifugal forces from spinning influence the dewetting dynamics. In addition, we report two instabilities of the dewetting rim due to centrifugal forces. Next, we investigate the influence of a continuous flux of gas along the surface. Finally we study the influence of Marangoni forces by adding the vapor of organic solvents to the gas flux.

4.5.1 Centrifugal forces

Dewetting velocity

The experiments were performed under the same conditions as described above (Fig. 4.6), with the addition of spinning the substrate at a constant rate during the dewetting phase. Spinning adds centrifugal forces acting on the rim, which, are expected to enhance the dewetting motion. To quantify the effect of centrifugal forces, we used three liquids: isopropanol, ethanol and 1,2-propanediol. As substrate we used a pfDDMCS coating. The receding static contact angles θ_r with the substrates were 44^o, 46^o, and 69^o, respectively (see also Table. 4.1). The spinning rate was varied from 0 up to 80rad/s. $r(t)$ curves were extracted with the image analysis described above.

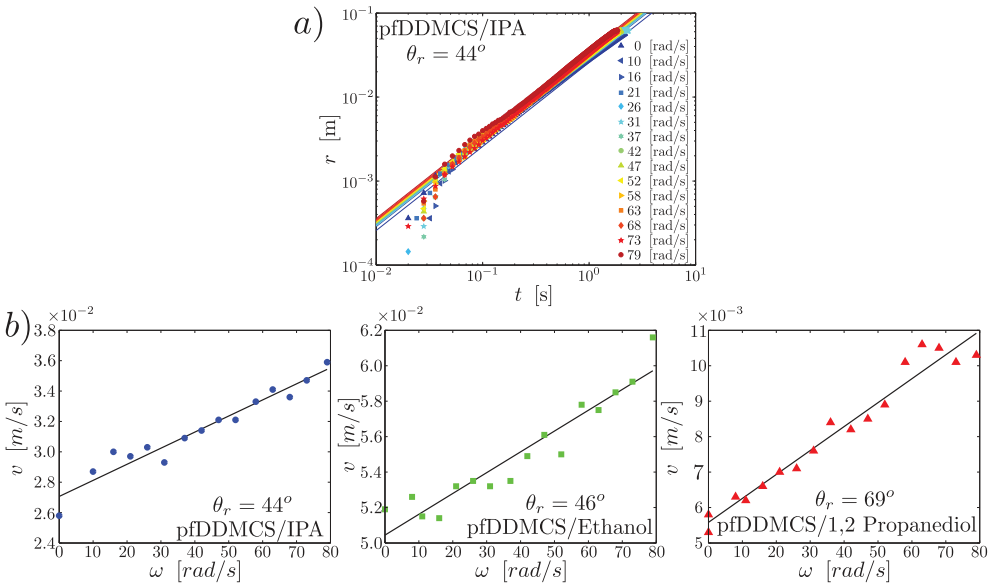

Figure 4.10: Spinning increases the velocity of drying. *a*) drying radius as a function of time for different spinning rates. *b*) The velocity increases linearly with the spinning velocity, for the three systems indicated in the header of the plots.

Figure 4.10*a*) shows the result for isopropanol. Again, the dewetting velocity is constant after a short initial phase. The constant velocity indicates that the ongoing centrifugal thinning of the outer film is negligible compared to the effect of the centrifugal forces onto the rim itself. The data indeed reveal an increase in the dewetting velocity as a function of the spinning rate (note that data are on a log-log scale). This increase is analyzed in Fig. 4.10*b*), where the three panels correspond to the three

different liquids. Within our accessible range of rotational speeds, up to 80rad/s, we observe a linear increase of the dewetting velocity with spinning rate. However, the increase in velocity is not the same for all systems. Since isopropanol and ethanol have a similar surface tension, the contact angles are similar, but the viscosity of isopropanol is twice as large as compared to ethanol. The increase in velocity for isopropanol is around 33%, while for ethanol is smaller, only 20%. In both cases, the *initial* films were prepared with identical spinning rates and times. Thus, the isopropanol films are thicker that the ethanol films. This suggests that the relative influence of the centrifugal forces is stronger for larger initial film heights. For the experiments of Fig. 4.10*b*), the initial film thicknesses for ethanol and isopropanol are 20μm and 40μm for 1,2-propanediol. However, a much larger enhancement of the dewetting velocity is observed for 1,2-propanediol: here the dewetting velocity is increased almost by a factor two. This liquid has a significantly larger contact angle than the other two, which is most likely the reason of the more pronounced enhancement.

Our results clearly demonstrate that spinning substantially enhances the (nonetheless constant) dewetting velocity. To firmly conclude on the underlying physical mechanisms, these experiments should be repeated with a wider range of parameters.

Instabilities

An interesting observation for dewetting while spinning is the appearance of two kinds of instabilities. The first one occurs at the very beginning of the dewetting process, when the rim loses its axisymmetry and forms "pearls". This is demonstrated in Fig. 4.11, which shows the dewetting rim for 1,2-propanediol on a substrate coated with pfDDMCS ($\theta_r = 69^o$) – with and without rotation. Figure 4.11*a*) is the process without rotation, revealing a nearly perfectly axisymmetric rim. Figure 4.11*b*) shows that, when rotating, one clearly observes an instability of the dewetting rim toward the formation of a large number of drops.

This result strongly resembles the breakup of a liquid jet, *i.e.*, the Rayleigh-Plateau instability [1]. The onset of this instability can be understood by considering the change in interfacial area of a liquid cylinder (radius R), when imposing a periodic variation of wavelength λ. For wavelengths larger than a critical value

$$\frac{\lambda}{R} = 2\pi, \tag{4.9}$$

the interfacial area is reduced by the perturbation, leading to the instability. The

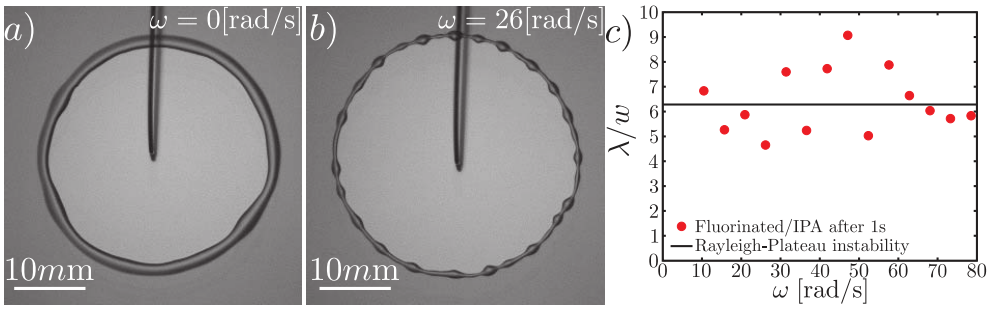

Figure 4.11: Pearling instability of the dewetting rim due to rotation. *a*) Dewetting at $\omega = 0$ gives a nearly axisymmetric liquid profile. *b*) Dewetting at $\omega = 26$ rad/s reveals an instability towards droplet formation. *c*) The wavelength λ normalized by the half-width of the rim w as a function of the spinning rate ω. The solid line represents the stability boundary for the classical Rayleigh-Plateau instability of a free liquid cylinder with a radius $R = w$.

wavelength of maximum growth rate is a multiple of this critical wavelength, though the precise value depends on details of the fluid dynamics. To verify that the instability in Fig. 4.11 is indeed related to the Rayleigh-Plateau instability, we determine the typical wavelength in our experiment at different spinning rates. The result is shown in Fig. 4.11*c*). The ratio is approximately independent of ω, supporting a Rayleigh-Plateau like mechanism. Also, the wavelength much larger than the width of the rim. The black solid line is the stability boundary for a free liquid jet of radius $R = w$ of the Rayleigh-Plateau instability. Some datapoints fall below this boundary. This can be attributed to the difference in geometry of the dewetting rim as compared to the free jet: since the contact angle is below 90^o, the radius of curvature of the free surface is larger than the width of the rim. The energetics of a rivulet on a substrate, *i.e.* cylindrical cap of finite contact angle, was previously assessed in Diez *et al.* [21] and Davis [20]. It was found that below 90°, the stability boundary is only slightly reduced with respect to (4.9), when taking w instead of R. However, in the present case the rivulet is connected to a liquid film, which will surely affect the details of the geometric variations and the hydrodynamics of the growth of the instability. A full linear stability analysis of the two-dimensional lubrication equations would be required to resolve this issue.

The second kind of instability appears due centrifugal forces exerted on the pearls by the spinning, as shown in Fig. 4.12. The snapshots in Fig. 4.12 *a*) and *b*) are taken from dewetting experiments using 1,2-propanediol on a substrate coated with pfD-

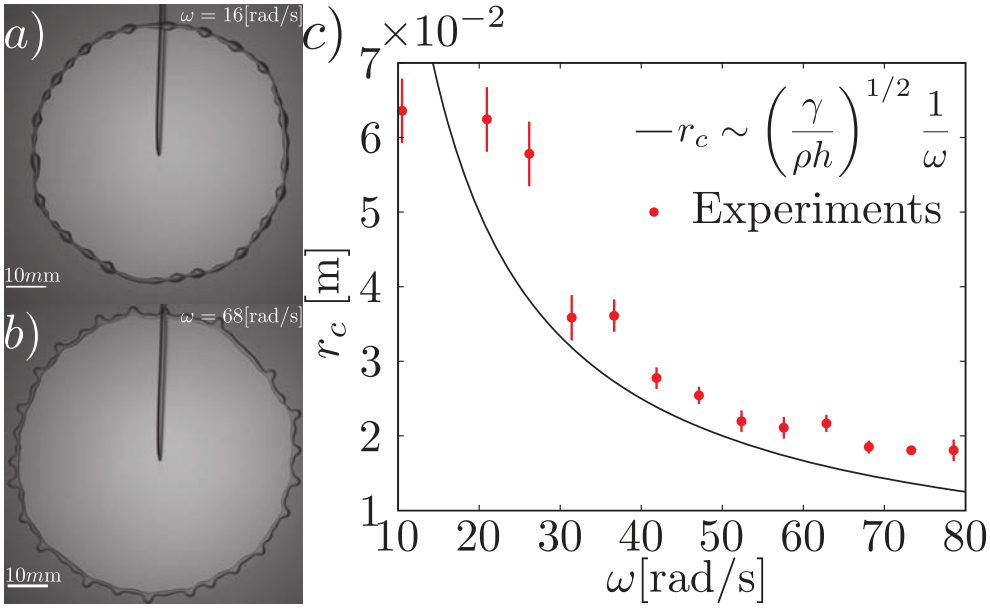

Figure 4.12: Destabilization of droplets under the influence of spinning, comparing different spinning rates: *a*) $\omega = 16$ rad/s, *b*) $\omega = 68$ rad/s. *c*) The onset of the instability is characterized by a critical hole radius r_c that decreases with ω. The solid line corresponds to (4.12).

DMCS, at different rotation rates. In Fig. 4.12*a*) we see the "pearling" instability, that occurs when rotation is applied, as discussed in the previous section. In Fig. 4.12*b*), these pearls are stretched out radially under the influence of centrifugal forces. We have observed that, for a given spinning rate, there is a critical distance r_c at which the elongation of the pearls becomes evident. This is shown in Fig. 4.12*c*). The critical radius is plotted as a function of ω. The larger the spinning rate, the earlier the instability appears.

We can explain this behavior from a balance of surface tension versus centrifugal forces. While surface tension acts to retain the drops, centrifugal forces accelerate the drops in outward direction. To quantify this balance, we first need to estimate the volume of liquid that is present in the rim (see Fig. 4.13). Since the initial thickness is known, the volume of liquid contained in the rim is $V_1 = \pi r^2 h_f$. At a later stage, as depicted in Fig. 4.13*b*), we can calculate the volume of the rim as a torus with a cross section of a circular segment with area $A = f(\theta)\, w^2$, where

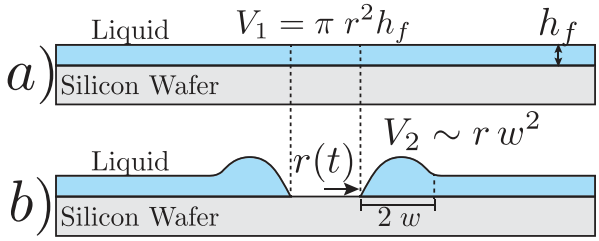

Figure 4.13: A cross section of the dewetting rim before, *a*), and after it was formed, *b*). Since mass is conserved, the total volume of the liquid in both stages is the same. Two ways to quantify the volume of the rim, lead to the expression used to compute the critical radius of the instability.

$f(\theta) = (\pi - 2\theta - 2\sin\theta)/\cos\theta$ and θ is the contact angle of the rim. Therefore the volume of the torus is obtained by integrating the area A along the perimeter, leading to $V_2 = 2\pi r f(\theta) w^2$. Since the mass of liquid remains unchanged, we can equate the two volumes and hence find the scaling law $w^2 \sim r\, h_f$.

Now, we estimate the retaining force due to surface tension, which per unit length is of the order

$$F_{ca} \sim \gamma. \tag{4.10}$$

On the other hand, the centrifugal force acceleration $r\omega^2$ yields a force per unit length,

$$F_{ce} \sim \rho A\, r\, \omega^2 \sim w^2\, r\, \omega^2, \tag{4.11}$$

pushing on the drops. The onset of the instability arises when the force (4.11) overcomes (4.10). When adding the result of mass balance $w^2 \sim r\, h_f$, this gives a prediction for the critical radius:

$$r_c \sim \left(\frac{\gamma}{\rho h_f}\right)^{1/2} \frac{1}{\omega}. \tag{4.12}$$

The factor $\sqrt{\gamma/\rho h_f}$ in this expression depends of the properties of 1,2-propanediol as well as the film height in the experiment. The surface tension is reported in Table. 4.1 and the density is $\rho = 1040\,\mathrm{kg/m^3}$. The height of the film in the experiment is 50μm. The black solid line in Fig. 4.12*c*) corresponds to the scaling law (4.12), where for simplicity we assumed that the prefactor is 1. This indeed gives a very accurate description of the data, and as such provides a good explanation for the destabilization of the pearls.

4.5.2 The effect of a flux of gas on the surface on the dewetting velocity

In industrial processes, such as spin drying, an additional flux of dry gas, such as nitrogen, is often used in order to increase the evaporation rate and/or to enhance the dewetting velocity. This type of external forcing couples to the hydrodynamics in the liquid film as an additional shear stress at the surface.

In the following paragraphs, we describe experimental results on the influence of a dry gas flow. Otherwise, the same conditions as described in the experimental section, were left unchanged. The additional gas flux was provided by an extra needle and a mass flow controller set to a constant flow rate. Additionally, the spin coater was covered with a glass plate. The latter had one hole at the center (to provide access to the substrate for the needels) and a series of holes around the periphery. The outer holes served as a gas outlet. This way, the gas flux, which was fed to the center of the wafer, created a radial outward flow over the wafer surface. It is expected that the addition of a shear stress in outward direction would increase the dewetting velocity.

We measured the radius as a function of time for different gas flow rates. The needle (inner diameter $\approx 1m$m.) was fixed at a determined height of the substrate ($\approx 4m$m). In order to control the flux, we used a mass flow controller that varies the gas input from 1L/min to 20L/min. In this series of experiments, the minimum radius we could measure starts around $5m$m, just above the size of the hole in which the needles are inserted. These measurements are presented in Fig. 4.14*a*).

We observe that for early times, the dewetting rim moves faster as compared to the case without gas flux (blue triangles). However, for later times, the slopes of all the curves become similar, regardless of the gas flow rate. The effect of blowing gas remains localized at the center of the dewetting hole. It becomes negligible as the rim moves outward. This observation is confirmed in Fig. 4.14*b*) where the velocities of dewetting are plotted as a function of time for the same datasets. The initial dewetting velocities are larger, but all curves collapse for later times. The black solid lines represents the velocity of dewetting without gas flux.

Fig. 4.14 shows that the influence of the gas flux decays with r. This most likely due to the radially decreasing velocity in the gas flux: according to mass conservation, the azimuthally integrated gas flux must be constant with respect to r, and thus the velocity decreases as $\sim 1/r$. However, this could also be an artifact created by the mass flow controller: Upon opening, the mass flow controller creates a rather big overshoot. Indeed, we observed the formation of a certain waviness on the central

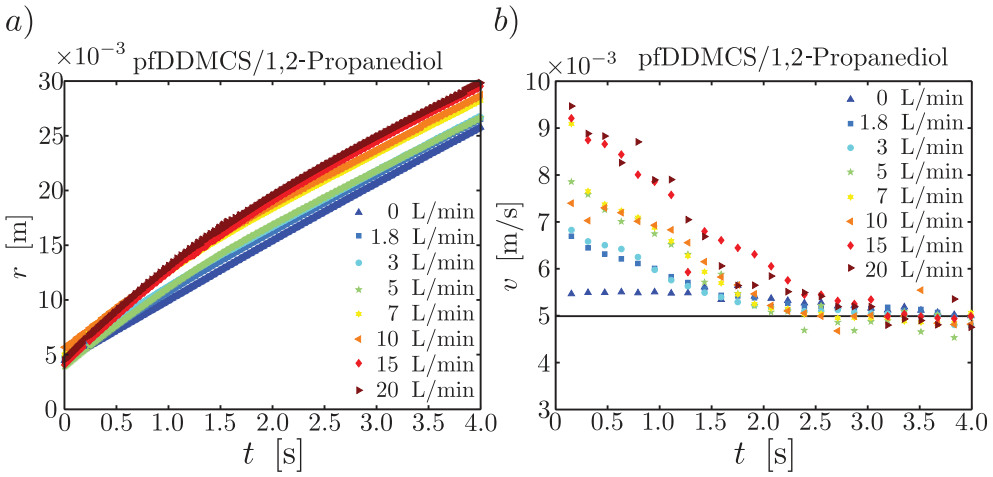

Figure 4.14: Spinning increases the velocity of drying. *a*) drying radius as a function of time for different spinning rates. *b*) The velocity increases linearly with the spinning velocity. The system is indicated in the header of the panels.

part of the film, immediately after the mass flow controller was opened.

4.5.3 How Marangoni forces affect the dewetting rim

Finally, in industrial applications, the opening of the dewetting rim is freqently also supported by vapors of organic solvents (such as isopropanol) within the gas flux. Such vapors will be absorbed by the film and thus lead to surface tension gradients. The flows caused by surface tensions gradients are known as the Marangoni effect, and, accordingly, this technique of drying surfaces is called Marangoni drying [22].

Here, we made some qualitative tests in which Marangoni forces were introduced by adding vapor of organic solvents to the gas flow. However, controlling the involved parameters is rather difficult. We thus limit ourselves to reporting on the appearance of instabilities that, nevertheless, we found fascinating enough so that they should be reported.

In this series of experiments we use nitrogen gas that was bubbled through either ethanol or isopropanol prior to flowing it onto the substrate. Both organic solvents have low surface tensions. Since Marangoni flows are more relevant for small contact angles [26, 27], we performed the experiments on surfaces modified with VDMCS

(compare table 4.2). In Fig. 4.15 we show different effects appearing for early times, depending on the combination of liquids in both the vapor and the liquid phase.

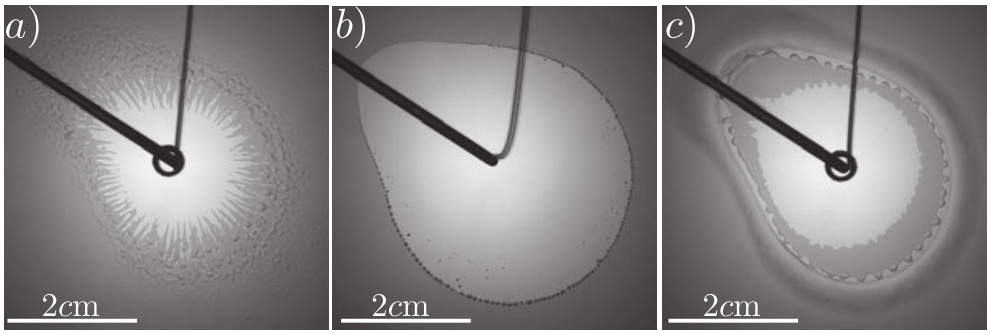

Figure 4.15: When blowing vapor of a low surface tension organic solvent, instabilities appear. These images show snapshots of experiments where a flux of isopropanol vapor was blown onto a film of ethanol. The substrate was coated with VDMCS. *a*) The film of ethanol is very thin (5μm). Here we observe the formation of "pointy" fingers that refuse to dewett. *b*) Evaporation was enhanced by removing the lid of the spin coater. On the contact line regular and uniform pearls form, thickness is around $h_f \sim 30\mu$m. *c*) The film is around $h_f \sim 200\mu$m thick. Tears are formed in the vicinity of the needle.

Fig. 4.15*a*) shows a very thin layer of ethanol ($h_f \sim 5\mu$m) on a VDMCS surface. The gas flux onto the film contains isopropanol vapor. In this case, the surface tension of the vapor is slightly smaller than the surface tension of the liquid. Instabilities nucleate, and, as shown in the outer part of the image, a "granular" texture forms due the Marangoni forces. To the inside of the rim, a "fingering" instability appears, with the fingers pointing to the center of the dewetting hole. The morphology of these fingers is very different from the ones shown in Fig. 4.12*b*), the tips appear very sharp.

Fig. 4.15*b*) shows the same combination of liquids as before (ethanol film, isopropanol vapor), but the film thickness is higher: $h_f \sim 20\mu$m. In addition, evaporation was enhanced by removing the lid. In this experiment the contact line shows a pearling instability, which has a remarkably different morphology from the one shown in the spinning case. Here the pearls are very small but also very rounded, collecting almost all the liquid of the dewetting rim. Therefore, the wavelength is much smaller as compared to the Rayleigh-Plateau like instability for dewetting with spinning (see above). Evaporation is enhanced by the removal of the lid, and the va-

por supply is more centered on the film. Thus the Marangoni effect is enhanced at the contact line where the tears form. Fig. 4.15*c*) shows the same combination of liquids for a very thick film $h_f \sim 200\mu$m. This is enough liquid that, even after nucleating a hole with dry nitrogen vapor, the ethanol film will re-wet the entire surface. With continuous blowing of dry nitrogen, a dewetting hole of a certain stable size is observed. However, with isopropanol vapor in the gas flux, Marangoni tears appear at the edge of the region affected by the blowing. Outside this region, a rim containing a significant amount of liquid is formed.

While these effects appear immediately after the vapor is in contact with the surface, other phenomena appear at some distance to the impinging jet. The outer regions are not affected by the mechanical forced excerted by the jet. Therefore, the solutal Marangoni forces which will nonetheless act here, can be studied separately. Fig. 4.16*a*) shows the combination of an isopropanol film with vapor of the same liquid, isopropanol, in the gas flux. Although, in principle, identical liquids should not produce Marangoni effects, a series of water drops are left by the dewetting rim. We believe this phenomena occurs due the water content within the isopropanol on the substrate (isopropanol is hygroscopic; using isopropanol from a bottle that was opened long time ago, inevitably means that the water content has increased). When the aged isopropanol has evaporated, a film of water may remain on the surface. Such a layer will destabilize intro droplets if it is put into contact with a remaining vapor flux of isopropanol.

Finally in Fig. 4.16*b*) shows the combination of an ethanol film with isopropanol vapor (as in Figs. 4.15*a*) to *c*)), but at later times and with a thick initial film ($h_f \sim 200\mu$m). It can be seen that the dewetting rim emits a structure with a fingering instability that resembles the structure of “veins”. Initially, these features appear at the rim and later on extend out to the perimeter of the wafer.

Despite the beauty of these phenomena, we found no improvement when using Marangoni forces to increase the velocity of dewetting. However, a more extensive study of these effects is suggested in order to gain some insight in further possibilities. We advise a variation of liquids and vapors in order to vary the properties and strength of the Marangoni forces.

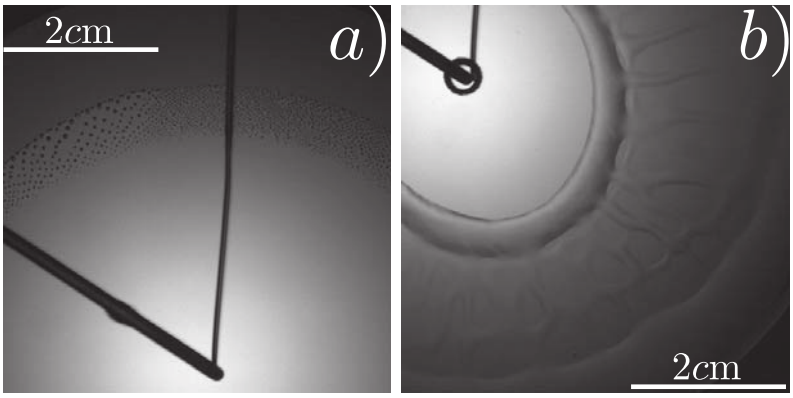

Figure 4.16: Snapshots of experiments showing surface tension gradient effects at long times. Both substrates are VDMCS. *a*) shows isopropanol at the liquid and the vapor phase. The film thickness is around $h_f \sim 30\mu$m. Evaporation is enhanced by removing the lid. We observe regular drops remaining at the surface, presumably absorbed water from the isopropanol bottle. *b*) The liquid of the film is ethanol and the vapor phase is isopropanol. The film is considered thick, $h_f \sim 200\mu$m. At long times, we observe the appearance of a fingering instability that points outward from the dewetting rim.

4.6 Discussion and conclusions

We experimentally studied the dynamics of the dewetting rim. Using two different visualization methods, we quantified the global dewetting dynamics as well as the dynamic contact angle. Using a variety of substrate modifications and several different liquids, we measured the dewetting velocity and the dynamic contact angle for a wide range of viscosities η, surface tensions γ, and static receding contact angles θ_r. We recover the classical hydrodynamic scaling Ca $\sim \theta_r^3$, previously reported in [1, 3, 14, 15]. We show that the dynamic contact angle is larger than predicted by de Gennes *et al.* [1], but agrees with a lubrication-based theory [16].

We also tested the influence of different additional forcings on the dynamics of the dewetting rim. It was observed that centrifugal forces have an influence on the dewetting velocity and can increase it by a significant amount. In addition, we found that spinning induced two kinds of instabilities. The first is reminiscent of a Rayleigh-Plateau instability: the rim deformes into a series or droplets. The second instability concernes the stability of the newly formed drops toward centrifugal elongation (sim-

ilar to viscous fingering) and occurs beyond a (frequency dependent) critical radius.

Furthermore we tested two other types of external forcings that are often encountered in practical applications. These were, on the one hand, blowing gas at the center of the wafer, in order to increase mechanically the shear rate at the surface of the liquid film. On the other hand, we were blowing vapor of an organic solvent at the film to induce Marangoni flows inside the film. None of these were found to significantly increase the velocity of dewetting. However, blowing dry gas accelerated the dewetting velocity locally, very close to the source of gas. Marangoni effects decreased dramatically the control on the experiment, leading to a family of phenomena that, despite being beautiful and interesting, do not fulfill the purpose of improving the contact line mobility. We believe that more experiments, including a wider variation in the liquids and substrates used, will lead to results in which the contact line could be manipulated in a more controlled and predictable way.

References

[1] P.G. de Gennes, F. Brochard-Wyart & D. Quéré. Capillarity and wetting phenomena: drops, bubbles, pearls, waves. *Springer*, 2004.

[2] D. Bonn, J. Eggers, J. Indekeu, J. Meunier & E. Rolley. Wetting and spreading. *Rev. Mod. Phys.*, **81** (2), 739:, 2009.

[3] J.H. Snoeijer & B. Andreotti. Moving contact lines: scales, regimes, and dynamical transitions. *Annu. Rev. Fluid Mech.*, **45**, 269:292, 2013.

[4] R.J. Daniello, N.E. Waterhouse & J.P. Rothstein. Drag reduction in turbulent flows over superhydrophobic surfaces. *Phys. Fluids*, **21** (8), 085103, 2009.

[5] J.P. Rothstein. Slip on superhydrophobic surfaces. *Annu. Rev. Fluid Mech.*, **42**, 89:109, 2010.

[6] T. Liu, Y. Yin, S. Chen, X. Chang & S. Cheng. Super-hydrophobic surfaces improve corrosion resistance of copper in seawater. *Electrochim. Acta*, **52** (11), 3709:3713, 2007.

[7] L. Mishchenko, B. Hatton, V. Bahadur, J.A. Taylor, T. Krupenkin & J. Aizenberg. Design of ice-free nanostructured surfaces based on repulsion of impacting water droplets. *ACS nano*, **4** (12), 7699:7707, 2010.

[8] G. Reiter. Dewetting of thin polymer films. *Phys. Rev. Lett.*, **68** (1), 75, 1992.

[9] F. Saulnier, E. Raphaël, & P.G. de Gennes. Dewetting of thin polymer films near the glass transition. *Phys. Rev. Lett.*, **88** (19), 196101:, 2002.

[10] R. Seemann, S. Herminghaus & K. Jacobs. Gaining control of pattern formation of dewetting liquid films. *Journal of Physics: Condensed Matter*, **13** (21), 4925, 2001.

[11] R. Fetzer, K. Jacobs, A. Münch, B. Wagner & T.P. Witelski. New slip regimes and the shape of dewetting thin liquid films. *Phys. Rev. Lett.*, **95** (12), 127801, 2005.

[12] F. Saulnier, E. Raphaël & P.G. de Gennes. Dewetting of thin-film polymers. *Phys. Rev. E*, **66** (6), 061607, 2002.

[13] S. Herminghaus, R. Seemann & K. Jacobs. Generic morphologies of viscoelastic dewetting fronts. *Phys. Rev. Lett.*, **89** (5), 056101, 2002.

[14] C. Redon, F. Brochard-Wyart, F. Rondelez. Dynamics of dewetting. *Phys. Rev. Lett.*, **66** (6), 715, 1991.

[15] F. Brochardwyart, J.M. Dimeglio & D. Quéré. Dewetting-growth of dry regions from a film covering a flat solid or a fiber. *Comptes Rendus De L Academie Des Sciences Serie II*, **304** (11), 553, 1987.

[16] J.H. Snoeijer & J. Eggers. Asymptotic analysis of the dewetting rim. *Phys. Rev. E*, **82** (5), 11823:056314, 2010.

[17] P.G. de Gennes. Deposition of langmuir-blodgett layers. *Colloid and Polymer Sciences*, **264** (5), 463:465, 1986.

[18] J.F. Joanny & P.G. de Gennes. Upward creep of a wetting fluid: a scaling analysis. *Journal de Physique*, **47** (1), 121:127, 1986.

[19] J.C. Flitton & J.R. King. Surface-tension-driven dewetting of Newtonian and power-law fluids. *Journal of Engineering Mathematics*, **50**(2:3) (241:266), 2004.

[20] S.H. Davis. Moving contact lines and rivulet instabilities. Part 1. The static rivulet. *J. Fluid Mech.*, **98** (02), 225:242, 1980.

[21] J.A. Diez, A.G. González & L. Kondic. On the breakup of fluid rivulets, *Phys. Fluids*, **21** (8), 082105, 2009.

[22] A.F.M. Leenaars, J.A.M. Huethorst, & J.J. Van Oekel. Marangoni drying: a new extremely clean drying process. *Langmuir*, **6** (11), 1701:1703, 1990.

[23] A. Eddi, K.G. Winkels & J.H. Snoeijer. Influence of droplet geometry on the coalescence of low viscosity drops. *Phys. Rev. Lett.*, **111** (14), 144502, 2013.

[24] J.F. Hernández-Sánchez, L.A. Lubbers, A. Eddi & J.H. Snoeijer. Symmetric and Asymmetric Coalescence of Drops on a Substrate. *Phys. Rev. Lett.*, **109** (18), 184502, 2012.

[25] S. Karpitschka & H. Riegler. Quantitative Experimental Study on the Transition between Fast and Delayed Coalescence of Sessile Droplets with Different but Completely Miscible Liquids. *Langmuir*, **26** (14), 11823:11829, 2010.

[26] S. Karpitschka & H. Riegler. Noncoalescence of Sessile Drops from Different but Miscible Liquids: Hydrodynamic Analysis of the Twin Drop Contour as a Self-Stabilizing Traveling Wave. *Phys. Rev. Lett.*, **109** (6), 066103, 2012.

[27] S. Karpitschka & H. Riegler. Sharp transition between coalescence and non-coalescence of sessile drops. *J. Fluid Mech.*, **743**, 2014.

[28] C.W. Berendsen, J.C. Zeegers, G.C. Kruis, M. Riepen & A.A. Darhuber. Rupture of thin liquid films induced by impinging air-jets. *Langmuir*, **28** (26), 9977: 9985, 2012.

5
Conclusions and Outlook

In this thesis different types of capillary free surface flows are studied. The topics discussed are mainly the coalescence of viscous sessile drops, the Marangoni-spreading of locally deposited drops on a thin water film and the dynamic contact angle of the dewetting rim and the effect of external forcing on the rim velocity. In this Chapter we will review conclusions for each topic and propose an outlook on future work.

On the coalescence of viscous sessile drops

In Chapter 2, we obtained fundamental insight in understanding the coalescence of viscous sessile drops. It was demonstrated that the initial coalescence of drops on a substrate, which is manifestly a three-dimensional process, is described quantitatively by a one-dimensional model. Based on the lubrication approximation, we found similarity solutions describing the temporal dynamics and the shape of the bridge connecting the drops. Both the shapes and the dynamics accurately describe the experimental results. An additional similarity solution of the lubrication approximation equation was derived, which can also describe the coalescence of two drops with different contact angles. As a result, dimensionless horizontal and vertical velocities characteristic of the contact angle ratio were determined theoretically and experimentally. It was experimentally corroborated that there is effectively no influ-

ence of the contact line in the coalescence process. This is highly surprising, since fluid motion is usually strongly inhibited by the famous moving contact line singularity. Here, this somehow does not play a role and deserves further explanation in the future.

Inspired by the results presented in Chapter 2, a natural question was raised: What is the behavior of the bridge joining two inertially dominated sessile drops? To answer this question in detail Eddi *et al.* [1] studied experimentally the coalescence of sessile water drops, which have a much lower viscosity than the drop in Chapter 2. The dynamics of the bridge was once again described by self-similarity solutions. So the concept of self-similarity during coalescence, discovered in this thesis, applies beyond the viscous lubrication limit. Intriguingly, it was found that the exponent changed (from two thirds to one half) when the contact angle approaches 90^o. For contact angles smaller than 90^o, the height of the bridge follows a scaling of $h \sim t^{2/3}$. While at 90^o the geometry induces a fundamental change in the bridge dynamics, resulting in $h \sim t^{1/2}$. It would be interesting to investigate whether such a transition also arises for very viscous drops of high contact angles.

Another interesting question arises when observing the differences in the coalescence of drops from two different directions. On the one hand the bottom view showed that the width of the bridge scales as $w \sim t^{1/2}$[2] for viscous drops. While on the other hand, from the side, we found that the height scales linearly with time $h \sim t$. Despite the different exponents, both the measurements represent the evolution of bridge size. Therefore, using geometrical arguments these two observations could be combined, unifying the physics.

Finally, it would be interesting to study the bridge dynamics during coalescence of non-Newtonian liquids. At the onset of the coalescence, there is a big curvature joining the bridges, which is translated into a big shear stress at the surface. As the bridge grows, the curvature gets smaller as well as the stress. Then it is natural to propose that the scaling of the bridge would be modified with liquids with shear thickening or thinning, or even visco-elastic rheology.

On Marangoni spreading

In Chapter 3 we investigated the Marangoni spreading that arises when droplets of IPA-water mixtures are deposited on a thin film of water. We identified the parametric dependence of the radius of spreading with the flux of liquid, the surface tension and

viscosity, which is achieved by varying the IPA-water concentrations of the deposited droplets. Based on a balance between Marangoni and viscous stresses, we proposed a scaling law that was experimentally confirmed by a data collapse.

The experimental setup in Chapter 3 can be seen as a systematic version of the work by Thomson [3], in which liquids with different surface tensions were mixed. Here it was reported that when pouring a liquid with a lower surface tension on a thin layer, an even thinner region appears. In previous work, several experiments have been carried out using surfactants instead of a different liquid composition, as showed in the reviews by Matar & Craster [4] and Craster & Matar [5]. Despite the notable similarities between the experiments, *i.e.* the spreading dynamics and the thinning of the film, some differences stand out. Surfactants are usually supplied in quantities per unit area, while the flux of IPA-water is naturally imposed per unit volume. In addition, in contrast to insoluble surfactants the mixing takes place in all the volume of the film. Hence, the concentration profile also has a component in the vertical direction and prevents using the 1D lubrication approximation to model the system. A consequence of this difference is that contrarily to the case of surfactants, the film thickness of the initial film is irrelevant for the dynamics.

The delayed coalescence between sessile drops [6] presents similarities with the experiments in Chapter 3. In both cases the contact of liquids with different surface tensions lead to a motion of the bridge connecting the two regions towards the liquid with the high surface tension. In the case of the delayed coalescence the position of the bridge scales linearly with time, while for our spreading experiments, it scales as the square root of time. The difference can be attributed to a different geometry of the concentration gradient. On the one hand in the delayed coalescence the whole system is being translated at a constant surface tension gradient. On the other hand the gradient of the spreading liquid is continuously being elongated, because the point where liquid is being injected has a fixed concentration. This change in geometry explains the difference in the observed scaling. It illustrates that when applying Marangoni forces for drying purposes in a technological context, the flow geometry is of prime importance.

On dewetting

In Chapter 4 we performed experiments on the dewetting of a thin film deposited on a hydrophobic surface, measuring the velocity of dewetting as a function of the liquid properties and the receding contact angle with the substrate. These experiments

confirmed the classical prediction given by Redon *et al.* [8] of $Ca \sim \theta_r^3$. Furthermore, using single wave interferometry we measured the dynamic contact angle of the dewetting at a micrometric scale. These measurements were directly compared with the contradictory predictions by de Gennes [9] and the lubrication theory by Snoeijer & Eggers [10]. Our results are best described by the lubrication theory. The contact angle in our case was measured at a short distance of about $10\,\mu$m from the contact line. Future work should be dedicated to measuring the full rim profile, so that upon extrapolation of a circular cap an alternative definition of the contact angle can be measured.

The second part of Chapter 4 presents the results of spinning the substrate to increase the speed of the dewetting rim. This external forcing resulted in a series of instabilities described on Chapter 4. These instabilities resemble the Marangoni tears for high volumetric concentrations of isopropanol. On the one hand, these instabilities appear when the liquid from the jet is forced via Marangoni forces to spread on a thin film. On the other hand, the instabilities on the dewetting rim appear when centrifugal forces pull the liquid to recede faster. Both instabilities appear due external actuations added to wetting and dewetting processes. The Marangoni instabilities appear at a critical concentration of isopropanol, while the dewetting instabilities are displayed for any spinning rate. Thus the experimental setup in Chapter 3 is a good tool to explore the parameters involved in the transition to these instabilities. Also it would be interesting to perform experiments at IPA concentrations higher than 20%, since the behavior of the instabilities can dramatically change with the parameters. To investigate the effect of viscosity or evaporation on the instabilities, different liquids such as 1,2-propanediol could be used. The effect of high IPA concentrations in the train of drops was limited by the strong wettability on the microdrop nozzle. This problem could be solved using a hydrophobic nozzle.

The dynamics of dewetting is also important from a technological perspective, since any increase of the velocity could speed up the drying processes. In this context, Chapter 4 showed that the speed of dewetting is enhanced up to factor two with spinning for 1,2-propanediol on a surface coated with pfDDMCS. However, the liquid properties as well as the contact angle seem to determine to what extent the dewetting velocity will be enhanced. Studying further the variation on the velocity of dewetting would help in determining its dependency with different parameters. This study could be performed using different liquids and varying the contact angle, while the substrate rotates.

In Chapter 4 we finally investigated the effect on the velocity of the dewetting rim when a jet of gas impinges vertically on the surface. We observed that this flux of gas has a very important effect on the dewetting, increasing the velocity at the onset of the hole by a factor two. However, this effect fades away very quickly as the rim moves away from the gas nozzle. In the process of microprocessor fabrication, the tools make use of an automated arm that displaces the nozzle from the center to the edge of the wafer. Thus, the region that is being influenced by the gas impinging is always close to the contact line. It would be interesting to systematically study the geometry of impinging and its effect on the contact line motion. In the experiments performed in this chapter, the angle of attack of the gas nozzle is 90^o. However a variation on the angle of attack might influence the velocity of dewetting or diminishes the development of instabilities and would be interesting for future work. In the final part of Chapter 4 we investigate the effect of adding Marangoni forces to the gas jet, via vapor of organic solvents. Here we observed many manifestations of Marangoni instabilities, underlining once more the rich phenomenology and the many challenges to achieve a full understanding of Marangoni drying.

References

[1] A. Eddi, K.G. Winkels & J.H. Snoeijer. Influence of droplet geometry on the coalescence of low viscosity drops. *Phys. Rev. Lett.*, **111**(14), 144502, 2013.

[2] W. D. Ristenpart and P. M. McCalla and R. V. Roy and H. A. Stone, Phys. Rev. Lett. **97**, 064501 (2006).

[3] J. Thomson. XLII. On certain curious motions observable at the surfaces of wine and other alcoholic liquors. *The London, Edinburgh, and Dublin Philosophical Magazine and Journal of Science*, **10** (67), 330:333, 1855.

[4] O.K. Matar & R.V. Craster. Dynamics of surfactant-assisted spreading. *Soft Matter*, **5** (20), 3801:3809, 2009.

[5] R.V. Craster & O.K. Matar. Dynamics and stability of thin liquid films. *Rev. Mod. Phys.*, **81** (3), 1131:, 2009.

[6] Karpitschka, Stefan and Riegler, Hans Quantitative Experimental Study on the Transition between Fast and Delayed Coalescence of Sessile Droplets with Different but Completely Miscible Liquids, *Langmuir*, **26** (14), 11823:11829, 2010.

[7] J.H. Snoeijer & B. Andreotti. Moving contact lines: scales, regimes, and dynamical transitions. *Annu. Rev. Fluid Mech.*, **45**, 269:292, 2013.

[8] C. Redon, F. Brochard-Wyart, F. Rondelez. Dynamics of dewetting. *Phys. Rev. Lett.*, **66** (6), 715, 1991.

[9] P.G. de Gennes. Deposition of langmuir-blodgett layers. *Colloid and Polymer Sciences*, **264** (5), 463:465, 1986.

[10] J.H. Snoeijer & J. Eggers. Asymptotic analysis of the dewetting rim. *Phys. Rev. E*, **82** (5), 11823:056314, 2010.

Summary

Capillary and wetting phenomena are an essential part of nature. Its presence is noticed in many circumstances where solid and liquid surfaces come into contact. In this thesis different types of capillary free surface flows are studied. The topics discussed are mainly the coalescence of viscous sessile drops, the Marangoni-spreading of locally deposited drops on a thin water film and the dynamic contact angle of the dewetting rim and the effect of external forcing on the rim velocity.

In Chapter 2, we obtained fundamental insight in understanding the coalescence of viscous sessile drops. It was demonstrated that the initial coalescence of drops on a substrate, which is manifestly a three-dimensional process, is described quantitatively by a one-dimensional model. Based on the lubrication approximation, we found similarity solutions describing the temporal dynamics and the shape of the bridge connecting the drops. Both the shapes and the dynamics accurately describe the experimental results. An additional similarity solution of the lubrication approximation equation was derived, which can also describe the coalescence of two drops with different contact angles. As a result, dimensionless horizontal and vertical velocities characteristic of the contact angle ratio were determined theoretically and experimentally. It was experimentally corroborated that there is effectively no influence of the contact line in the coalescence process. This is highly surprising, since fluid motion is usually strongly inhibited by the famous moving contact line singularity. Here, this somehow does not play a role and deserves further explanation in the future.

Another interesting question arises when observing the differences in the coalescence of drops from two different directions. On the one hand the bottom view showed that the width of the bridge scales as $w \sim t^{1/2}$[1] for viscous drops. While on the other hand, from the side, we found that the height scales linearly with time $h \sim t$. Despite the different exponents, both the measurements represent the evolution of bridge size. Therefore, using geometrical arguments, these two observations could be combined, unifying the physics.

In Chapter 3 we investigated the Marangoni spreading that arises when droplets of IPA-water mixtures are deposited on a thin film of water. We identified the parametric dependence of the radius of spreading with the flux of liquid, the surface tension and viscosity, which is achieved by varying the IPA-water concentrations of the deposited droplets. Based on a balance between Marangoni and viscous stresses we proposed a scaling law that was experimentally confirmed by a data collapse.

The experimental setup in Chapter 3 can be seen as a systematic version of the work by Thomson [2], in which liquids with different surface tensions were mixed. Here it was reported that when pouring a liquid with a lower surface tension on a thin layer, an even thinner region appears. In previous work, several experiments have been carried out using surfactants instead of different liquid composition, as showed in the reviews by Matar & Craster [3] and Craster & Matar [4]. Despite the notable similarities between the experiments, *i.e.* the spreading dynamics and the thinning of the film, some differences stand out. Surfactants are usually supplied in quantities per unit area, while the flux of IPA-water is naturally imposed per unit volume. In addition, in contrast to insoluble surfactants the mixing takes place in all the volume of the film. Hence, the concentration profile also has a component in the vertical direction and prevents using the 1D lubrication approximation to model the system. A consequence of this difference is that contrarily to the case of surfactants, the film thickness of the initial film is irrelevant for the dynamics.

In Chapter 4 we performed experiments on the dewetting of a thin film deposited on a hydrophobic film, measuring the velocity of dewetting as a function of the liquid properties and the receding contact angle with the substrate. These experiments confirmed the classical prediction given by Redon *et al.* [5] of $Ca \sim \theta_r^3$. Furthermore, using single wave interferometry we measured the dynamic contact angle of the dewetting at a micrometric scale. These measurements were directly compared with the contradictory predictions by de Gennes [6] and the lubrication theory by Snoeijer & Eggers [7]. Our results are best described by the lubrication theory. The contact angle in our case was measured at a short distance of about $10\,\mu$m from the contact line. Future work should be dedicated to measuring the full rim profile, so that upon extrapolation of a circular cap an alternative definition of the contact angle can be measured.

The dynamics of dewetting is also important from a technological perspective, since any increase of the velocity could speed up the drying processes. In this con-

text, Chapter 4 showed that the speed of dewetting is enhanced with spinning up to factor two for 1,2-propanediol on a surface coated with pfDDMCS. However, the liquid properties, as well as the contact angle, seem to determine to what extent the dewetting velocity will be enhanced. Studying further the variation on the velocity of dewetting would help in determining its dependency with different parameters. This study could be performed using different liquids and varying the contact angle, while the substrate rotates.

Finally, in Chapter 4 we investigated the effect on the velocity of the dewetting rim when a jet of gas impinges vertically on the surface. We observed that this flux of gas has a very important effect on the dewetting, increasing the velocity at the onset of the hole by a factor two. However, this effect fades away very quickly as the rim moves away from the gas nozzle. In the process of microprocessor fabrication, the tools make use of an automated arm that displaces the nozzle from the center to the edge of the wafer. Thus, the region that is being influenced by the gas impinging is always close to the contact line. It would be interesting to systematically study the geometry of impinging and its effect on the contact line motion. In the experiments performed in Chapter 4, the angle of attack of the gas nozzle is 90^o. However a variation on the angle of attack might influence the velocity of dewetting or diminishes the development of instabilities and would be interesting for future work. Also in the final part of this chapter we investigated the effect of adding Marangoni forces to the gas jet, via vapor of organic solvents. Here we observed many manifestations of Marangoni instabilities, underlining once more the rich phenomenology and the many challenges to achieve a full understanding of Marangoni drying.

References

[1] W. D. Ristenpart and P. M. McCalla and R. V. Roy and H. A. Stone, Phys. Rev. Lett. **97**, 064501 (2006).

[2] J. Thomson. XLII. On certain curious motions observable at the surfaces of wine and other alcoholic liquors. *The London, Edinburgh, and Dublin Philosophical Magazine and Journal of Science*, **10** (67), 330:333, 1855.

[3] O.K. Matar & R.V. Craster. Dynamics of surfactant-assisted spreading. *Soft Matter*, **5** (20), 3801:3809, 2009.

[4] R.V. Craster & O.K. Matar. Dynamics and stability of thin liquid films. *Rev. Mod. Phys.*, **81** (3), 1131:, 2009.

[5] C. Redon, F. Brochard-Wyart, F. Rondelez. Dynamics of dewetting. *Phys. Rev. Lett.*, **66** (6), 715, 1991.

[6] P.G. de Gennes. Deposition of langmuir-blodgett layers. *Colloid and Polymer Sciences*, **264** (5), 463:465, 1986.

[7] J.H. Snoeijer & J. Eggers. Asymptotic analysis of the dewetting rim. *Phys. Rev. E*, **82** (5), 11823:056314, 2010.

Samenvatting

Capillaire en bevochtigingsverschijnselen zijn een essentieel onderdeel van de natuur. Deze fenomenen zijn waar te nemen in situaties wanneer vaste en vloeibare grensvlakken met elkaar in contact komen. Daarnaast speelt bevochtiging een belangrijke rol voor diverse toepassingen. In dit proefschrift worden verschillende types van capillaire stromingen over een vast oppervlak bestudeerd, met als motivatie een beter begrip van het bevochtigen en drogen van wafers in de halfgeleiderindustrie. De onderwerpen zijn achtereenvolgens het samenvloeien van viskeuze druppels liggend op een oppervlak, de Marangoni-uitspreiding van druppels van diverse samenstellingen op een dunne waterfilm, en de dynamica van een terugtrekkende vloeistoflaag.

In hoofdstuk 2 hebben we fundamenteel inzicht verkregen in hoe viskeuze druppels op een vast oppervlak samenvloeien. Een belangrijke bevinding was dat de aanvankelijke samenvloeiing van druppels op een substraat, wat een driedimensionaal proces is, echter kwantitatief kan worden beschreven door een één-dimensionaal model. Op basis van de dunne laag-benadering, vonden we theoretische oplossingen die zowel de dynamica als de vorm van de ontstane brug tussen de druppels beschrijven en laten samenvallen op één curve en bovenal overeenstemmen met de experimentele resultaten. De gevonden oplossingen van de dunne laag-benadering beschrijven niet alleen de samenvloeiing van druppels met gelijke contacthoeken, maar ook het geval waarbij de hoeken van elkaar verschillen. Dit alles resulteerde in zowel een theoretische en experimentele bepaling van de dimensieloze horizontale en verticale snelheden als functie van de contacthoek ratio. Daarnaast is experimenteel aangetoond dat de contactlijn geen wezenlijke invloed heeft tijdens het samenvloeiingsproces. Dit is zeer opmerkelijk, aangezien bevochtigingsdynamica meestal sterk wordt afgeremd door de singulariteit van de contactlijn.

Een ander interessant fenomeen treedt op wanneer de druppelsamenvloeiing wordt bekeken vanuit twee verschillende richtingen. Van onderaf beschouwd bleek, voor viskeuze druppels, de breedte van de brug toe te nemen met de wortel van de tijd: $w \sim t^{1/2}$ [1]. Echter, vanuit het zijaanzicht ontdekten we dat de hoogte lineair schaalt

met de tijd: $h \sim t$. Ondanks de verschillende exponenten geven beide metingen de ontwikkeling van de bruggrootte weer. We hebben laten zien hoe deze twee waarnemingen aan elkaar kunnen worden gerelateerd op grond van geometrische argumenten.

In hoofdstuk 3 hebben we gekeken naar de Marangoni-uitspreiding die ontstaat wanneer druppeltjes, bestaande uit een IPA-water mengsel, worden gedeponeerd op een dunne waterfilm. Onder invloed van verschillen in oppervlaktespanning ontstaat een centrale regio van kleine dikte, die zich uitspreidt in radiale richting. We hebben bepaald hoe de uitspreidingsradius afhangt van de vloeistofstroom, de oppervlaktespanning en de viscositeit, door middel van het variëren van de IPA-water concentraties van de gedeponeerde druppels. Een schalingswet, gebaseerd op een balans tussen Marangoni en viskeuze spanningen, geeft een nauwkeurige beschrijving van de experimentele data.

De meetopstelling in hoofdstuk 3 kan worden gezien als een systematische versie van het werk van Thomson [2], waarin vloeistoffen met verschillende oppervlaktespanningen werden gemengd. In andere onderzoeken werden vergelijkbare experimenten uitgevoerd met behulp van oppervlakte-actieve stoffen, zoals beschreven in de overzichtsartikelen vanMatar & Craster [3] en Craster & Matar [4]. Ondanks de gelijkenis met onze experimenten met IPA-water druppels, zijn er ook enkele opvallende verschillen. De aanvoer van de oppervlakte-actieve stoffen is normaliter opgelegd per oppervlakte-eenheid, terwijl de flux van IPA-water wordt opgelegd per volume-eenheid. Bovendien, in tegenstelling tot onoplosbare oppervlakte-actieve stoffen, mengen de vloeistoffen in het gehele volume van de film. Het meest opmerkelijke verschil is dat, in tegenstelling tot het geval van oppervlakte-actieve stoffen, de dikte van de initiële waterlaag irrelevant bleek voor de uitspreidingsdynamica in onze experimenten.

In hoofdstuk 4 hebben we het ontvochtigen van een dunne laag bestudeerd, nadat deze gedeponeerd was op een hydrofoob oppervlak. De snelheid van ontvochtiging werd gemeten als functie van de vloeistofeigenschappen en de contacthoek. De resultaten bevestigen de klassieke voorspelling gemaakt door Redon *et al.* [5], die de relatie geeft tussen het capillaire getal en de contacthoek als $Ca \sim \theta_r^3$. Bovendien hebben we met behulp van interferometrie de dynamische contacthoek gemeten op een afstand van ongeveer $10\,\mu$m tot de contactlijn. Deze metingen hebben we vergeleken met de tegenstrijdige voorspellingen van de Gennes [6] en de dunne laag-theorie gebruikt in Snoeijer & Eggers [7]. Laatstgenoemde theorie beschrijft onze resultaten het beste. De ontvochtigingsdynamica van een vloeistofslaag is ook

belangrijk vanuit een technologisch perspectief, omdat deze de snelheid van droogprocessen beïnvloedt. In dit verband laten we in hoofdstuk 4 zien dat de snelheid van ontvochtiging voor propyleenglycol op een met pfDDMCS bedekt oppervlak kan worden vergroot met een factor twee door het substraat snel te laten draaien. De vloeistofeigenschappen en de contacthoek lijken echter te bepalen in hoeverre de ontvochtiging kan worden versneld. Het verder variëren van de deze parameters is nodig om de precieze afhankelijkheid van de ontvochtingingssnelheid te bepalen.

Tenslotte onderzochten we in hoofdstuk 4 het effect van een verticale gasstraal op de ontvochtigingssnelheid. We zagen dat deze stroom van gas een belangrijke invloed heeft op het terugtrekken van de vloeistof, waarbij de snelheid aan het begin met een factor twee werd verhoogd. Dit effect verdwijnt echter zeer snel wanneer de vloeistofrand zich verder van de gasstraal verwijderd. In de halfgeleiderindustrie maken machines gebruik van een geautomatiseerde arm die de gasstraal van het midden naar de rand van de wafer verplaatst, de terugtrekkende vloeistof volgend. Dit betekent dat het gebied dat wordt beëinvloed door de gasstraal altijd dichtbij de contactlijn is. Het zou interessant zijn om systematisch de geometrie van de invallende gasstroom te bestuderen en het effect ervan op de verplaatsing van de contactlijn. In het laatste deel van het hoofdstuk onderzochten we het effect van Marangoni krachten aan de gasstroom, via damp bestaande uit organische oplosmiddelen. We zagen vele manifestaties van Marangoni instabiliteiten. Dit onderstreept nogmaals de rijke fenomenologie van ontvochtiging waneer deze wordt gedreven door externe krachten.

References

[1] W. D. Ristenpart and P. M. McCalla and R. V. Roy and H. A. Stone, Phys. Rev. Lett. **97**, 064501 (2006).

[2] J. Thomson. XLII. On certain curious motions observable at the surfaces of wine and other alcoholic liquors. *The London, Edinburgh, and Dublin Philosophical Magazine and Journal of Science*, **10** (67), 330:333, 1855.

[3] O.K. Matar & R.V. Craster. Dynamics of surfactant-assisted spreading. *Soft Matter*, **5** (20), 3801:3809, 2009.

[4] R.V. Craster & O.K. Matar. Dynamics and stability of thin liquid films. *Rev. Mod. Phys.*, **81** (3), 1131:, 2009.

[5] C. Redon, F. Brochard-Wyart, F. Rondelez. Dynamics of dewetting. *Phys. Rev. Lett.*, **66** (6), 715, 1991.

[6] P.G. de Gennes. Deposition of langmuir-blodgett layers. *Colloid and Polymer Sciences*, **264** (5), 463:465, 1986.

[7] J.H. Snoeijer & J. Eggers. Asymptotic analysis of the dewetting rim. *Phys. Rev. E*, **82** (5), 11823:056314, 2010.

Acknowledgements

At the end of last year, the movie “The Hobbit: The battle of the five armies” was presented in theaters all around the world. In the trailer there is a conversation my decaying memory remembers as follows:

> *Bilbo*: ...If I go with you, can you promise I will come back?
> *Galdalf*: No, and if you do, you will not be the same.

Two things called my attention. On the one hand I realized how bad my memory has become, since this was the only book of the saga I read completely and could not recall any of these events. On the other hand, the forgotten conversation had an impact that obviously did not have before. I wished someone had warned me (just like Galdalf did) that the adventure of leaving my home country to study a PhD will put on the line everything I knew. However, the illusion of never leaving the safety of home broke almost immediately as I realized that my former reckless self would have never listened. Despite not being the ring-bearer, nor choosing the most helpful beginning for my acknowledgements, I indeed feel very fortunate in being part of this adventure.

Chronologically I thank the people that made possible that I could arrive, stay and finish the PhD on the Physics of Fluids group. To Roberto Zenit for all the nonsense in the lab, the continuous challenges, the mind games and above all the impulse to grow. I never took the time to thank Devaraj van der Meer for the time he spent teaching me about vibrated granular matter and taking me seriously when I requested a PhD the last day before finishing my internship. To Detlef Lohse for the opportunity and the trust. To the most involved supervisor I could I think of, Jacco Snoeijer; for his endless patience when explaining asymptotics, for the discussions about the colors of the plots, for all the comments and corrections. To Chao, for all the funny little talks. To Michel Versluis for the space in the lab as well as the instructions to keep us safe inside it.

To Antonin, for his e-mails at 3am in the morning, the wise statements during *les petites pauses-cigarette*, his support inside and outside the lab and the body-guarding

on the D-day. To Luuk, for his smart questions and the even smarter answers. To Wolter, for sharing the pleasure of trying a crazy idea, the continuous improving and the arduous work. To Stefan, for being a crack-shot and never hesitating in sharing your experimental skills.

To Joanita, for taking care of the administrative needs, but most important all the background work that I never realized is required. To Gert-Wim, Bas and Martin, I cannot imagine the last four years in the lab being so much fun without your guard.

To the PoF members, Tim, Mark-Jan, Pascal, Olex, Michiel, Varghese, Vampsi, Claas Willem, Jannis, Rodrigo, Dennis, Richard, Marie-Jean, Marine, Henry, Hélène, Tak, Tobias, Elena, Roeland, Wilco, Elisabeth, Erwin, Hanneke, Tess, Joost, Biljana, Alexander, Yoshi, Theo, Ivo, Ceyda and Laura. Thanks for all the voluntary and the involuntary knowledge, the help to find solutions and the missing equipment.

To the old friends that have been part of this journey from the beginning and the new friends that I found here. The adventures we had, have become an important part of me. To Kike, for the body guarding, but above of all, the success and the broken cycles that lead to the start of new ones. To Niya, for the dinner, the evening laughs, we made it my friend. To Guillaume, for the talks, the cultural shocks, the beers, the time and what follows. To María, for the great time in Enschede and the cozy hideout during my visit. To Arturo, for the jogging, the advises, the ideas and the projects. To Julián, for the free couch crashing, the occasional food and music. To Sander Huisman, for the movie nights, the programming lessons, the zero-ugly-font-tolerance, but mostly the two years of unlimited and the most inappropriate conversations I could think of. To Rodolfo, for the travels, the history lessons, the cultural issues and the surprise coffee-breaks. To Rianne, for the most interesting chat in a long time, the support in the *sammenvatting*. To Olga, for the induced gossip, the running club, the running-again club, the no-more-running-just-sushi-lovers club, the regular hosting place, the ten-days-left t-shirt and your friendship. To *Neto* for the complains, the nicknames, the grumpiness and the salad-time followed by the the pizza-time. To Vicky, for sharing the endless grumbles, the empathy and her vision. To Andreea, for the great time, the cooking and the music. To Sander Wildeman, for the friday afternoon experiments. To Esli, for surprising me with the visit. To Michelle, for the cards against humanity and the Charles Dickens festival.

To the great community I found in Enschede: Nayeli, Lalo, Lorenzo, Oscar, Daniela, Jorge, Maite, Kasia, Altaf, Patti, Armin, Vivek, David, Lea, Roland, Loreto,

Leo, Kaisa, Lissy, Nekane, Minori, Ayaka, Vania, Isra, Nico, Álvaro, Lila, Tom, Fenna, Carolin, Lionel, Andrea, Elia, Elodie, Daniela Narezo and TJ. Thanks for glimming a light from home with you at all times.

To Lidia, for her joy, comfort and patience, but above all for joining the adventure of “There and back again”.

To my parents, for their support and their infinite courage.

To all the committee members that took the time to revise this manuscript and comment it.

To the sponsors of Lam Research Corporation, for an interesting topic, the challenge and the fruitful scientific discussions.

To all the missing people that my decaying memory forgets at this time of the night. Thank you all.

About the author

José Federico Hernández Sánchez was born in Mexico City in April the 27th of 1982. In 2001 he started a bachelor in Mechanical engineering at the *Universidad Nacional Autónoma de México* (UNAM). He defended the bachelor thesis titled *Emulsificación de residuos pesados de petróleo* (Emulsification of heavy oil residues), a project from the program UC-MEXUS in collaboration with the University of California in Santa Barbara. In 2008 he was admitted to the Masters in Materials Science at The *Instituto de Investigaciones en Materiales* of UNAM. As part of this program he did a three month internship in the Physics of Fluids group in the *Universiteit Twente* under the supervision of Devaraj van der Meer in 2010. In this internship he performed numerical simulations on the subcritical fluctuations before the onset of convection in granular materials. In 2011 he began his PhD studies under the supervision of Jacco Snoeijer in the physics of fluids group at the *Universiteit Twente*. During his PhD he was invited to talk about his research in the Dynamics at Interfaces Workshop that took place at the Okinawa Institute of Technology (OIST) in Japan. In 2014 Federico was also an invited speaker at the *Centro de Ciencias Aplicadas y Desarrollo Tecnológico* (CCADET) in Mexico and at The King Abdullah University of Science and Technology (KAUST) in the Kingdom of Saudi Arabia.